Ph. D. DISSERTATION

EFFECT OF SURFACE PASSIVATION OF NANOCRYSTALS ON ELECTRICAL PROPERTIES OF POLYMER-NANOCRSYTAL SOLAR CELL

나노결정 표면 패시베이션의 고분자−나노결정 태양전지의 전기적 특성에 미치는 영향 연구

BY

DONGGU LEE

FEBRUARY 2014

DEPARTMENT OF ELECTRICAL ENGINEERING AND COMPUTUER SCIENCE
COLLEGE OF ENGINEERING
SEOUL NATIONAL UNIVERSITY

EFFECT OF SURFACE PASSIVATION OF NANOCRYSTALS ON ELECTRICAL PROPERTIES OF POLYMER-NANOCRSYTAL SOLAR CELL

나노결정 표면 패시베이션의 고분자−나노결정
태양전지의 전기적 특성에 미치는 영향 연구

지도교수 이 창 희

이 논문을 공학박사 학위논문으로 제출함

2014 년 2 월

서울대학교 대학원

전기컴퓨터 공학부

이 동 구

이동구의 공학박사 학위논문을 인준함

2014 년 2 월

위 원 장 : _____ (인)
부위원장 : _____ (인)
위   원 : _____ (인)
위   원 : _____ (인)
위   원 : _____ (인)

Abstract

EFFECT OF SURFACE
PASSIVATION OF NANOCRYSTALS
ON ELECTRICAL PROPERTIES OF
POLYMER-NANOCRSYTAL
SOLAR CELL

DONGGU LEE

DEPARTMENT OF ELECTRICAL ENGINEERING
AND COMPUTER SCIENCE

COLLEGE OF ENGINEERING

SEOUL NATIONAL UNIVERSITY

Colloidal semiconductor nanocrystals (NCs) have been widely investigated due to their tunable optical and electrical properties through shape- and size control. Moreover, low cost solution based device fabrication processes such as inkjet printing or spin-casting are applicable to build NCs based optoelectronic devices. Tunable band gap and possibility to harvest excess energy as additional charge

carriers via multiple exciton generation attracted much attention toward colloidal NCs based solar cells.

The surface states originating from the non-bonding orbital of surface atoms has been regarded as the critical issues to deteriorate electrical and optical properties of NCs. several modification methods have been suggested to passivate surface traps and to reduce an insulating organic shell thickness.

However, in spite of the improvement in device performance, the chemical status of surface modified NCs still has not been clear; remnant or exchanged surface ligands and thickness of surface ligand shell are sensitively altered by temperature, concentration of additional ligands, and reaction time. Because of this complexity most reports have only described about the device performance before and after surface modification of NCs.

In this thesis, we investigated the relationships between surface chemistry changed by surface treatment (i.e., amount of surface ligands exchanged and average ligand chain length) and correlated device physics (i.e., charge separation, extraction, and recombination) in polymer-nanocyrstal hybrid solar cells.

Through the ^{1}H-NMR analysis, we observed different nature of ligands exchange according to functional group (carboxylic acid and amine group) and process sequence, and correlated their effect on Poly(3-hexylthiophene) (P3HT):CdSe quantum dot (QD) BHJ solar cell performances (current density-voltage (J-V) characteristics, incident photon-to-current conversion efficiency (IPCE)). Photogenerated charge carrier collection properties in active layers were studied using incident light intensity dependent J-V characteristics. Device performances depending on the thickness of active layer and donor: accepter blend ratio and the effect of thermal annealing were also investigated. By reducing insulating ligand shell thickness with sequential ligand exchange and passivating

surface trap states with 1-hexylamine ligand, carrier transport and collection property, and solar cell performance were significantly enhanced with 2% of power conversion efficiency (*PCE*) and 72% of carrier collection efficiency (η_{C0}).

However surface ligand modification in solution phase could alter the colloidal stability of NCs, and therefore, inevitable change of P3HT:NCs BHJ morphology is arisen. Since surface chemistry of NCs as well as nanoscopic morphology of the active layer are correlated with device performances, systematical study needs to clarify the effect of surface ligand on the device performances with fixed nanoscopic morphology. To prevent morphology change followed by surface ligand modification and resolve reliability problem, we propose a modular fabrication procedure to assemble CdSe TP nanocrystal/P3HT hybrid heterojunction. Such a modular approach enables the independent control of nanoscopic morphology and surface chemistry of the nanocrystals in reproducible manner, which are generally known to exhibit complex correlations. This modular fabrication separates the breakwaters-like nanocrystal network formation (step 1), the nanocrystal surface modification via chemical treatments (step 2), and the intrusion of polymers into the nanocrystal network (step 3). Accordingly, CdSe TP/P3HT hybrid heterojuctions could be assembled with their nanoscopic morphology and surface chemistry is simply under control without any morphology change. Thanks to the modular fabrication, nanocrystal could be surface modified simply with pyridine and 1-hexylamine and solar cell performance could be systematically examined through temperature-dependent *J-V*) measurements at varying illumination light intensities.

We found that a 2-fold increase in short circuit current with 1-hexylamine ligands, compared with the value based on pyridine ligands, originates from the

reduced depth of trap states, minimizing the trap-assisted bimolecular recombination process.

This thesis demonstrates the practical approaches to enhance efficiency of polymer-NC hybrid solar cells, covering the tailored surface modification of NCs, suitable device structure, and novel processing method. This approach is believed that could be applied not only polymer-NC hybrid solar cells but also other kinds of optoelectronic devices.

Keywords: Polymer-Nanocrystal Hybrid Solar Cells, Surface Modification, Quantum Dot, Tetrapod, Poly-3-hexylthiophene (P3HT)
Student Number: 2010-30224

Contents

List of Figures

List of Tables

Chapter 1

Introduction

There has been an enormous increase in the global demand for energy in recent years as a result of industrial development and population growth. However, fossil fuels generate greenhouse gas such as carbon dioxide (CO_2) that cause serious air pollution and climate change. The risks associated with CO_2 emissions and global warming have spurred interest in renewable energy, for instance, hydropower, geothermal, municipal waste, wood, biomass, solar, wind, and so on.

Among the renewable energy resources, clean and infinite solar energy is considered important future energy source. The U.S. Energy Information Administration forecasted that solar energy remains the forth important renewable energy source, after hydro, biomass, and wind power, having highest growth rate of 9.8% in terms of global energy generation through 2040 (See, **Figure 1.1**). The common solar cell that many of us have seen is called a photovoltaic (PV) cell, which converts light energy directly into electrical energy. Since 2012, the world's

cumulative PV solar cell capacity surpassed the 100-gigawatt (GW) installed electrical power mark, achieving just over 102 GW. This capacity is capable saving more than 53 million tons of CO_2 every year.
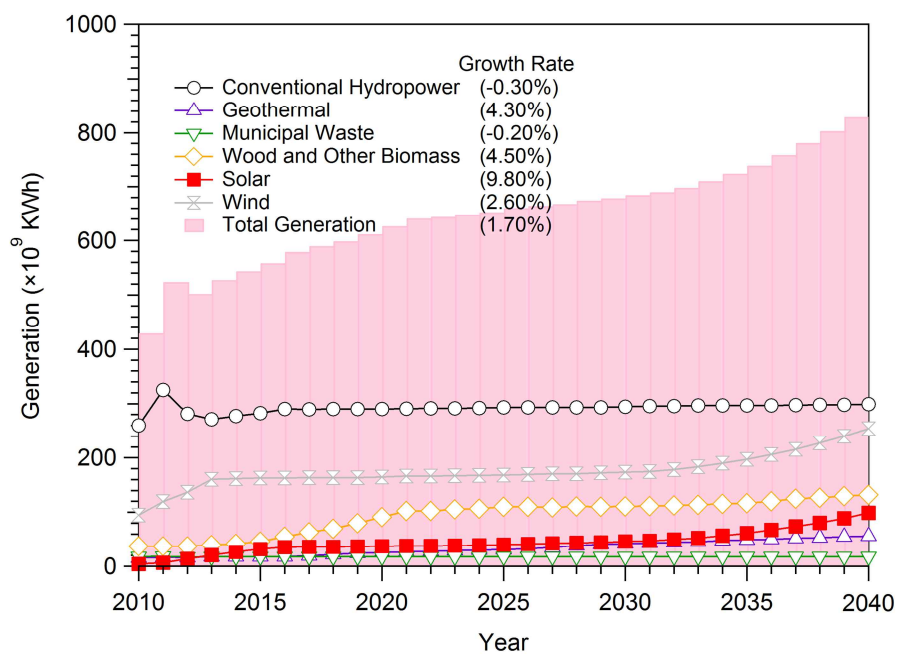
Figure 1.1 Projection for renewable energy generation in U.S. (Source: U.S. Energy Information Administration (Oct 2013)).

1.1   Colloidal Nanocrystal Based Solar Cells

The PV solar cells can be classified into so-called 1st, 2nd and 3rd generation. 1st generation solar cell is consist of pn-junction based on silicon wafers and dominate the commercial market (**Figure 1.2**). Si solar cells have a quite high efficiency, but very pure Si is needed, and the price is high compared to the power output. To provide a truly widespread primary energy source, solar cells must be be cost-competitive with fossil based electricity at utility scale.

Hence, improvements in efficiency as well as reducing manufacturing costs must be substantially required for cost-competitive solar cells. Concepts consuming less material based on thin film technology are considered as 2nd generation solar cells (for instance, amorphous Si cells, polycrystalline silicon on low cost substrate, Copper Indium Gallium Selenide (CIGS) cells, Cadmium Telluride (CdTe) cells).

To achieve high cost-effective and efficient solar cells, not only cost reduction in existing manufacturing process, but also science and technology breakthroughs requires. 3rd generation solar cells aims to overcome the so-called Shockley Queisser (SQ) limit. The third generation is somewhat ambiguous in the technologies that it encompasses, though generally it tends to include, among others, non-semiconductor technologies (including polymer cells and biomimetics), quantum dot (QD), tandem/multi-junction cells, intermediate band solar cell, hot-carrier cells, photon up-conversion and down-conversion technologies.
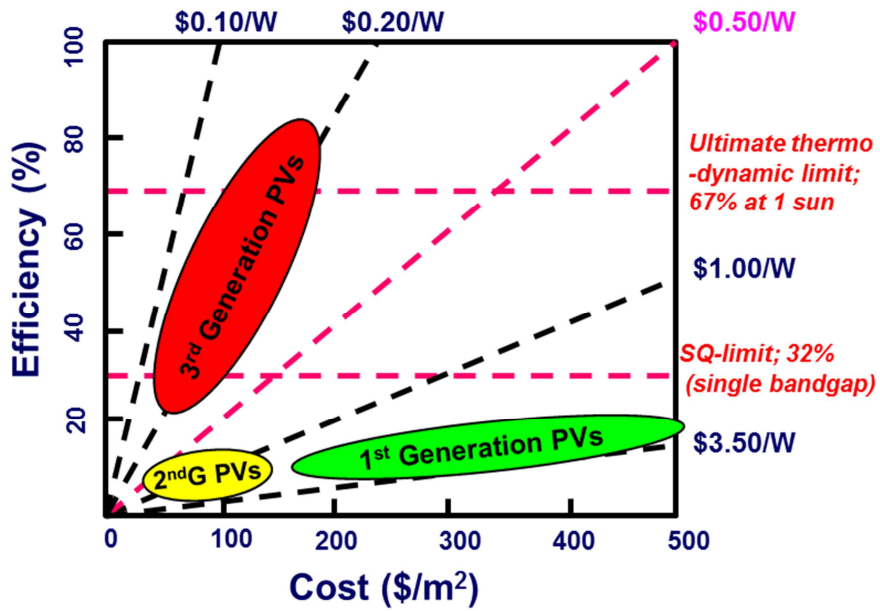
Figure 1.2 Solar electricity cost as function of module efficiency. the Shockley-Queisser limit for a quantum conversion device with a single band gap, in which carriers of lower energy are not absorbed and carriers of energy higher than the band gap thermalize to the band gap; the second-law thermodynamic limit on Earth for 1 Sun of concentration. (figure was redrawn from [1]).

Colloidal QDs based solar cells have been attracted great attention due to their superior optical and electrical properties, and possibility to harvest that excess energy as additional charge carriers via multiple exciton generation (MEG). MEG is a process that absorption of a high energy photon bearing at least twice the bandgap energy produces two or more electron-hole pairs. This phenomenon can occur in semiconductor nanocrystals (NCs), or QDs.

State-of-the-art research NC solar cell efficiency is very low compare to conventional Si solar cells but NC solar cells could be achieved theoretically higher than SQ limit of 32% [2-4]. In addition, incorporating NC solar cells into a solution process and flexible substrate is important issues that make it possible to fabricate solar cells with low cost mass product manufacturing such as roll-to-roll processing. Flexible and lightweight NC solar cells make many new applications possible. For instance, solar cells could be integrated into clothing which operates as wireless power without batteries.

Primarily, three kinds of solar cells based on colloidal NCs have been developed: (i) polymer-NC hybrid solar cell, (ii) NC-sensitized solar cell (NC-SSC), and (iii) all inorganic NC junction solar cell. **Table 1.1** shows best power conversion efficiency (PCE) achieved by each type of NC solar cells.

Since Greenham, Peng, and Alivisatos reported photoconductivity between polymer and NC composite film [3], polymer-NC hybrid type solar cells have been developed. The polymer-NC hybrid system could have both advantages of polymer (solution processable, flexible, light, and transparent) and NCs (tunable bandgap, wide absorption range, and MEG). The polymer-NC solar cells were construsted with nanostructured BHJ of polymer and NCs processed from solution [5]. Therefore device morphology cannot be precisely controlled on such a small scale. In addition, efficient transport of charge carriers to their respective electrodes before recombination is important to achieve high efficiency. High electron and hole

mobilities, controllable nanomorphology, and a well-structured interface are critical performance factors for developing efficient hybrid solar cells.

Second kind of NC solar cell is originated from dye-sensitized solar cell (DSSC) structure which is mainly composed of a sensitizer for light absorption, a nanoscale semiconductor porous photoanode (widely used TiO_2) for photogenerated electrons transfer from the sensitizer, an electrolyte to shuttle between the photoanode, and the counter electrode for the sensitizer regeneration. Elementary works to apply NCs as the sensitizer in DSSC configuration were first demonstrated by Vogel, Pohl, and Weller [6]. Two general approaches have been developed for depositing QDs onto TiO_2 electrodes: (i) direct growth of QDs on TiO_2 films using successive ionic layer adsorption and reaction (SILAR) [7, 8] or chemical bath deposition (CBD) [9] and (ii) postsynthesis assembly using presynthesized QDs [10].

All inorganic NC junction solar cells using thin film assembly of colloidal NCs, was first developed by Sargent et al. in 2007 [11]. In the first stage of the NC junction solar cells employed Schottky junction to separate charge. Typical Schottky junction NC solar cells were constructed with low bandgap p-type NCs such as PbS or PbSe, and shallow work function metals such as Mg or Al [12]. Due to the low upper bound on the built-in potential of Schottky barriers, Schottky junction NC solar cells have low open circuit voltage (V_{OC}). Moreover, Schottky junction NC solar cells have a limitation that incident light enters through nonrectifying side (ITO side) of the solar cells, since built-in potential formed at the back electrode side. To resolve these problems, depleted heterojunction NC solar cell in which an n-type transparent metal oxide such as TiO_2 induces a depletion region in the p-type NC solid, was developed. The depleted heterojunction solar cells have rapidly attracted attention as an effective architecture for extracting photogenerated current from NCs, and exhibited the highest power conversion efficiency (*PCE*) of 8.5%,

short circuit current (J_{SC}) of 22.7 mA/cm^2, V_{OC} of 0.62 V and fill factor (FF) of 61% [13]. In addition, Semonin, Luther, Joseph *et al.*, demonstrated *EQE* of over 100%, which denote MEG in depleted heterojunction solar cell structure [14].

Table 1.1 Best power conversion efficiency (*PCE*) achieved by each types of NC solar cell.

Type	Structure	Materials	*PCE* (%)	Ref.
Polymer-NC Hybrid	bulk heterojunction	PDTPBT:PbS$_x$Se$_{1-x}$	5.5	[5]
NC-SSC	SILAR or CBD	PbS:Hg	5.6	[7]
	Colloidal NCs	CdSe	5.4	[10]
NC junction	Schottky	PbSe	4.6	[12]
	Depleted heterojunction	TiO$_2$/PbS	8.5	[13]

1.2   Polymer-Nanocrystal Hybrid Solar Cells

Since Huynh, Dittmer, and Alivisatos demonstrated the frist hybrid solar cells with BHJ structure of P3HT and CdSe QDs in 2002 [15], various combinations of electron donor polymers and electron acceptor NCs, for example, CdSe [16-26], CdS [27, 28], PbS_xSe_{1-x} [5], ZnO [29] and TiO_2 [30] have been investigated to improve efficiency. In addition, the anisotropic structure of NCs such as nanodot (ND) [5, 17, 20-22, 24, 26, 28, 29], nanorod (NR) [16, 19, 23, 27, 30], tetrapod (TP) [18, 31], and hyperbranched structures [32], have been employed to facilitates electron transport.

The surface ligands surrounding NCs are also recognized as important factor to determine their colloidal stability as well as electrical characteristics. Greenham *et al*. reported that long ligands used in the NC synthesis were harmful to the charge transfer process between polymers and NCs [33]. They investigated the PL quenching of MEH-PPV:CdS NC blends, where either trioctylphosphine oxide (TOPO)-coated or pyridine-treated NCs were used. For the blends with pyridine treated NCs exhibited signficant quenching of PL, implying efficient electron transfer from the polymer to NCs. However, no PL quenching was observed with TOPO covered on the NC surface, indicating no electron transfer from MEH-PPV to CdS NCs. Therefore ligand exchange processes for exchanging a long synthesis ligands to short ones, are needed to obtain good device performance.

In 2003, the Alivisatos group investigated the issue of ligands and PL in more detail using P3HT:CdSe blends. They found that excess pyridine could be removed by pumping the device under low pressure ($<10^{-6}$ mbar) and/or thermal annealing, due to the low boiling point of pyridine. The device performance could be significantly improved with the thermal annealing process.

The pyridine treatment of NCs [16-18, 23, 25, 26, 30-32] has been challenged recently, since devices based on NCs treated with other short ligands (like amines [21], thiols [5, 19, 24, 28], or acids [20, 22] based ligand) have been reported to outperform those based on pyridine-treated NCs. (See **Table 1.2** for performance of various polymer:NC hybrid solar cells.).

In 2005, Sargent and coworkers treated PbS NCs with octylamine, and blended NCs with MEH-PPV. Although the device efficiency was low, significant improvement compared with devices fabricated from oleic acid (OA)-coated NCs were achieved, proving the effectiveness of amine treatment [34]. Carter and co-workers also investigated P3HT:CdSe blends with different short ligands on the NC surface, including tributylamine, butylamine, and pyridine, and as a result, devices based on butylamine-treated CdSe NCs gave the highest efficiency [35].

In 2010, Wu and Zhang managed to perform thiol treatment using a vapor annealing method. They spin-coated blends of P3HT and pyridine-treated CdSe NCs, and then, the substrate was left for vapor annealing using benzene-1,3-dithiol at 120ºC. As a result, they observed replacement of original ligand to the benzene-1,3-ditiol, and significant enhancement of short-circuit current and power conversion efficiency were achieved compared with the control device which was not vapor-annealed [19].

Chou and co-workers achieved a power conversion efficiency of 3.2% combining with polymer and device structure engineering. They employed a functional conjugated polymer of mono-aniline-capped poly[(4,4′-bis(2-ethylhexyl)-dithieno[3,2-b:2′,3′-d]silole)-2,6-diyl-alt-(2,1,3-benzothiadiazole)-4,7-diyl] (PSBTBT-NH$_2$) as a donor (D) and cadmium telluride (CdTe) NCs comprising a tetrapod or nanorod-shape as an acceptor (A) and solvent–vapor annealed with

9

benzene-1,3-dithiol (BDT) to improve the charge separation at the D/A interface and efficient charge transportation. [36].

Alternatively, Prasad and coworkers employed a post-ligand exchange method to replace OA ligands with 1,2-ethanedithiol (EDT) based on bulk hetrojunction solar cells with poly(2,6-(N-(1-octylnonyl)dithieno[3,2-b:20,30-d]pyrrole)-alt-4,7-(2,1,3-benzothiadiazole)) (PDTPBT) and OA-capped PbS NCs. They spin-coated blends of PDTPBT and PbS NCs, and then, EDT solution in acetonitrile was spin-coated on the blend film to exchange OA. They introduced a layer of TiO$_2$ NCs as the hole-blocking layer beneath the cathode. The device exhibited a high power conversion efficiency of 3.78% [37]. In the meantime, Ren *et al.* reported a high efficiency of 4.1% for hybrid PVs based on P3HT and CdS NCs, which were also treated with EDT. The EDT-treated device showed 70% improvement in device efficiency compared with the non-treated one [28].

More recently, Brutchey and co-workers demonstrated polymer/NC solar cells fabricated from blends of tert-butylthiol-treated CdSe nanocrystals and P3HT and obtained an efficiency of 1.9%.1The thiol-treated CdSe nanocrystals are found to consistently exhibit high open circuit voltage of 0.80 V, implying that the LUMO and HOMO levels of NCs changed to a favorable band alignment between the P3HT HOMO and the CdSe LUMO with tert-butylthiol treatment [24].

In 2010, Krüger and co-workers proposed the acid treatment using hexanoic acid (HA). The CdSe NCs covered with a long synthesis ligand, hexadecylamine (HDA), were washed using HA. this acid treatment form an organic salt which effectively remove the HDA, and obtained a power conversion efficiency of 2% with bulk hetrojunction solar cells consisting of P3HT and the acid-treated CdSe QDs [38]. Later on, they found that this acid treatment method could also be applied to CdSe NCs covered with trioctylphosphine (TOP)/OA ligands [39].

Thanks to the efforts of many researchers (introduction of low bandgap donor polymer and NCs, and novel surface treatment), the best power conversion efficiency of polymer:NC hybrid solar cell has so far been known as 5.5% with a structure of PDTPBT/PbS$_x$Se$_{1-x}$ QDs [5].

However, in spite of the improvement in device performance, the chemical status of surface modified QDs still has not been clear; remnant or exchanged surface ligands and thickness of surface ligand shell are sensitively altered by temperature, concentration of additional ligands, and reaction time. In addition, device structure of hybrid solar cells still unchanged since 2002. Therefore, the relationships between surface chemistry changed by ligand manipulation and correlated device physics in polymer:NC solar cell systems should be investigated and novel device structure have to be developed to make full use of the NCs.

Table 1.2 Selected performance parameters of polymer:NC hybrid solar cells.

Donor	Acceptor	Surface treatment	J_{SC} (mA/cm²)	V_{OC} (V)	FF (%)	PCE (%)	Ref.
P3HT	CdSe QDs	pyridine	2.6	0.67	36	0.65	[17]
		butylamine	5.5	0.78	47	2.0	[21]
		tert-butylthiol	5.6	0.80	43	1.9	[24]
		hexanoic acid	5.8	0.62	56	2.0	[20]
	CdSe NRs	pyridine	8.79	0.62	50	2.9[*]	[16]
		pyridine/dithiol	9.7	0.55	49	2.65	[19]
	CdSe TPs	pyridine	4.83	6.33	52	1.49	[31]
	Hyperbranched CdSe NCs	pyridine	7.1	0.60	51	2.18	[32]
	CdS QDs	butylamine/1,2-ethanedithiol	10.9	1.1	35	4.1	[28]
	CdS NRs	N/A[†]	9	0.65	48	2.9	[27]
	ZnO QDs	N/A[†]	5.2	0.75	52	2.0	[29]
	TiO₂ NRs	pyridine	2.73	0.63	56	0.98	[30]
PCPDTBT	CdSe QDs	pyridine	9.2[‡]	0.78[‡]	49[‡]	3.5[‡]	[26]
	CdSe QDs	hexanoic acid	8.7	0.63	56	3.1	[22]
	CdSe NRs	pyridine	12.1	0.63	45	3.42	[23]
	CdSe QDs+NRs[**]	pyridine	13.9	0.48	51	3.5	[25]
	CdSe TPs	pyridine	10.1	0.68	51	3.19	[18]
PDTPBT	PbSₓSe₁₋ₓ QDs	1,3-benzenedithiol	14.66	0.57	66	5.5	[5]

[*]Correcting for spectral mismatch between solar simulator and the true AM1.5G spectrum gives an AM1.5G *PCE* of 2.6%. [†]in-situ growth of NCs in polymer matrix. [‡]Device applied ZnO NDs for optical spacer. For the device without a ZnO NDs layer, J_{SC} = 7.2 mA/cm₂, V_{OC} = 0.78 V, *FF* = 48%, and *PCE* = 2.7%, [**]NDs:NRs = 27:63 wt. ratio.

1.3　Outline of Thesis

This thesis consists of five chapters including **Introduction** and **Conclusion**. In **Chapter 1**, brief history of solar cells based on colloidal nanocrystals and research issues of surface modification and shape control of nanocyrstals are introduced. In **Chapter 2**, basic solar cell theories including equivalent circuit models and light intensity dependent characteristics are described. In addition preparation of nanocrystals and solar cell fabrication and characterization methods are described. The chemical structures of organic materials which used in this thesis are depicted. In **Chapter 3**, the relationships between surface chemistry changed by surface treatment and correlated device physics are investigated based on P3HT:CdSe QD BHJ solar cells. Through the ^{1}H-NMR analysis, we observed different nature of ligands exchange according to functional group and process sequence, and correlated their effect on P3HT:CdSe QD BHJ solar cell performances (current density-voltage (J-V) characteristics, incident photon-to-current conversion efficiency (IPCE)). Photogenerated charge carrier collection properties in active layers were studied using incident light intensity dependent J-V characteristics. Device performances depending on the thickness of active layer and donor: accepter blend ratio and the effect of thermal annealing were also investigated. However surface ligand modification in solution phase could alter the colloidal stability of NCs, and therefore, inevitable BHJ morphology change is arisen. In **Chapter 4**, to identify the effect of surface ligand on device performance without morphology change, we propose a modular fabrication method to assemble CdSe TP nanocrystal/polymer hybrid heterojunction solar cells, which provides uniform and reliable TP film morphology and simple chemical modification of CdSe TP with fixed morphology. Consequently, the influence of nanocrystal surface modification

on the as-assembled solar cell performance could be systematically examined through temperature-dependent current density-voltage measurements at varying light intensities.

Chapter 2

Theory and Experimental Methods

2.1 Basic Solar Cell Characteristics

2.1.1 Solar Cell Performance Parameters

Performances of solar cells are characterized by current density-voltage (J-V) curve under illumination of a light source that resembles the solar spectrum. The main parameters that are used to characterize the performance of solar cells are maximum power point power (P_{max}), short-circuit current density (J_{SC}), open-circuit voltage (V_{OC}), and fill factor (FF). Power conversion efficiency (PCE) of a solar cell is determined from these parameters. A typical J-V curve of a solar cell is shown in Figure 2.1.
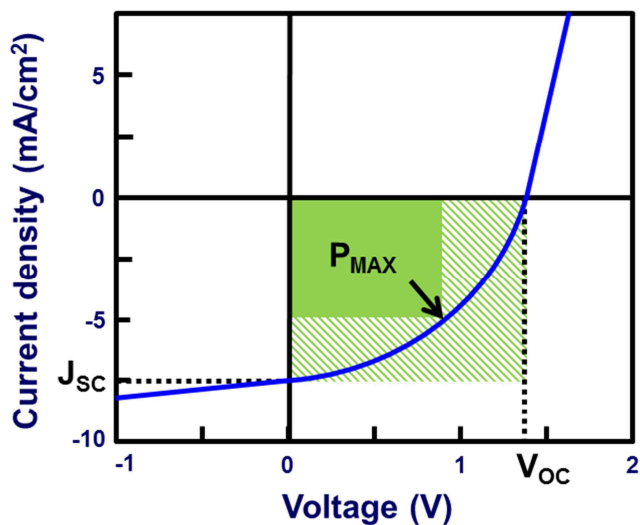
Figure 2.1 Typical current density-voltage (*J-V*) curve of solar cell.

The J_{SC} is the current density that flows through the external circuit when the electrodes of the solar cell are at short condition (zero bias). In terms of J_{SC}, optical properties (band gap and extinction coefficient) as well as electrical properties (efficient exciton dissociation, charge carrier transport, recombination and collection) of active layer are critical factor to determine J_{SC}.

The V_{OC} is the voltage at which no current flows through the external circuit. It is the maximum voltage that a solar cell can deliver. In the MIM picture, the V_{OC} originated by the built-in potential generated by difference in work function of the cathode and anode. But in the case of polymer:fullerene solar cells, V_{OC} is empirically proportional to the difference between the highest occupied molecular orbital energy of donor and the lowest unoccupied molecular orbital energy of acceptor [40, 41]. The built-in potential of polymer:NC hybrid solar cells, in common with polymer solar cells, should be originated from energy level difference

16

of polymer and NC. Therefore to achieve high V_{OC}, size, composition, and materials of NC should be designed and tailored to match with energy level of polymer.

The point where the electrical power ($P = I \times V$) reaches the maximum value called the maximum power point (P_{max}) which represents the condition where the solar cell can deliver its maximum power to an external load. The *FF* is the ratio between the maximum power generated by a solar cell and the product of V_{OC} and J_{SC}. Typical polymer:NC hybrid solar cells exhibit 20–70% of *FF* due to transport and recombination losses.

$$FF = \frac{P_{\max}}{J_{SC} \times V_{OC}}$$ (2.1)

The *PCE* is the most commonly used parameter to compare the performance of one solar cell to another. The *PCE* is the percentage of the solar energy to converted electrical power by solar cell. The *PCE* is calculated by dividing P_{max} by the input energy (P_{light}). By convention, *PCE* are measured under standard test conditions, which are a temperature of 25 °C and an irradiance of 1 sun (100 mW/cm^2) with an air mass 1.5 global (AM1.5G) spectrum. These conditions correspond to a clear day with sunlight incident upon a sun-facing 37°-tilted surface with the sun at an angle of 41.81° above the horizon

$$PCE\ (\%) = \frac{Electric\ Power}{Light\ Power} = \frac{J_{sc} \times V_{oc} \times FF}{P_{light}} \times 100\ (\%)$$ (2.2)

The quantum efficiency (*QE*) is the ratio of the number of carriers collected by the solar cell to the number of photons of a given energy incident on the solar cell. There are two types of *QE* of a solar cell which are often considered: external quantum efficiency (*EQE*) and internal quantum efficiency (*IQE*). *EQE* is the ratio

17

of the number of charge carriers collected by the solar cell to the number of photons of a given energy shining on the solar cell from outside (incident photons) and IQE is the ratio of the number of charge carriers collected by the solar cell to the number of photons of a given energy which are absorbed by the cell. *EQE* and *IQE* are functions of the photons' wavelength (λ).

$$EQE\,(\%) = \frac{number\ of\ electrons\ in\ external\ circuit}{number\ of\ incident\ photons} \qquad (2.3)$$

$$IQE\,(\%) = \frac{number\ of\ electrons\ in\ external\ circuit}{number\ of\ absorbed\ photons} \qquad (2.4)$$

$$IQE\,(\%) = \frac{EQE}{Total\ Absorption} = \frac{EQE}{1 - Reflection - Transmission} \qquad (2.5)$$

Spectral responsivity (*SR*) is a similar with *QE*, but it has different unit (A/W). SR is defined as current comes out of the solar cell per incoming photon of a given energy and wavelength:

$$SR(\lambda) = \frac{J_{SC}(\lambda)}{\Phi(\lambda)} \qquad (2.6)$$

where Φ is incident optical power per unit area in W/m^2 and J_{SC} is short circuit current density in A/m^2.

QE can be converted from *SR* as follows:

$$QE\,(\%) = SR(\lambda) \times \frac{h\,c}{q\lambda} \times 100\ (\%) \qquad (2.7)$$

Where λ is wavelength of photon, h is the Planck constant, c is the speed of light in a vacuum, and q is the elementary charge.

Incident photon-to-current conversion efficiency (*IPCE*) is typically considered as *EQE*. Ideally, if we know standard solar spectrum or solar simulator spectrum, J_{SC} can be calculated by integrating *IPCE* spectra.

$$J_{SC} = \int \frac{P_{light}(\lambda) \times \lambda}{h\,c} \times \frac{IPCE(\lambda)}{100} \times q \; d\lambda \qquad (2.8)$$

2.1.2   Equivalent Circuit Model

J-V curves of solar cell can be described with equivalent circuit models which consist of diode, series and shunt resistance (Figure 2.2). From the equivalent circuit, current density flowed by the solar under illumination is a summation of the dark diode current density (J_{diode}), leakage current density (J_{leak}), and the photo-generated current density (J_{ph}), given as

$$J = J_{diode} + J_{leak} - J_{ph} \qquad (2.9)$$

Voltage drop across the R_S and then, considering Kirchhoff's law, V can be expressed as

$$V = J_{leak} R_{Sh} + J R_S \qquad (2.10)$$

Equation (2.9) and (2.10) lead to

$$J = J_{diode} + \frac{V - J R_S}{R_{Sh}} - J_{ph} \qquad (2.11)$$

The current density flows through the diode is expressed by the Shockley diode equation:

$$J_{diode} = J_0 \left[e^{\frac{q}{nk_BT} V_{diode}} - 1 \right] \qquad (2.12)$$

where J_0: reverse saturation current density, n: diode ideality factor, k_B: Boltzmann's constant and V_{diode}: voltage across the diode. Therefore, J can be derived as following equation:

$$J = J_0 \left[e^{\frac{q}{nk_BT}(V - JR_S)} - 1 \right] + \frac{V - JR_S}{R_{Sh}} - J_{ph} \qquad (2.13)$$

In the case of short circuit condition (V=0) and open circuit condition (J=0), J_{SC} and V_{OC} are given by

$$J_{SC} = J_0 \left[e^{\frac{q}{nk_BT}(-J_{SC}R_S)} - 1 \right] - \frac{J_{SC}R_S}{R_{Sh}} - J_{ph} \qquad \text{(V=0)} \qquad (2.14)$$

$$0 = J_0 \left[e^{\frac{q}{nk_BT}V_{OC}} - 1 \right] + \frac{V_{OC}}{R_{Sh}} - J_{ph} \qquad \text{(J=0)} \qquad (2.15)$$

Considering high-quality solar cell, which have low R_S and J_0, and high R_{Sh}, the J_{SC} and V_{OC} can be expressed :

$$J_{SC} \approx -J_{ph} \qquad \text{(V=0)} \qquad (2.16)$$

$$V_{OC} \approx \frac{nk_BT}{q} \ln \left(\frac{J_{ph}}{J_0} + 1 \right) \qquad \text{(J=0)} \qquad (2.17)$$

20
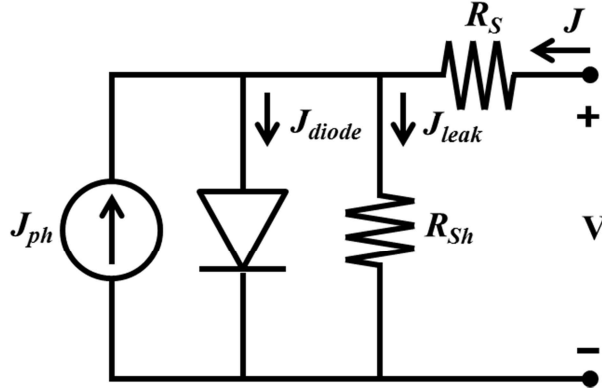
Figure 2.2 Equivalent circuit diagram of solar cell. J_{ph}: photogenerated current density, J_{diode}: diode current density, J_{leak}: leakage current density, R_S: series resistance, and R_{Sh}: shunt resistance.

2.1.3 Light Intensity Dependence of Solar Cells

Incident light intensity dependent J-V measurement provide carrier collection [42-44] and recombination characteristics [45, 46] of solar cells. The incident light intensity dependence of J_{SC} follows a power law dependence upon the light intensity (I_{light}) with the incident light intensity scaling exponent (α), i.e. $J_{SC} \propto I_{light}^{\alpha}$. The α correlates with a carrier loss mechanism, which is if $\alpha = 1$, the carrier loss mechanism originates from the monomolecular recombination, whereas if the bimolecular recombination arises, α reduce to 0.5. This could be interpreted as a result of competition between recombination of charge carriers and extraction before recombination. If extraction of charge carriers is faster than recombination, recombination mechanism is dominated by monomolecular recombination, and therefore, α should be close to 1, whereas if the recombination of charge carries is

comparable with carrier extraction, the bimolecular recombination arises and then α will reduce.

In equivalent circuit model for solar cells, the J_{rec} has been introduced in the solar cells which consisted of disordered materials, such as, amorphous silicon solar cell or organic solar cell (Figure 2.4). The J_{rec} represents an additional loss term of J_{ph} in active layer, which increases significantly with the forward voltage. Equation (2.13) can be modified as following equation from the modified equivalent circuit model.

$$J = -J_{ph} + J_0\left\{\exp\left[\left(\frac{q}{nk_BT}(V - R_SJ)\right)\right] - 1\right\} + \frac{V - R_SJ}{R_{Sh}} + J_{rec} \qquad (2.18)$$

All linear fit of J-V curves of various incident light intensity at short circuit conditions (V=0), intersect the x-axis at a single point of voltage, which is called collection voltage (V_C) and short circuit resistance (R_{SC}) can be defined as a reciprocal slope of the J-V curve at V=0, i.e., $V_C = R_{SC}J_{SC}$. The V_C provides carrier collection properties in the solar cells.
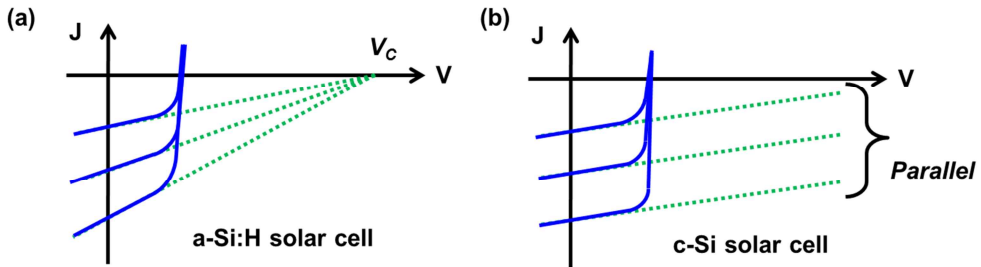
Figure 2.3 Schematic representation of the theoretical behavior of J-V curves of (a) a-Si:H solar cell and (b) c-Si solar cell (figure was redrawn from [47]).

Short circuit resistances (R_{SC}, reciprocal slopes of the *J-V* curve at V=0, i.e., $V_C = R_{SC} J_{SC}$) can be described based on the modified equivalent circuit model in Figure 2.4. From the equation (2.18), the $\partial J / \partial V$ can be expressed as following equation:

$$\frac{\partial J}{\partial V} = \frac{\dfrac{q}{nk_BT} J_0 \exp\left[\dfrac{q}{nk_BT}\left(V - R_S J\right)\right] + \dfrac{1}{R_{Sh}} + \dfrac{\partial J_{rec}}{\partial V}}{1 + R_S \dfrac{q}{nk_BT} J_0 \exp\left[\dfrac{q}{nk_BT}\left(V - R_S J\right)\right] + \dfrac{R_S}{R_{Sh}}} \tag{2.19}$$

Thus, if we take into account short circuit condition (V=0), we can derive the R_{SC}:

$$\frac{1}{R_{SC}} = \frac{\dfrac{q}{nk_BT} J_0 \exp\left[-\dfrac{q}{nk_BT} R_S J\right] + \dfrac{1}{R_{Sh}} + \dfrac{\partial J_{rec}}{\partial V}\Big|_{V=0}}{1 + R_S \dfrac{q}{nk_BT} J_0 \exp\left[-\dfrac{q}{nk_BT} R_S J\right] + \dfrac{R_S}{R_{Sh}}} \tag{2.20}$$

Since all parameters except J_{rec} are determined from dark *J-V* characteristics, the R_{SC} reflect the recombination term (J_{rec}) under various light intensity. If we consider $R_{Sh} \gg R_S$, and moderated applied voltage ($J_{ph} \gg J_{diode}$), R_{SC} and *J* can be expressed :

$$\frac{1}{R_{SC}} \approx \frac{\partial J_{rec}}{\partial V}\Big|_{V=0} \tag{2.21}$$

$$J \approx J_{ph} - J_{rec} \tag{2.22}$$

Recently, Voz *et al.* derived a compact expression for the current density near the short circuit condition under these assumptions (constant electric filed, drift-driven collection and monomolecular recombination [44]:

$$J \approx qGL\left(1 - \frac{L/2}{l_C}\right) \qquad (2.23)$$

where l_C is the collection length, which is defined as the sum of the drift lengths of electrons ($l_n = \mu_n \tau_n E$) and holes ($l_p = \mu_p \tau_p E$), G is the effective generation rate of charge carriers per unit volume, and L is thickness of active layer. The l_C implies conceptually the maximum travel distance of separated electron and hole driven by electric field (E) before recombination. Since we assume the constant electric filed, E within the active layer can be expressed:

$$E = \frac{V_{bi} - V}{L} \qquad (2.24)$$

If we introduce effective $\mu\tau$ product, $\mu\tau_{eff} = \mu_n \tau_n + \mu_p \tau_p$, l_C is derived as following:

$$l_C = \mu\tau_{eff}\frac{V_{bi} - V}{L} \qquad (2.25)$$

The built in potential (V_{bi}) of solar cells, which have sandwich structure of two different electrodes, is determined by work function difference of the electrodes. In most case of organic solar cells constructed with PEDOT:PSS and Al electrode, V_{bi} can be estimated around 0.7 eV [44].

In equation (2.23), photogenerated current density (J_{ph}) is can be identified as qGL, and then, J_{SC} can be described using short circuit collection length (l_{C0}):

$$J_{SC} = J_{ph}\left(1 - \frac{L/2}{l_{C0}}\right) \tag{2.26}$$

where $l_{C0} = \mu\tau_{eff}V_{bi}/L$, which means collection length evaluated at $V=0$. Finally, we can obtain the analytical expression of recombination term, J_{rec} at moderated applied voltage ($J_{ph} \gg J_{diode}$):

$$J_{rec} = J_{ph}\frac{L/2}{l_C} = J_{ph}\frac{L^2/2}{\mu\tau_{eff}(V_{bi} - V)} \tag{2.27}$$

According to equation (2.21), (2.26), and (2.27), the R_{SC} can be evaluated:

$$R_{SC} = \frac{l_{C0}}{L/2}\frac{V_{bi}}{J_{ph}} = \left(\frac{l_{C0}}{L/2} - 1\right)\frac{V_{bi}}{J_{SC}} \tag{2.28}$$

Therefore, V_C can be examined as following:

$$V_C = \left(\frac{l_{C0}}{L/2} - 1\right)V_{bi} \tag{2.29}$$

From the equation (2.23), collection efficiency (η_C) of photogenerated charge carriers can be defined:

$$\eta_C = 1 - \frac{L/2}{l_C} \tag{2.30}$$

Now, we can evaluate $\mu\tau_{eff}$ and collection efficiency at short circuit condition (η_{C0}) from the V_C.

$$\mu\tau_{eff} = l_{C0}\frac{L}{V_{bi}} = \frac{L^2}{2V_{bi}}\left(\frac{V_C}{V_{bi}}+1\right)$$ (2.31)

$$\eta_{C0} = 1 - \frac{L/2}{l_{C0}} = 1 - \frac{1}{V_C/V_{bi} + 1}$$ (2.32)
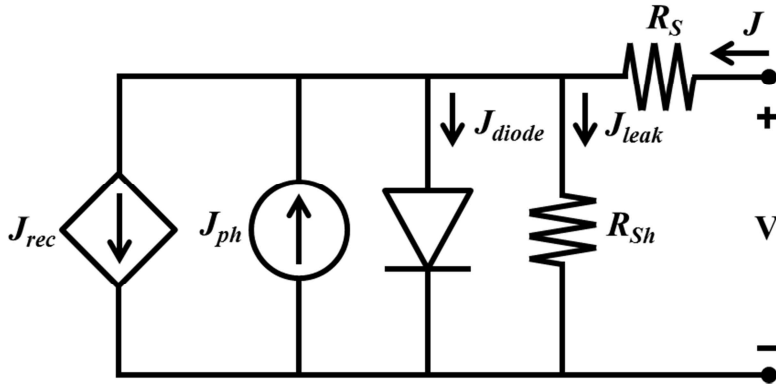
Figure 2.4 Modified equilvanet circuit diagrams for solar cells. J_{rec}: recombination current density, J_{ph}: photogenerated current density, J_{diode}: diode current density, J_{leak}: leakage current density, R_S: series resistance, and R_{Sh}: shunt resistance., J_{rec} represents an additional loss term of J_{ph} in active layer.

2.2　Materials

2.2.1　Synthesis and Surface Modification of CdSe Quantum Dots

In order to prepare CdSe QDs, synthetic procedure proposed by Zhong *et al.* was slightly modified [48]. Briefly, a Cd stock solution was obtained by reacting 10 mmol of CdO and 10 mL of oleic acid in 10 mL of ODE at 270 °C for 20 min under N_2 flow. Then, 6 mmol of Se powder and 3 mL of n-trioctylphosphine were loaded into 100 mL 3-neck round flask and heated up to 150 °C for 20 min under N_2 flow. After Se powder is fully dissolved, 50 mL of oleylamine was added and heated up to 300 °C. Next, 12 mL of Cd stock solution (6 mmol) was swiftly injected into the reaction flask within 1 sec and the temperature was set to 280 °C. After 10 min of reaction time, the product was cooled down to room temperature and purified three times through precipitation/redispersion procedure with acetone/methanol (v/v = 2 : 1) and toluene. At the end of purification process, the precipitate was dried under N_2 atmosphere for 10 min and dispersed in chloroform.

In a typical procedure for ligand exchange, 200 mg of QDs in 4 mL chloroform and 4 mL of ligands (1-hexylamine or hexanoic acid) were placed in an air-tightened vial, and sonicated for 15 min. And then the resulting QDs were purified for three times by precipitation with the excess of methanol and re-dispersion with chloroform. At the final step of purification, the precipitate was dried under N_2 atmosphere for 5 min, and dissolved in 3 mL of chloroform. For the sequential ligand exchange, the QDs were firstly modified with hexanoic acid, purified twice, and then modified with 1-hexylamine. The final product was purified one time to remove residual 1-hexylamine.

However, for the NMR measurement, we purified the final product three times in order to remove residual 1-hexylamine on QD surfaces. Surface coverage of ligands was characterized by using a 500 MHz ^{1}H-NMR, using $CdCl_3$ as a solvent and bromoform as internal concentration reference. In order to remove reaction byproducts in QD dispersion or weakly-bound ligands on QDs, every sample for ^{1}H-NMR were purified three times with methanol and chloroform, and dried under N_2 atmosphere for 10 min.

2.2.2   Synthesis and Surface Modification of CdSe Tetrapods

Modified synthetic procedure by Lim *et al.* was adopted for the synthesis of CdSe TPs [49]. Cd and Se precursor solutions for arm growth were prepared as follows. Cadmium oleate ($Cd(OA)_2$) solution was prepared by dissolving 10 mmol of CdO in 7.8 mL of OA, 6.2 mL of ODE, and 1 mL of TOP in a round bottom flask at 280 °C under N_2 flow. After the mixture became optically clear, the round bottom flask was cooled down to 50 °C and 0.14 mmol of CTAB was added. Separately, 12 mmol of Se and 6 mL of TOP were mixed in a 50 mL round bottom flask with a condenser and heated at 200 °C. Once the mixture became transparent, the TOPSe solution was cooled down to room temperature. 5 mL of TOPSe solution was then added to the $Cd(OA)_2$ solution and the resulting mixture was stirred for 5 minutes.

To prepare CdSe seeds with zincblende crystal structure, 0.5 mmol/mL of $Cd(OA)_2$ solution was prepared by reacting 5 mmol of CdO, 5 mL of OA, and 5 mL of ODE at 280 °C under N_2 flow for 15 min and then the reaction mixture was cooled down to room temperature. Following, 1 mmol of Se and 10 mL of ODE were loaded into a 100 mL 3-neck round flask and heated up to 300 °C under N_2 flow. When the Se/ODE solution became optically clear, 4 mL of $Cd(OA)_2$ solution

(2 mmol) was rapidly injected into the solution and reacted at 270 °C for 15 min. Finally, 6 mL of ODE was added into the seed solution and the reaction mixture was cooled down to room temperature.

Using the as-prepared injection solution and the CdSe seeds, CdSe TPs were synthesized by continuous precursor injection approach. For a typical synthesis to attain 76 nm-long CdSe TPs, 2.5 mL of seed solution, 2.25 mL of OA, 1.5 mL of TOP, 23.75 mL of 1-ODE, and 0.21 mmol of CTAB were placed in a 3-neck round bottom flask and then were heated up to 260 °C. At this elevated temperature, 30 mL of injection solution was injected into the reactor in a stepwise manner: 0.5 mL/min for 6 min, 0.6 mL/min for 6 min 40 sec, 0.7 mL/min for 8 min 35 sec, (the temperature was set to 280 °C at this step), and 0.8 mL/min for 8 min 45 sec. After finishing precursor injection, the reactor was quenched rapidly. To purify the product, 2 mL of chloroform and an excess amount of acetone were added into the cooled reactor until the solution became turbid. After the centrifugation at 3000 rpm, the supernatant was decanted and the precipitate was re-dispersed in organic solvents such as chloroform, toluene, or hexane. The precipitation and re-dispersion was repeated until the samples were sufficiently purified.

5 mL of oleate-capped CdSe TP solution (40 mg/mL) was collected through precipitation using excess ethanol and following centrifugation at 3000 rpm. After discarding transparent supernatant, the precipitate was dissolved with 5 mL of hexane. 5 mL of N,N-dimethylformamide (DMF)/0.5 mL of HBF_4 solution (48 wt% in H_2O) was then added to the CdSe TP solution dissolved in hexane. After short voltexing for less than a minute, CdSe TPs were collected in the polar DMF phase and oleic acid was remained in the non-polar hexane phase. After removing the upper phase containing oleic acid, 5 mL of hexane was added and the mixture was vortexed again to wash out oleate ligands in the DMF/H_2O phase. After repetitive

29

washing steps for three times, the mixture was precipitated with excess amount of acetone. To remove oleate ligands completely, HBF$_4$ treatment was conducted once again with same amount of DMF, HBF$_4$ solution, and hexane.

To modify bare CdSe TPs with oleylamine ligands, the bare CdSe TPs were precipitate with excess acetone and re-dispersed in chloroform/oleylamine mixture (chloroform : oleylamine = 8 : 2 (v/v)). After 10 minutes, the excess amount of acetone was added to the CdSe TP solution and then the solution was centrifuged at 3000 rpm to remove remnant HBF4 or water. Finally, the preciptates was re-dispersed in 3 mL of chloroform/oleylamine (chloroform: oleylamine = 30 : 1 (v/v)).

2.2.3   Synthesis of ZnO Nanoparticles

ZnO nanoparticles were synthesized modifying the method reported by Pacholski et al. 3 g of Zn(ac)$_2$·2H$_2$O and 120 mL of methanol were first placed in a 3-neck round bottom flask and heated to 60 °C. At 60 °C, a 60 mL KOH solution containing 1.51 g of KOH was added dropwise into the Zn(ac)$_2$·2H$_2$O solution under strong agitation. The reaction mixture was kept at 60 °C for 2 hr 15 min to yield a milky solution containing ZnO nanoparticles. The ZnO nanoparticles were then isolated by centrifugation at 4000 rpm followed by repetitive washing using methanol. Finally, the product was centrifuged again and re-dispersed in 5 mL of butanol.

2.2.4   Organic Materials

Poly(3-hexylthiophene) (P3HT, PHO148) for donor polymer and poly(3,4-ethylenedioxythiophene):poly(styrenesulfonate) (PEDOT:PSS) (Clevios P) as a hole buffer layer were purchased from 1-Material Inc. and Heraeus, respectively. All chemicals were used as purchased.
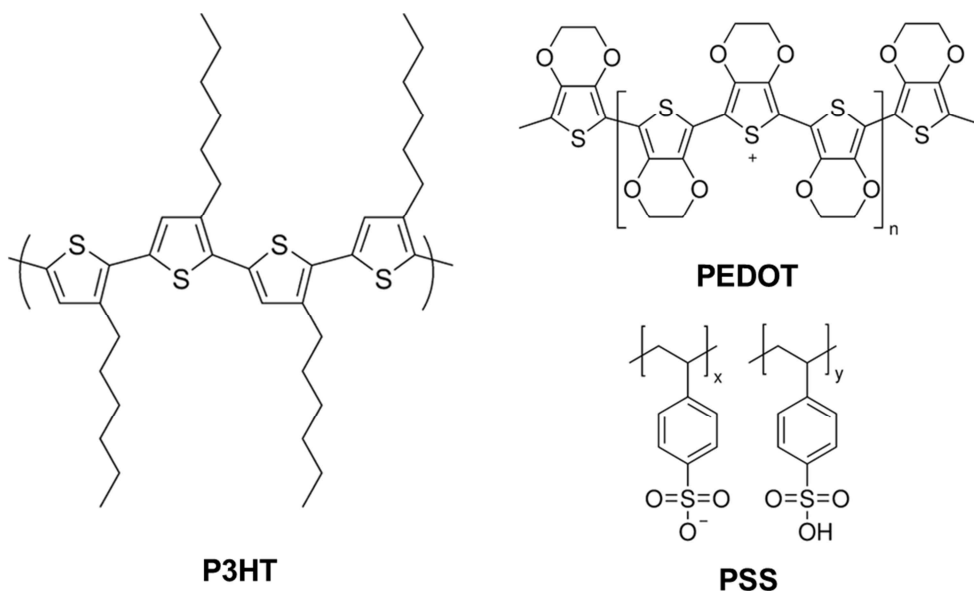
Figure 2.5 Chemical structure of the P3HT and PEDOT:PSS.

2.3   Device Fabrication Methods

The polymer:NC hybrid solar cells were fabricated based on all-solution process except metal electrode. Patterned indium tin oxide (ITO) glass substrates (~10 Ω/□) were cleaned in an ultrasonic bath with acetone, isopropyl alcohol, and deionized water, respectively for 20 min, and then blow-dried with a N2 stream. Then, PEDOT:PSS solution for hole buffer layer or ZnO NPs solution for electron buffer layers were spun-casted. After soft baking, P3HT:CdSe QD blend solution or CdSe TPs solution were spun-casted. On the top of that, Al electrodes (100 nm) or MoO_3 (for hole extraction layer, 10 nm)/Al (100 nm) were deposited via thermal evaporation. The active area of these solar cells was 0.09 cm^2. Detailed fabrication methods for the solar cells (P3HT:CdSe QD BHJ solar cell, P3HT/CdSe TPs HJ solar cell) will be described in the each chapter.

31

2.4   Thin Film Characterization Methods

UV-Visible absorption: UV-Visible absorption spectra were measured using an Agilent 8454 UV-Vis diode array spectrometer in room temperature.

Nuclear magnetic resonance (NMR) spectrascopy: Surface coverage of ligands was characterized by using a 500 MHz 1H-NMR instrument manufactured by Brunker Corporation, using $CdCl_3$ as a solvent and bromoform as internal concentration reference. In order to remove reaction byproducts in NC dispersion or weakly-bound ligands on NCs, every sample for 1H-NMR were purified three times with methanol and chloroform, and dried under N2 atmosphere for 10 min.

Auger electron spectroscopy: Atomic contents of the polymer:NC hybrid films were characterized by an Auger electron spectroscopy (Perkin-Elmer PHI 660), equipped with a LaB6 electron gun, an Ar ion beam, and a cylindrical mirror analyzer.

Fourier transform infrared (FT-IR) spectroscopy: FT-IR spectra of NCs films were acquired using a Perkin-Elmer Frontier FT-IR spectrometer in a transmission mode. All samples were fabricated on dual-side-polished Si wafer for characterization, which prevents the accumulation of charge during the radiation of high-energy beam or light scattering during the transmission of infrared beam.

Electron microscopy: Transmission electron microscopy (TEM) images of NCs and polymer:NC BHJ films were taken using a JEOL JEM-2100 and a JEM-3010. Top and cross-sectional Scanning electron microscope (SEM) image of CdSe TP networks and polymer:TPs hybrid films were taken with a Carl Zeiss SUPRA 55VP.

2.5   Device Characterization Methods

J-V characteristics: Typical *J-V* characteristics of the solar cells were measured using a Keithley 237 source measurement unit under AM1.5G condition and an illumination intensity of 100 mW/cm2 generated by a Newport 91160A solar simulator. Incident light power was varied with neutral density filters. For temperature-dependent *J-V* measurements between 200 and 300 K, the solar cells were loaded on to the cold finger of a closed-cycle He cryostat with LakeShore 331 temperature controller.

Incident photon to current conversion efficiency (IPCE): IPCE was measured using an Oriel QE/IPCE Measurement Kit which was composed of a 300W xenon lamp, a monochromator (74125), an order sorting filter wheel, a Merlin lock-in amplifier (70100) and a chopper.
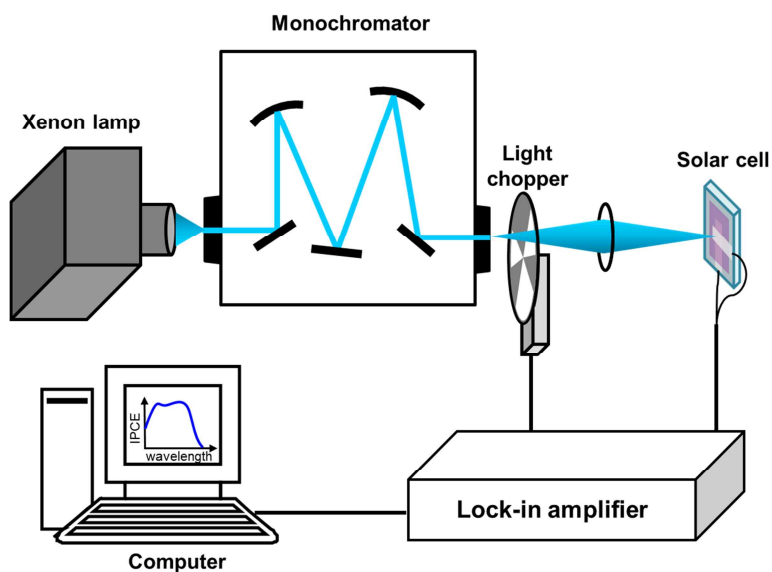
Figure 2.6 Schematic diagram for IPCE measurement set-up.

Chapter 3

Influence of Ligand Exchange /Elimination Procedure on CdSe Quantum/P3HT Hybrid Solar Cell Performance

The surface ligands surrounding NCs are recognized as important factor to determine their colloidal stability as well as electrical characteristics. In the early stages, to eliminate long alkyl chain ligands and to attain better exciton dissociation and carrier transporting properties, as-synthesized NCs were modified by pyridine. However, the pyridine-based ligand exchange has several drawbacks: a long reaction time varying from several hours to days as well as poor colloidal stability. Because of the small size of pyridine molecule, the QDs capped with pyridine

cannot be sufficiently stabilized by the steric effect. In addition to these constraints, the formation of surface states originating from the non-bonding orbital of surface atoms has been regarded as the critical limitation to achieve highly efficient hybrid solar cells [21, 50].

Against to those drawbacks, alternative modification methods have been suggested to avoid the pyridine treatment and to reduce an insulating organic shell. For instance, Olson *et al.* reported the effect of short butylamine ligands on the performance of poly-3-hexylthiophene (P3HT):CdSe QD solar cells comparing with several other ligands such as pyridine, steric acid, tributylamine, and oleic acid [35]. Radychev et al. also reported the superiority of butylamine ligands over pyridine— butylamine ligands had better passivation of Cd-dangling bonds while pyridine introduced additional hole traps [21]. In the meantime, Zhou et al. demonstrated that the organic shell comprised of hexadecylamine was easily reduced by the addition of hexanoic acid [20]. Thanks to the reduced resistance at the interface, P3HT:CdSe QD solar cells with a thin ligand shell showed considerable improvement in power conversion efficiency (PCE).

However, in spite of the improvement in device performance, the chemical status of surface modified QDs still has not been clear; remnant or exchanged surface ligands and thickness of surface ligand shell are sensitively altered by temperature, concentration of additional ligands, and reaction time. Because of this complexity most reports have only described about the device performance before and after surface modification of QDs. Moreover, Lokteva et al. reported that insufficient removal of surface ligands of QDs results in higher solar cell performance than perfect removal of the surface ligands [50]. It is therefore important to understand intermediate states during surface ligand manipulation and their influence on solar cell performance.

In this context, we investigated the relationships between surface chemistry changed by surface treatment (i.e., amount of surface ligands exchanged and average ligand chain length) and correlated device physics (i.e., charge separation, extraction, and recombination) in polymer:QD solar cells.

We selected two kinds of short alkyl chain ligands, such as weakly bound alkylamine ligand (1-hexylamine) and covalently bound carboxyl acid ligand (hexanoic acid) to investigate the influence of the surface treatment on insulating ligand shell of CdSe QDs. Through the ^{1}H-NMR analysis, we observed different nature of ligands exchange according to functional group and process sequence, and correlated their effect on P3HT:CdSe QD BHJ solar cell performances (current density-voltage (*J-V*) characteristics, incident photon-to-current conversion efficiency (IPCE)). Photogenerated charge carrier collection properties in active layers were studied using incident light intensity dependent *J-V* characteristics. Device performances depending on the thickness of active layer and donor: accepter blend ratio and the effect of thermal annealing were also investigated.

3.1 Fabrication of P3HT:CdSe QD BHJ Solar Cells

The P3HT:CdSe QD solar cells with the structure of ITO/PEDOT:PSS/P3HT:CdSe QD/Al were fabricated by following method. 1.5 wt% of P3HT solution in dichlorobenzene and 1.5 wt% of CdSe QD solution in chloroform were blended with 1:3 wt/wt ratio for making P3HT:CdSe QD blend solution.

In the meantime, patterned ITO glass substrates (~10 Ω/□) were treated with oxygen plasma for 10 min, and then, PEDOT:PSS was then spin-coated onto the

substrate (4000 rpm, 30 sec). The films were annealed in a vacuum oven at 120 °C for 30 min. The resulting PEDOT:PSS film thickness was 60 nm.

Subsequently, the P3HT:CdSe QD solutions were deposited through spin-casting at 1000 rpm. The thickness of P3HT:CdSe QD films were around 90 nm.

On the top of that, Al electrodes (100 nm) were deposited via thermal evaporation. Fabricated solar cells were post-annealed on a hot plate in an Ar glove box at 150 °C for 10 min.

As shown in the energy band diagram in Figure 3.1, the energy levels of CdSe QDs, taken by a photoemission spectroscopy and optical band, and P3HT make type II band alignment which is favorable for exciton separation. The energy level of CdSe QDs was in agreement with the value in a previous report [51].
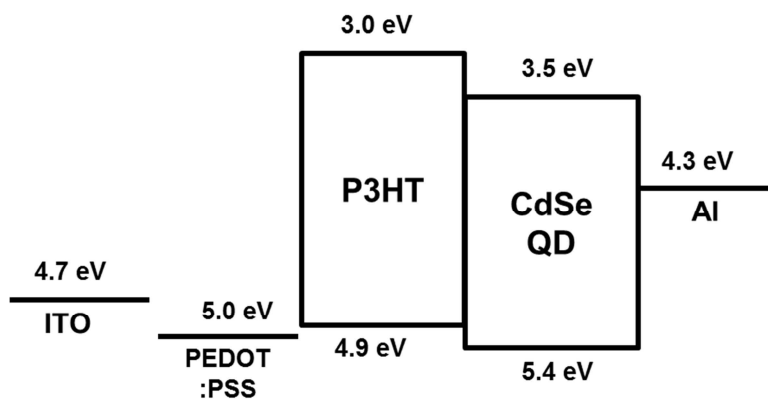
Figure 3.1 Energy band diagram of P3HT:CdSe QD BHJ solar cell
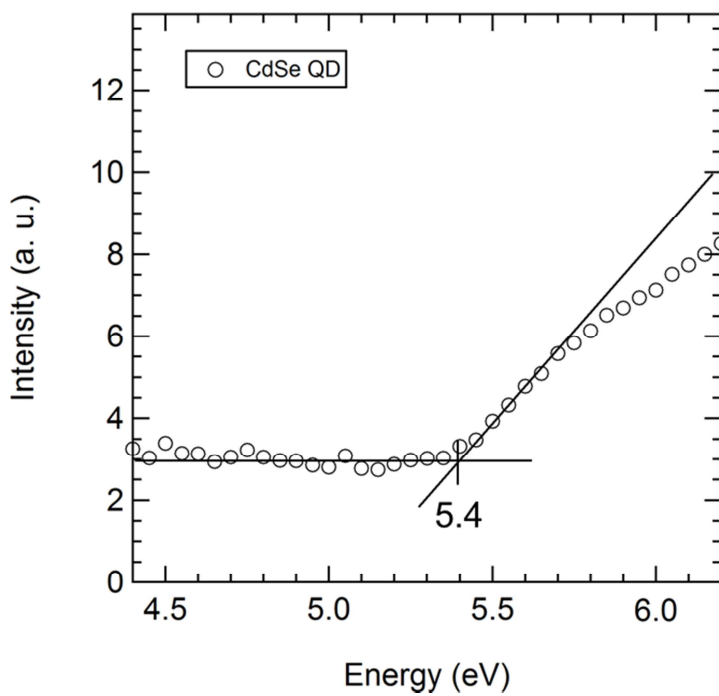
Figure 3.2 UPS spectrum of the as synthesized CdSe QDs.

3.2 Ligand Exchange/Elimination of CdSe Quantum Dots

3.2.1 Surface Modification Procedure of CdSe QDs

As-synthesized CdSe QDs have two or more ligands originating from the reaction condition such as unreacted cadmium oleate, n-trioctylphosphine selenide (SeTOP), n-trioctylphosphine, oleylamine, or unknown byproducts. The presence of various ligands impedes the accurate examination of surface ligands and their change during surface modification process. Therefore, we thoroughly purified the QDs with chloroform and acetone/methanol to remove excess ligands and byproducts, and then, we added hexanoic acid (HA) or 1-hexylamine (HAm) for the surface modification. In terms of surface modifications procedures, we prepared four different CdSe QDs (see, Figure 3.3), which are pristine CdSe QDs capped with oleate ligands (CdSe A), QDs ligand-exchanged with HAm (CdSe B) or HA (CdSe C), and QDs sequentially ligand-exchanged with HA followed by HAm (CdSe D). The absorption spectra of ligand-exchanged CdSe QDs had same spectra with pristine CdSe QDs (Figure 3.4). This denotes ligand exchange dose not deteriorate physical properties of pristine QDs, such as, radius of QD and optical band-gap.

Figure 3.5 shows the TEM images of pristine and ligand-exchanged QDs. The removal of oleate ligand on pristine CdSe QDs can be represented by decrease of inter-dot distance after sequential ligand exchange. The size of CdSe QD was estimated to be 5.4 nm from the first excitonic absorption peak (figure 1(b)) [52] and confirmed by TEM image.
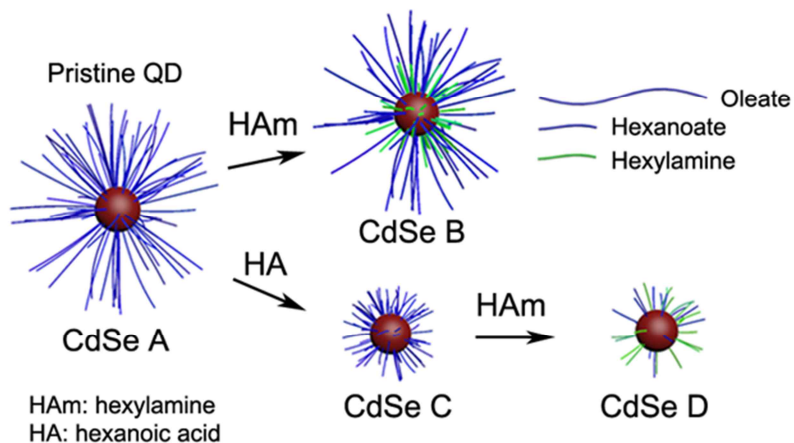
Figure 3.3 Schematic diagram of the ligand exchanging and elimination procedure.
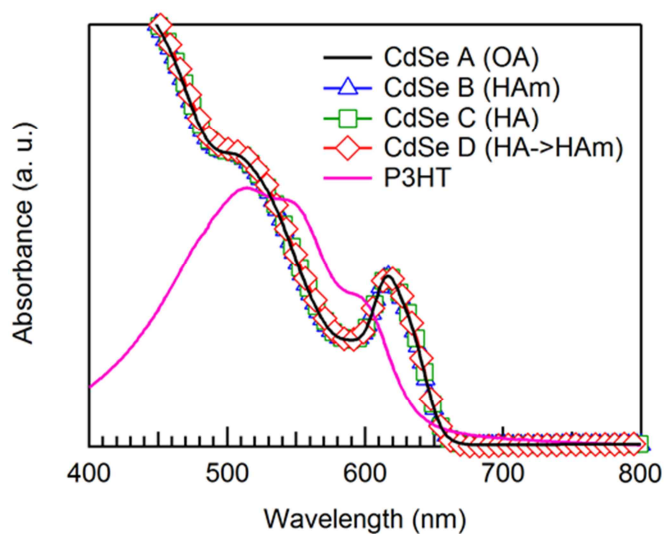
Figure 3.4 Absorption spectra of the pristine CdSe QD and ligand-exchanged CdSe QDs (avg. d ~ 5.4 nm) and P3HT thin film.
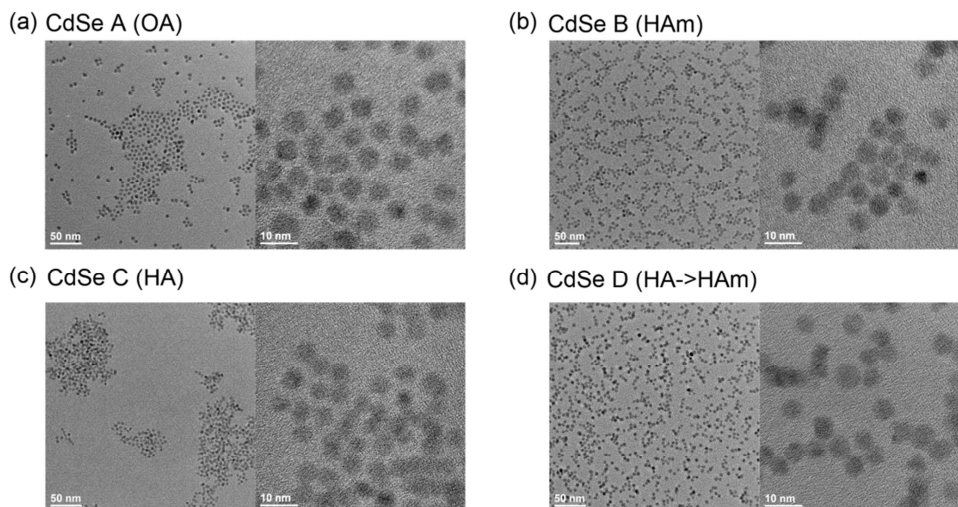
Figure 3.5 TEM images of CdSe QDs with four different CdSe QDs: (a) as-prepared (oleate capped), surface modified with), (b) hexylamine, (c) hexanoic acid and (d) hexanoic acid followed by hexylamine.

3.2.2 Quantitative Analysis on the Surface Ligands of CdSe QDs

Before ^{1}H-NMR measurement, we purified the resulting QDs for three times in order to exclude excess of ligands after surface modification process. In the case of CdSe A, phosphorus and amine species were not detected by ^{1}H-NMR (Figure 3.6) and ^{31}P-NMR (Figure 3.7), but signals from oleate ligands were only observed. Broadened resonance peak at 5.3 ppm (denoted as (i) in Figure 3.6(a)), from two protons bound to a double bond, is a characteristic peak of oleate ligands. For the quantitative analysis on the surface ligands, we focused on the signals from 0 to 3.4 ppm (denoted as (ii) and (iii) in Figure 3.6 (a)) in ^{1}H-NMR spectrum, representing the protons in saturated alkyl chains ((ii) for -CH_3 and (iii) for -CH_2-). The integrated area from 1 ppm to 3.4 ppm contains the total number of protons in the -

CH$_2$- units. In addition to the integrated area from 1 to 3.4 ppm, a sharp peak at ~ 0.9 ppm (denoted as (ii) in Figure 3.6 (a)) reflects the total amount of protons at the end of alkyl chains (-CH$_3$) and enables us to quantify the number of surface ligands in the sample. All ligands have one terminal methyl group, thus, the peak at 0.9 ppm is directly related to the amount of overall alkylchain. Based on this information, we can establish a barometer of the amount of surface ligands: the ratio of overall proton ((i) + (ii) + (iii)) integral to terminal proton (ii) integral, defined as a proton ratio ($R_{O/T}$). For instance, the theoretical $R_{O/T}$ of oleate is calculated as 10.33 (= 31/3) and it will be decreased as the oleate ligands are removed or exchanged with shorter alkyl chains. Although such information is not faithfully correlated with the exact average of two or more ligands with different end groups, it gives us an insight on the change in thickness of insulating ligands shell during surface modification process.

In addition to the $R_{O/T}$, the resonance peak (ii) shows us the information about the areal density of surface ligands: dividing the total amount of terminal carbons by overall surface area of QDs (i.e., C_{-CH3} / $4\pi r^2 C_{QD}$, where C_i is concentration of i, respectively and r is average radius of QDs. See Experimental Section for detailed procedure). The average areal density of surface ligands can be calculated from following information: molar concentration of ligands and QDs as well as the diameter of QDs. All surface ligands involved in the present study have a terminal -CH$_3$ group, thus, dividing the molar concentration of protons in -CH$_3$ by 3 (proton ratio) yields the molar concentration of surface ligands (C_{-CH3}). First of all, C_{-CH3} can be calculated using the integration area of -CH$_3$ peak (at 0.9 ppm, for three photons) and CHBr$_3$ peak (at 6.8 ppm, for one photon) as follows;

$$C_{-CH_3} = \frac{\text{Integration area of - CH}_3 \text{ peak} \Big/ 3}{\text{Integration area of bromoform peak}} \times \text{Conc. of bromoform (50 mmol/L)}$$

where the bromoform was used as the concentration reference. Next, the diameter and concentration of QDs are estimated from the absorption spectra of QDs in the NMR samples. Known amount of QD solution (0.05 mL) is extracted from the NMR samples and diluted them using chloroform (1/1010) to acquire the position of 1st exciton peak and its optical density. The diameter of QDs is estimated from 1st exciton peak-diameter correlation by Yu *et al.* [52] and an empirical absorption coefficient (ε, in L / mol cm) is calculated from a diameter-absorption coefficient relationship. For instance, 1st exciton peak at 617 nm yields 5.4 nm of diameter and 5.2×10^5 L / mol cm of absorption coefficient. Using those information, the molar concentration of QDs (C_{QD}), ranging hundreds of μmol/L, yields based on Beer-Lambert law ($A = C_{QD} \times \varepsilon \times d$, A is an optical density of QDs at 1st exciton peak and d is a light beam path of the cuvette, 1 cm). Finally, the concentration of surface ligands (C_{-CH3}) divided by the product of a surface area of a QD and molar concentration of QDs ($\pi d^2 C_{QD}$) gives the areal density of surface ligands.
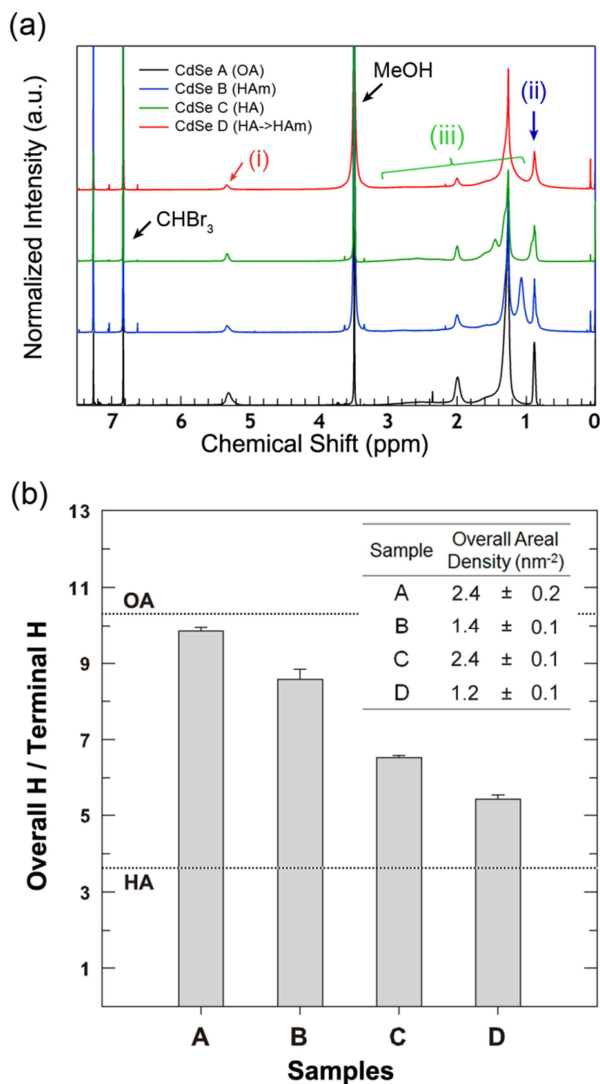
Figure 3.6 (a) ^{1}H-NMR spectra of oleate capped QDs (CdSe A, black), HAm exchanged QDs (CdSe B, blue), HA exchanged QDs (CdSe C, green), and sequentially exchanged QDs (CdSe D, red). The peaks are classified into three types: from double bond (-CH=CH-, denoted as (i)), the end of alkyl chain (-CH$_3$, denoted as (ii)), and the middle of alkyl chain (-CH$_2$-, denoted as (iii)). (b) The ratio of overall proton to terminal proton ($R_{O/T}$) of the CdSe QDs. The areal density of the ligands is listed as a table.
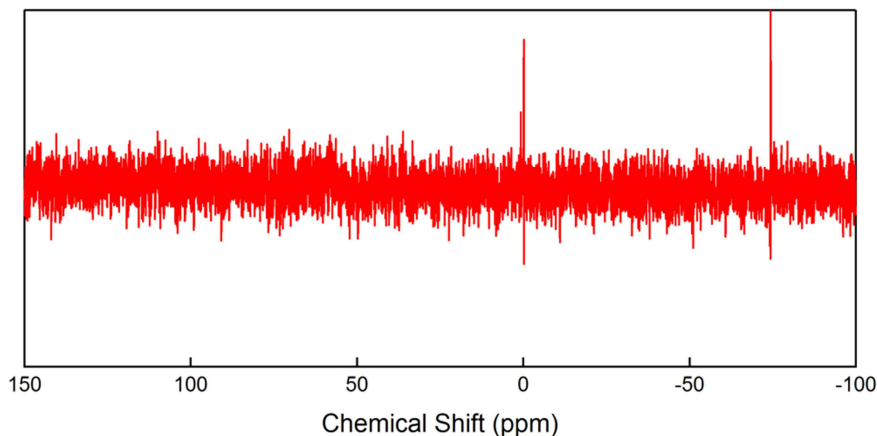
Figure 3.7 ^{31}P-NMR spectrum of oleate capped QDs (CdSe A) after purification.

Change in the $R_{O/T}$ and overall areal density of surface modified QDs are summarized in figure 2(b). For the CdSe A, the $R_{O/T}$ is smaller than the theoretical value due to impurity in oleic acid (~ 90%, technical grade) used in the synthesis of QDs. The surface treatment with HA or HAm showed fairly different tendency on the $R_{O/T}$ and areal density. The CdSe B exhibited decreased the $R_{O/T}$ to 8.6 and overall areal density to 1.4 nm^{-2}, while CdSe C had decreased the $R_{O/T}$ to 6.5 but hardly changed the overall areal density. This difference stems from the reaction mechanism of HAm and HA to QD surface.

In a case of HAm, the oleate ligands are removed from the QD surface as a form of cadmium carboxylate, coordinated with amines [53]. However, we observed the presence of residual HAm in CdSe B (a sharp peak at 1.1 ppm from ^{1}H NMR, signal from alpha-carbon was diminished due to heavy broadening). This can be considered that HAms are captured within alkyl chain ligands by hydrophobic interaction, which impedes the reduction in the ligand shell. The amine-assisted elimination of oleate is so slow that the surface modification requires long reaction

45

time or high temperature. In the present study, the reaction time was fixed at 15 min and HAm was washed out immediately, so the oleate ligands were not fully eliminated from QDs.

On the contrary in the case of CdSe C, the HA doesn't eliminate the cadmium oleate, but replace oleate ligands by proton transfer pathway. Thus, it hardly changes the number of surface ligands and only reduces the average length of ligands (namely, $R_{O/T}$ is decreased). Although every oleate ligand was not completely exchanged with HA under given reaction condition, it is clear that HA is more effective ligand than HAm for reducing the insulating ligand shells.

In contrast to the small decrease in an areal density of CdSe B, sequential treatment of HA followed by HAm (CdSe D) significantly reduces the $R_{O/T}$ to 5.4 and areal density to 1.2 nm^{-2}. This considerable difference is responsible for the steric hindrance effect of oleate ligands; the oleate ligands prevent the approach of HAm to inner region of ligand shell, so the elimination of ligands is retarded. Once the ligands are exchanged with HA, then, HAm can more effectively penetrate into the ligand shell and resulting cadmium oleate-HAm complex also easily escape from the ligand shell. Therefore, the sequential treatment of CdSe QDs with HA followed by HAm accomplishes the fast and effective reduction in the insulating ligand shell.

3.3   P3HT:CdSe QD BHJ Solar Cell Performances

3.3.1   Donor:Acceptor Blend Ratio Dependence of P3HT:CdSe QD BHJ Solar Cells

In this study, *J-V* characteristics of various polymer:CdSe QD blend ratio were investigated. The blend ratio is significant factor for determine solar cell efficiency since blend ratio related with the optical and electrical characteristics of active layer. Therefore, finding the optimal ratio is crucial for efficient device operation. We characterized blend ratio (from 43–87% of QD wt. ratio) of hybrid solar cells with CdSe QDs which were prepared with sequential ligand exchange of HA followed by HAm. The solar cells were fabricated with a structure of Figure 3.8.
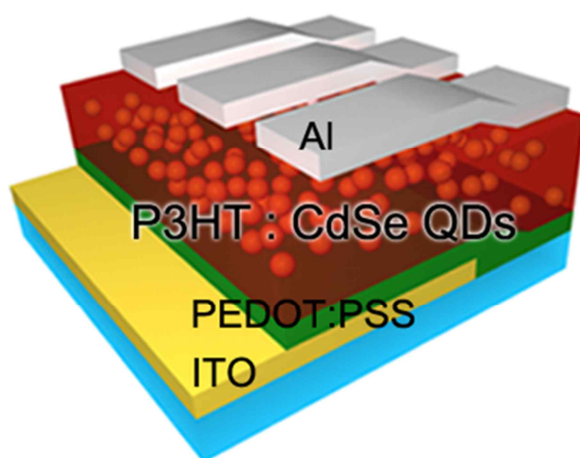
Figure 3.8 Device structure of P3HT:CdSe QD hybrid BHJ solar cells.

A Percentage of QD wt. occupation ratio was calculated from polymer:QD blend ratio. The QD wt. ratio below 75% could not achieved reasonable solar cell performances. This can be interpreted that high QD population is required to interconnect each other for efficient electron transport. When the ratio of QDs is increased, J_{SC}, V_{OC}, and FF increased and this denotes efficient charge transport of electron and hole thorough QDs and high built in potential with optimal donor:acceptor ratio. Over the 75% of QD wt. ratio, J_{SC} start to decrease. This can be caused by decreased interface area between QD and polymer with high QD concentration.
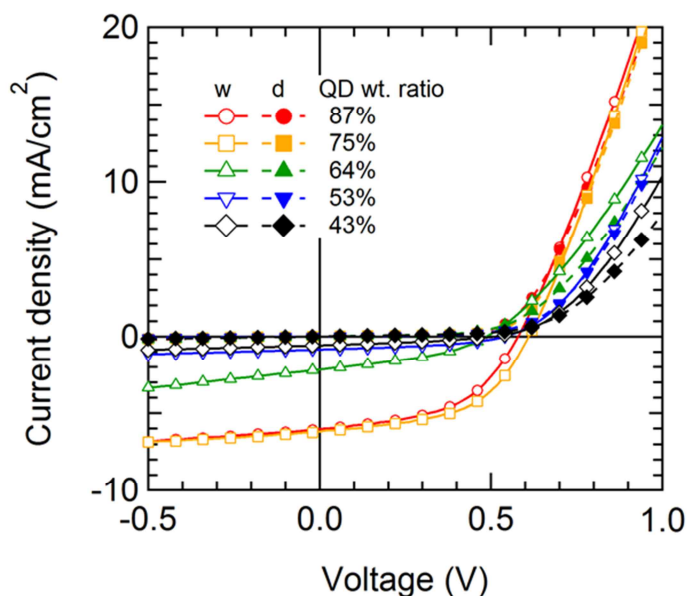
Figure 3.9 *J-V* curves of P3HT:CdSe QD BHJ solar cells as a function of polymer:QD blend ratio under AM1.5G 1sun illumination.
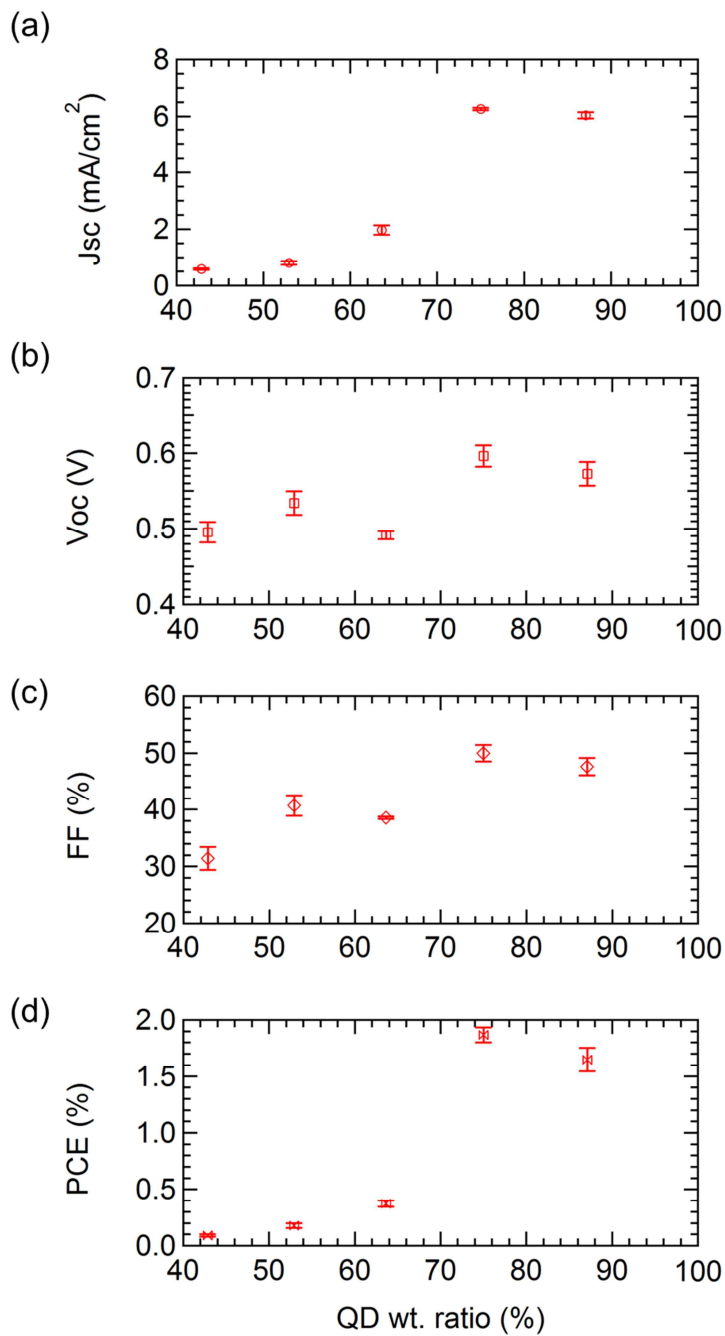
Figure 3.10 Variation of (a) J_{SC}, (b) V_{OC}, (c) FF and (d) PCE as a function of QD wt. ratio. The average values and error bars are derived from four individual cells on the same substrate.

Table 3.1 Blend ratio dependence of hybrid solar cell performances under the AM 1.5G 1sun illumination (average values of J_{SC}, V_{OC}, FF, PCE from four individual cells on the same substrate).

Polymer:QD wt. ratio	QD wt. ratio (%)	J_{SC} (mA/cm^2)	V_{OC} (V)	FF (%)	PCE (%)
1 : 6.75	87	6.03	0.57	47.6	1.65
1 : 3	75	6.27	0.60	50.0	1.87
1 : 1.75	64	1.97	0.49	38.6	0.37
1 : 1.125	53	0.81	0.53	40.7	0.18
1 : 0.75	43	0.59	0.50	31.4	0.09

From the incident light intensity dependence of J_{SC} (Figure 3.11), we can evaluate charge carrier recombination characteristics with light intensity scaling exponent (α). The α had similar values of 0.83–0.85, for all blend ratios. This denotes recombination characteristics weakly depend on the blend ratios but strongly depend on the surface chemistry from previous experiments.

Figure 3.12 shows IPCE spectra of solar cells with various blend ratios. IPCE spectra exhibited different shape with the blend ratios. As expected, the solar cell with high QD concentration had pronounced IPCE at the CdSe QD absorption region, while at the low QD concentration, IPCE had pronounced at P3HT

absorption region. At the 75% of QD wt. ratio, both of P3HT and QD absorption region had high IPCE, denoting optimal blend ratio.
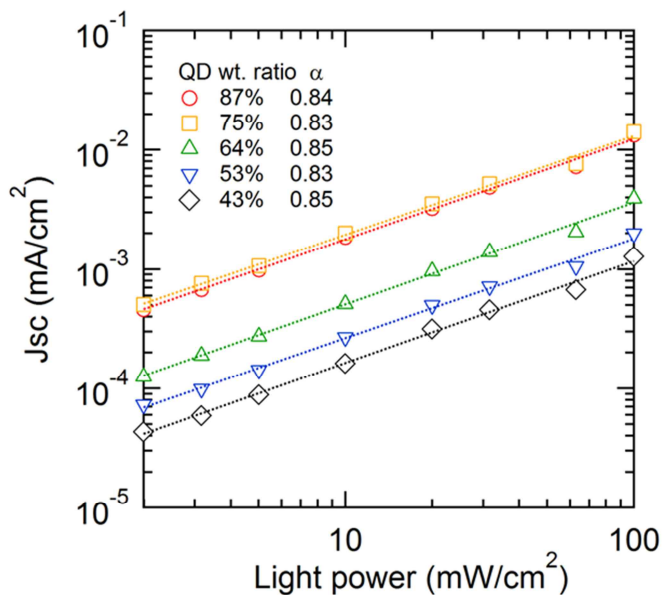
Figure 3.11 Light intensity dependence of J_{SC} as a function of QD wt. ratio. The light intensity scaling exponents (α) are summarized in the legend.
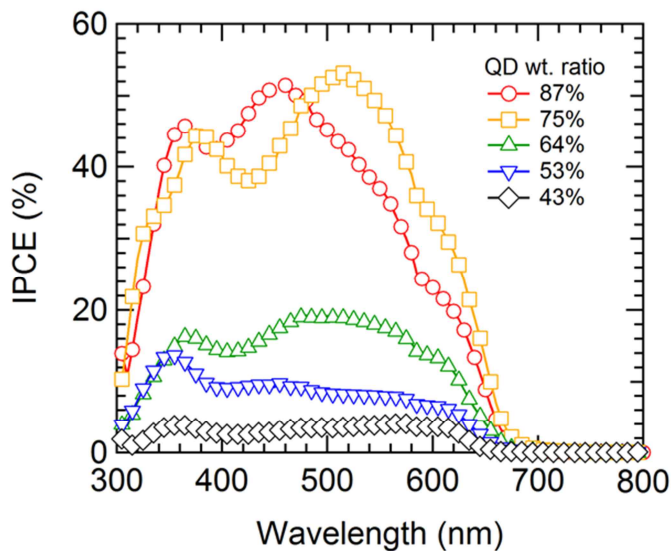
Figure 3.12 IPCE spectra of P3HT:CdSe QD BHJ solar cells as a function of QD wt. ratio.

3.3.2 Active Layer Thickness Dependence of P3HT:CdSe QD BHJ Solar Cells

In BHJ solar cells, thickness of active layer is also important factor for device operation. Thicker films can absorb more photons while thinner films have smaller series resistance, which intimately relate with the *FF*. We characterized blend thickness dependence (30–200 nm) of hybrid solar cells with CdSe QDs which were prepared with sequential ligand exchange of HA followed by HAm.

Figure 3.13 shows *J-V* curves of hybrid solar cells depending on thickness of active layer. The blend ratio of solar cells were fixed 1:3 wt. ratio of P3HT:CdSe QD. The hybrid solar cell characteristics as a function of thickness of active layer are shown in Figure 3.14 and Table 3.2. R_S and R_{Sh} were evaluated from the *J-V*

characteristics under the AM 1.5G 1sun illumination. The mean values and error bars in Figure 3.14 are derived from four individual cells on the same substrate.

The solar cell with 30 nm thickness of active layer exhibited poor solar cell characteristics and hardly operate as diode. This can be understood that connection of the top and bottom electrodes due to the thin active layer. As a result of increasing thickness, the leakage path connecting the both electrodes could be suppressed, and therefore, R_{Sh} increased. However, thick active layer could cause increase of bulk resistance, which was denoted by increase of R_S, and as a result, J_{SC} decreased rapidly over the 80 nm. In addition, FF also decreased over the 100 nm. Therefore, the highest J_{SC} is achieved at the thickness of 80 nm and reasonable FF resulted optimal solar cell performance with 80 nm thickness.
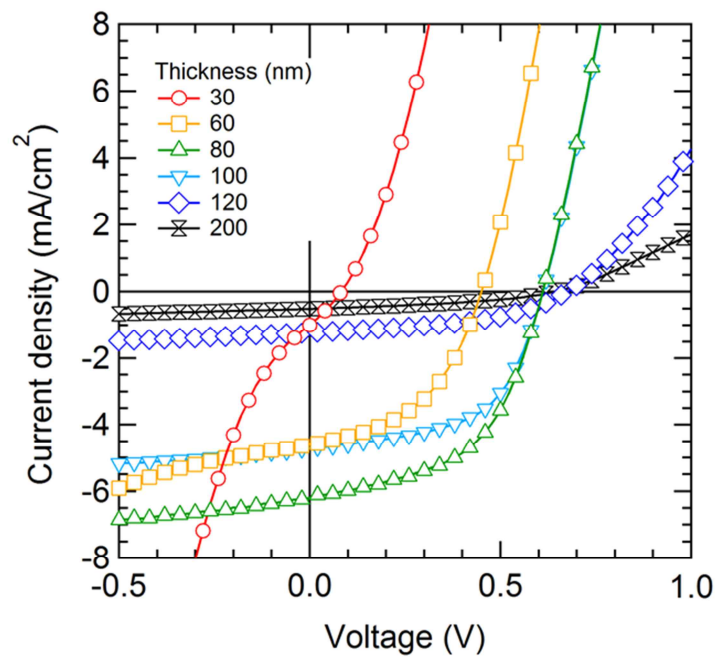
Figure 3.13 *J-V* curves of P3HT:CdSe QD BHJ solar cells as a function of thickness of active layer under AM1.5G 1sun illumination.
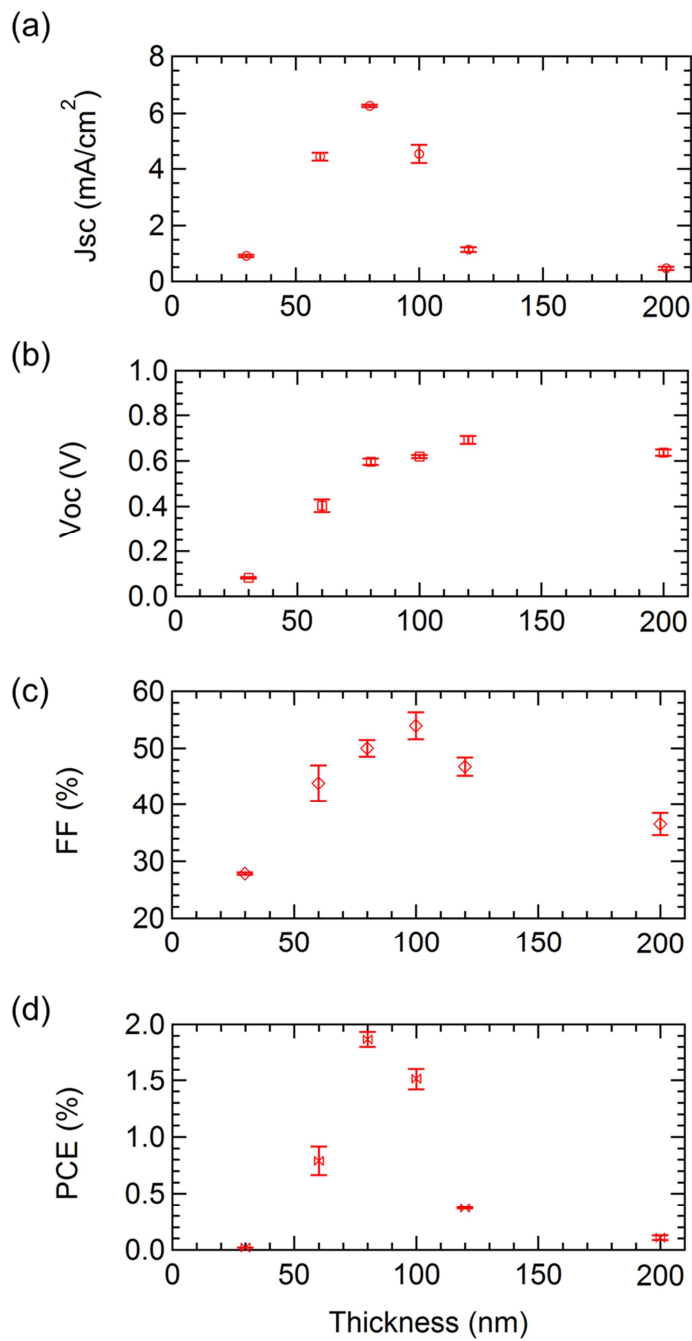
Figure 3.14 Variation of (a) J_{SC}, (b) V_{OC}, (c) FF and (d) PCE as a function of thickness of active layer. The average values and error bars are derived from four individual cells on the same substrate.

Table 3.2 Thickness dependence of hybrid solar cell performances characteristics under the AM 1.5G 1sun illumination. (The average values of J_{SC}, V_{OC}, FF, PCE are derived from four individual cells on the same substrate). R_S and R_{Sh} are evaluated from the best J-V curve.

Thickness (nm)	J_{SC} (mA/cm^2)	V_{OC} (V)	FF (%)	PCE (%)	R_S (Ω cm^2)	R_{Sh} (Ω cm^2)
30	0.93	0.08	27.8	0.02	11.5	100.6
60	4.43	0.40	43.8	0.79	11.5	439.1
80	6.27	0.60	50.0	1.87	14.9	421.1
100	4.53	0.62	54.0	1.51	14.6	795.2
120	1.16	0.69	46.8	0.37	58.8	1775.4
200	0.46	0.64	36.6	0.11	187.0	2894.4

IPCE are proportional to a product of carrier generation, dissociation and extraction efficiency. The IPCE shape except 80 and 100 nm thickness exhibited poor IPCE at the P3HT absorption region. For thick solar cells more than 120 nm, we can assume this inefficiency is caused by the poor carrier extraction and/or recombination before extraction, and then, charge collection through CdSe QDs are more efficient than through P3HT since CdSe QDs have higher mobility than P3HT. For films of CdSe QDs with small surface ligands, the electron mobilities reported to date are on the order of 10^{-2} cm^2/V·s [54-57] and hole mobilities of typical P3HT films are on the order of 10^{-3} cm^2/V·s [58, 59].

In the case of thin solar cell below 60nm, the shape of IPCE seems very similar to the IPCE of high QD wt. ratio at around 87% (see, Figure 3.12). This denotes current flows dominantly through the CdSe QDs at thin active layer. At the optimal thickness (80–100nm), the solar cells had efficient carrier extraction both P3HT and CdSe QDs.
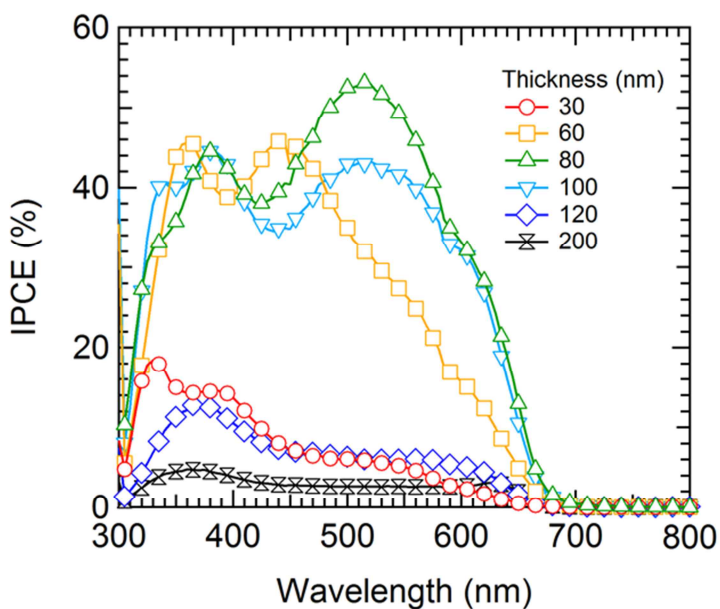
Figure 3.15 IPCE of P3HT:CdSe QD BHJ solar cells as a function of thickness of active layer.

3.3.3 Solar Cell Performances with Surface Modified CdSe QDs

The electrical properties of CdSe QDs with different ligand exchange procedures were investigated with P3HT:CdSe QD BHJ solar cells. We built devices with the structure of ITO/PEDOT:PSS/P3HT:CdSe QD (1:3 wt. ratio)/Al (Figure 3.8) using four kinds of CdSe QDs as described in Chapter 3.1; solar cells fabricated with CdSe A (pristine), CdSe B (treated with HAm), CdSe C (treated with HA), and CdSe D (sequential treatment with HA followed by HAm) are denoted as Device A, B, C, and D, respectively.

Figure 3.16 shows the current density-voltage (J-V) characteristics of the solar cells under air mass 1.5 global (AM 1.5G) 1sun illumination. Their photovoltaic performances in terms of short-circuit current density (J_{SC}), open-circuit voltage (V_{OC}), fill factor (FF), and power conversion efficiency (PCE) are summarized in Table 3.3. We found that the decrease in $R_{O/T}$, from Device A to Device D, led to the improved solar cell characteristics. Interestingly, even $R_{O/T}$ is not approaching to zero which denotes extant ligands on QDs, the Device D recorded 1.98% of PCE, 6.20 mA/cm^2 of J_{SC}, 52.2% of FF, and 0.61 V of V_{OC}, comparable to the previous reports based on CdSe QDs modified with pyridine.
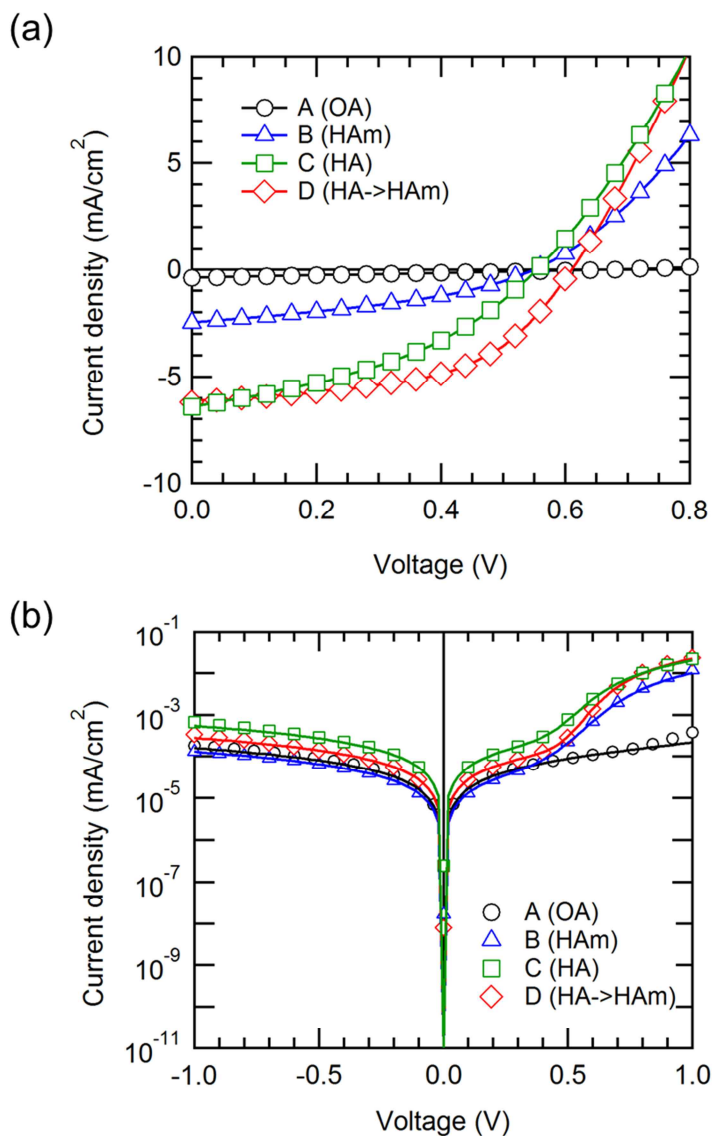
Figure 3.16 Current density-voltage *(J-V)* characteristics (a) under the AM 1.5G 1 sun illumination and (b) dark condition of the solar cells with various ligand exchanged CdSe QDs: oleate capped QDs (A, black circle), HAm exchanged QDs (B, blue triangle), HA exchanged QDs (C, green square) and sequentially exchanged QDs with HA followed by HAm (D, red diamond).

Table 3.3 Short circuit current density (J_{SC}), open circuit voltage (V_{OC}), fill factor (*FF*), and power conversion efficiency (*PCE*) of the P3HT:CdSe QD BHJ solar cells with various ligand exchanged QDs under AM1.5G 1sun illumination.

Device	J_{SC} (mA/cm^2)	V_{OC} (V)	*FF* (%)	*PCE* (%)
A	0.39	0.68	25.3	0.067
B	2.47	0.55	37.7	0.51
C	6.41	0.55	38.9	1.38
D	6.20	0.61	52.2	1.98

The *J-V* characteristics and parameters of solar cells can be analyzed using the solar cell equivalent circuit model, as shown below (See, Chapter 2.1.2 and 2.1.3):

$$J = -J_{ph} + J_0\left\{\exp\left[\left(\frac{q}{nk_BT}(V - R_SJ)\right)\right] - 1\right\} + \frac{V - R_SJ}{R_{Sh}} + J_{rec} \quad (3.1)$$

In equation (3.1), *J* is the current density, *V* is the applied voltage, J_0 is the reverse saturation current density, *q* is elementary charge, *n* is the diode ideality factor, k_B is the Boltzmann constant, *T* is the absolute temperature, R_S is the series resistance, R_{Sh} is the shunt resistance, J_{ph} is the photogenerated current density, and J_{rec} represents an additional loss term of J_{ph} in active layer, which increases significantly with the forward voltage. Without light illumination (J_{ph} and J_{rec} = 0), the diode characteristics including J_0, *n*, R_S, and R_{Sh} can be estimated (evaluated parameters are summarized in Table 3.4). The solid lines Figure 3.16(b) denote a calculated

current density with evaluated parameters. The detailed calculation method was followed from elsewhere [60].

Table 3.4 Series resistance (R_S), shunt resistance (R_{Sh}), diode ideality factor (n), saturation current density (J_0) of P3HT:CdSe QD BHJ solar cells with various ligand exchanged QDs. R_S, R_{Sh}, n, J_0 were calculated from the dark J-V curve.

Device	R_S (Ω cm^2)	R_{Sh} (Ω cm^2)	n	J_0 (nA/cm^2)
A	726.8	5644	9.64	2210
B	24.1	7731	2.45	53.2
C	16.1	1828	1.99	30.3
D	13.4	3587	1.69	1.58

Evidently, the diode characteristics of P3HT:CdSe QD BHJ solar cells shows a significant correlation with $R_{O/T}$, connected to the thickness of insulating ligand shells. Overall, from Device A to Device D, decrease in $R_{O/T}$ by surface treatment resulted in a better diode characteristics and solar cell performance. Particularly, reduction in Rs with decreasing $R_{O/T}$ is closely related to the carrier transport between QDs, which represents an improved carrier transport between QDs by reducing the thickness of insulating ligand shell. As well as the reduction in Rs, the improvement in diode characteristics (n and J_0) implies that the insulating ligands between QDs, acting as tunneling barrier in spite of small distance ($< \sim$1.5 nm), significantly limits the extraction of photocurrent and results in low J_{SC}.

In addition to the carrier transport, we found that the insulating ligand also largely prohibited exciton dissociation at interface between P3HT and CdSe QDs. From investigation of PL quenching (Figure 3.17) and nanoscopic morphology (Figure 3.18) of P3HT:CdSe QD hybrid films, decrease in $R_{O/T}$ led to the formation of well-distributed CdSe QD aggregates and complete PL quenching. Considerable transition on the PL quenching and aggregation morphology occurred at below $R_{O/T}$ of 6.5 (Device C and D), which can cause sufficient interfacial area with direct contact between P3HT and CdSe QD aggregates network to dissociate excitons [61]. Summing up the diode characteristics, PL quenching, and nanoscopic morphologies of devices, we conclude that the reduction in the chain length of insulating ligand shell strongly improve the carrier transport as well as the exciton dissociation, even if the insulating ligands are still remained.
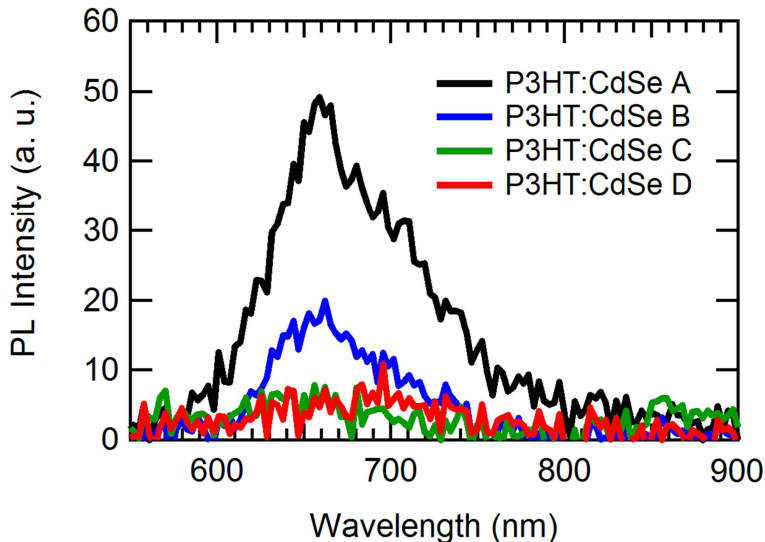
Figure 3.17 PL spectra of CdSe QD:P3HT BHJ films with various ligand exchanged QDs: oleate capped QDs (A, black), HAm exchanged QDs (B, blue), HA exchanged QDs (C, green) and sequentially exchanged QDs with HA followed by HAm (D, red).

(a) P3HT:CdSe A (OA)

(b) P3HT:CdSe B (HAm)

200 nm
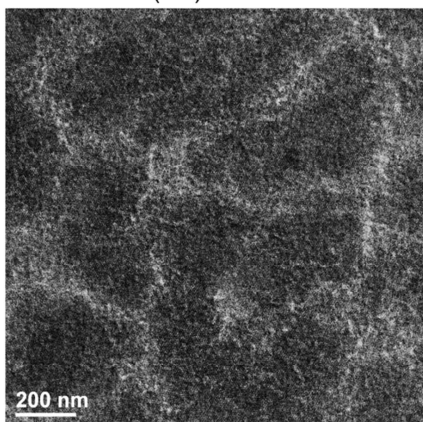
200 nm
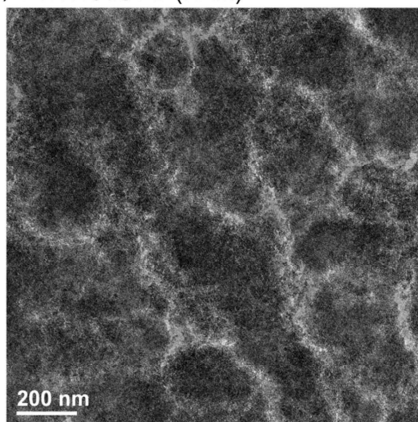
(c) P3HT:CdSe C (HA)

(d) P3HT:CdSe D (HA->HAm)

200 nm
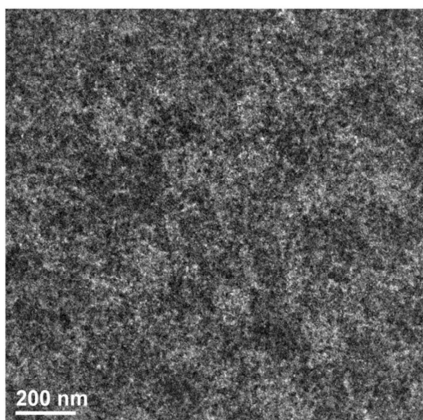
200 nm
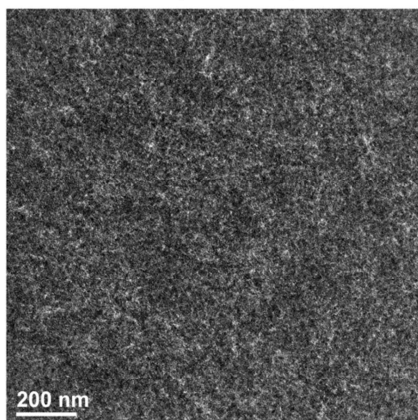
Figure 3.18 TEM images CdSe QD:P3HT BHJ films with various ligand exchanged QDs: (a) oleate capped QDs, (b) HAm exchanged QDs, (c) HA exchanged QDs and (d) sequentially exchanged QDs with HA followed by HAm.

Although n, J_0, and Rs display the clear correlation with $R_{O/T}$ as mentioned above, R_{Sh}, FF, and V_{OC} of each device represent complex behavior. Particularly, when comparing Device C with Device D, the Device C had lower FF, V_{OC} and R_{Sh} than those of Device D. The inferior FF of Device C can be interpreted as an increase in recombination current, which is indicated by the low R_{Sh} of 1828 Ω cm^2 and high n of 1.99 of Device C—Device D had higher R_{Sh} of 3587 Ω cm^2 and n of 1.69. Those variations can be understood by the influence of HAm ligands on surface states of CdSe QDs. Theoretically [62] and experimentally [21], recent publications on the surface states have suggested that the surface state can be generated, altered, or eliminated by several factors: charge imbalance due to off-stoichiometry, extra surface ligands generating or altering a midgap state, or binding modes of surface ligands. We believe that the surface states on QDs are existed in spite of the presence of covalently-bound oleate or hexanoate ligands (i.e., Device C). And those surface states act as recombination centers during carrier generation, transport, and recombination. By introducing HAm ligands subsequently (Device D), those trap states are passivated, and therefore, high FF, R_{Sh} and low n could be achieved. At the same time, low Voc of Device C can be also interpreted as the influence of surface states, based on the equivalent circuit model as below [63, 64]:

$$V_{OC} \approx \frac{k_B T}{q} \ln \frac{J_{SC}}{J_0} \qquad (3.2)$$

The reduction of V_{OC} of Device C implies that the increase of J_0 is due to the exposed surface traps, resulting in the leakage of diode current. As a result of efficient removal of oleate ligand and surface trap passivation with HAm, Device D exhibited the highest performances, 1.98% of PCE, 6.20 mA/cm^2 of J_{SC}, 52.2% of FF, and 0.61 V of V_{OC}.

Figure 3.19 plots the incident photon-to-electron conversion efficiency (IPCE) of all devices. Device C exhibited a considerable difference in the IPCE curve compared with the others. While the Device C displays a pronounce peak below 450 nm, Device B and D show two comparable peaks around 360 nm and 510 nm. Considering the absorption spectra of CdSe QDs and P3HT (see Figure 3.4), we can interpret that Device C has significant loss of photocarriers generated in P3HT domain, but Device B and D do not. Improved IPCE values of Device B and D around 510 nm are attributed to the HAm employed during the surface treatment, passivating the trap states on CdSe QDs. Taking into account the *J-V* characteristics, surface trap states of CdSe QDs capped with carboxylate ligands lead to recombination loss of photocurrent.
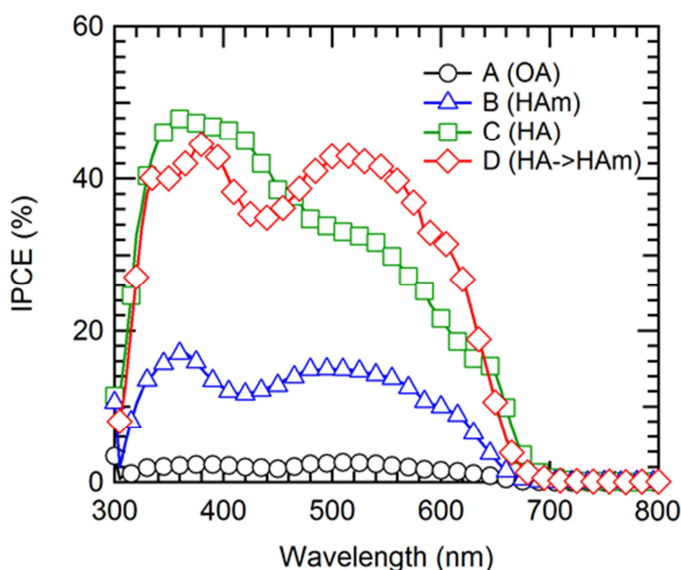
Figure 3.19 IPCE spectra of the hybrid solar cells with various ligand exchanged QDs: oleate capped QDs (A, black circle), HAm exchanged QDs (B, blue triangle), HA exchanged QDs (C, green square) and sequentially exchanged QDs with HA followed by HAm (D, red diamond).

3.3.4   Light Intensity Dependence of Hybrid Solar Cell Characteristics

We carried out incident light intensity dependent *J-V* measurement of the devices and analyzed collection voltage (V_C) [43, 44, 47] and J_{SC} [45, 46] to further investigate carrier recombination and collection characteristics of solar cells with different ligand exchange/elimination procedure.

All linear fit of *J-V* curves of various incident light intensity at short circuit conditions (*V=0*), intersect the x-axis at a single point of voltage, which is called V_C (figure 4). We can evaluate collection efficiency at short circuit condition (η_{C0}) and $\mu\tau_{eff}$ from the V_C. Voz *et al.* employed the V_C to calculate carrier collection efficiency (η_C) in polymer solar cells under these assumptions (constant electric filed, drift-driven collection and monomolecular recombination) [44].

Short circuit resistance (R_{SC}, reciprocal slopes of the *J-V* curve at *V=0*, i.e., $V_C = R_{SC} J_{SC}$) which reflects the recombination term (J_{rec}) under various light intensities and V_C can be expressed as follows.:

$$R_{SC} = \left(\frac{l_{C0}}{L/2} - 1 \right) \frac{V_{bi}}{J_{SC}} \tag{3.3}$$

$$V_C = \left(\frac{l_{C0}}{L/2} - 1 \right) V_{bi} \tag{3.4}$$

with

$$l_C = \mu\tau_{eff} \frac{V_{bi} - V}{L}, \quad l_{C0} = \mu\tau_{eff} \frac{V_{bi}}{L} \tag{3.5}$$

where l_C is a collection length, and L is a thickness of the active layer. The l_C implies the maximum travel distance of separated electron and hole driven by electric field before recombination. l_{C0} is the collection length at short circuit condition. The $\mu\tau_{eff}$ denotes effective $\mu\tau$ product, i.e, $\mu\tau_{eff} = \mu_n\tau_n + \mu_p\tau_p$. Detailed derivations of equations are provided in Supporting Information. The collection efficiency (η_C) of photogenerated charge carriers and collection efficiency (η_{C0}) at short circuit condition can be defined:

$$\eta_C = 1 - \frac{L/2}{l_C}, \quad \eta_{C0} = 1 - \frac{L/2}{l_{C0}} \tag{3.6}$$

Figure 3.20 shows J-V curves of Device B, C and D under various incident light intensity (2–100 mW/cm^2) and determined V_C by tangent of J-V curves at around $V = 0$. In the case of Device A, all linear fits at $V = 0$ doesn't intersect at a single voltage due to poor fill factor. In the case of Device B and C, linear fits under 10 mW/cm^2 doesn't intersect at a single point because the J-V curve is dominated by shunt resistance. If we consider V_{bi} of 0.7 V, the collection efficiency at short circuit condition, η_{C0} of Device B, C, and D are evaluated as 59, 63, and 72%, respectively. The corresponding $\mu\tau_{eff}$ product for $L = 90$ nm are 1.4, 1.6, and 2.1 $\times$ 10^{-10} cm^2/V, respectively, which is similar value for P3HT:PCBM solar cell [44]. Since the these coefficients are related with carrier transport, the η_{C0} and $\mu\tau_{eff}$ product had consistent tendency with J-V characteristics. This denotes again that decreasing $R_{O/T}$ provide enhanced carrier transport and moreover, passivation of traps states with HAm could achieve better carrier transport and collection efficiency.
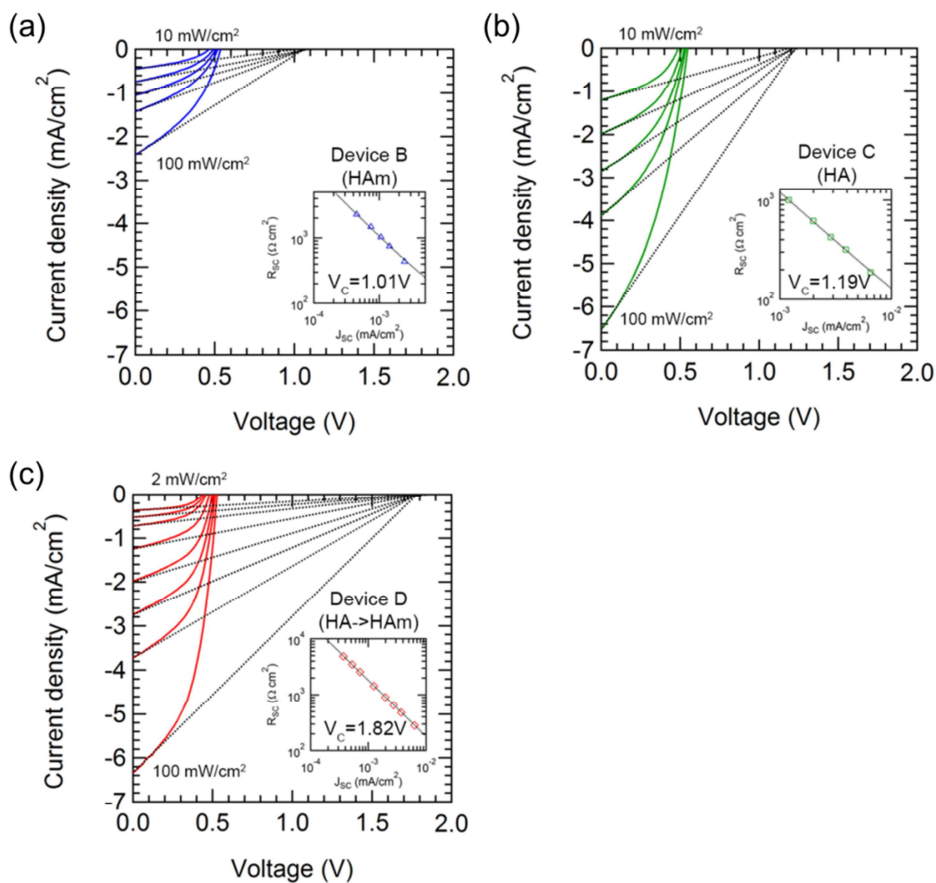
Figure 3.20 Collection voltages (V_C) of the P3HT:CdSe QD BHJ solar cells with various ligand exchanged QDs (Device B, C, and D are represented in (a), (b), and (c), respectively). The V_C is determined by the intersection of all linear fits around short circuit conditions under the various incident light intensity (2–100 mW/cm^2). Inset: extracted R_{SC} at around V = 0 and calculated V_C from the relation $V_C = R_{SC}J_{SC}$.

Table 3.5 Collection efficiency at short circuit condition (η_{C0}), $\mu\tau_{eff}$ product and incident light intensity scaling exponent (α) of P3HT:CdSe QD BHJ solar cells with various ligand exchanged QDs.

Device	η_{C0} (%)	$\mu\tau_{eff}$ (cm^2/V)	α
A	-	-	0.65
B	59	1.4×10^{-10}	0.74
C	63	1.6×10^{-10}	0.75
D	72	2.1×10^{-10}	0.89

The incident light intensity dependence of J_{SC} of the devices is shown in Figure 3.21. J_{SC} follows a power law dependence upon the light intensity (I_{light}) with the incident light intensity scaling exponent (α) which correlates with a carrier loss mechanism, i.e. $J_{SC} \propto I_{light}^{\alpha}$. The α could be interpreted as a result of competition between recombination of charge carriers and extraction before recombination. If extraction of charge carriers is faster than recombination, recombination mechanism is dominated by monomolecular recombination and α should be close to 1., whereas if the recombination of charge carries are comparable with carrier extraction, the bimolecular recombination arises and then α reduce to 0.5 [45, 46]. The α of all devices are summarized in Table 3.5.

Device A exhibited the lowest α. This denotes recombination mechanism is dominated bimolecular recombination due to the poor charge extraction with insulating oleate ligands. Device B and C exhibited similar α, having similar collection length at short circuit condition ($l_{C0} = 1.1$, and 1.2×10^{-5} cm, respectively). Device D had the highest α, meaning that the bimolecular recombination loss was suppressed owing to the efficient charge collection by the removal of oleate ligands and efficient surface trap passivation with HAm ($l_{C0} = 1.6 \times 10^{-5}$ cm, for comparison).
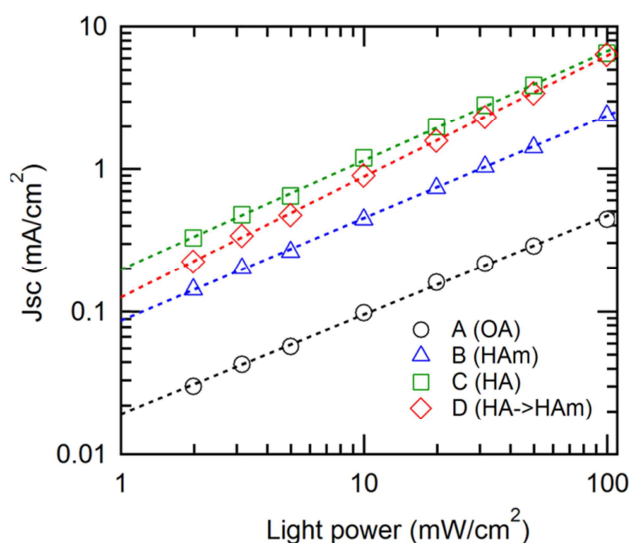
Figure 3.21 Light intensity dependence of short circuit current density (J_{SC}) of the P3HT:CdSe QD BHJ solar cells with various ligand exchanged QDs. Dotted lines denote fitted curves using $J_{SC} \propto I_{light}^{\alpha}$.

3.4 Influence of Thermal Annealing on P3HT:CdSe QD BHJ Solar Cells

3.4.1 P3HT:CdSe QD BHJ Thin Film Characteristics with Thermal Annealing

Absorption and photoluminescence (PL) experiments of CdSe QD films reveal not only optical characteristics but also physical characteristics of QDs such as surface state and aggregation of QDs. By thermal annealing at 150°C, first excition peak of CdSe QD film slightly red shift from 585 to 590 nm (Figure 3.22(a)). Red shift of first exciton absorption peak can be caused by increased electronic coupling between the QDs, which results extended band states with lower energies. The Electronic coupling will increase when the inter-dot distance decrease. Therefore, red shit of annealed film denotes reduce of inter-dot distance caused by removal of surfactant with thermal annealing.

Since PL efficiency of QDs depends on the surface traps which act as recombination center of excitons, efficient trap passivation with surface ligand is important issues for increasing PL efficiency. In the case of thermal annealed CdSe QD film, almost perfect PL quenching was observed (Figure 3.22(b)). This represents the removal of surfactant by the annealing.
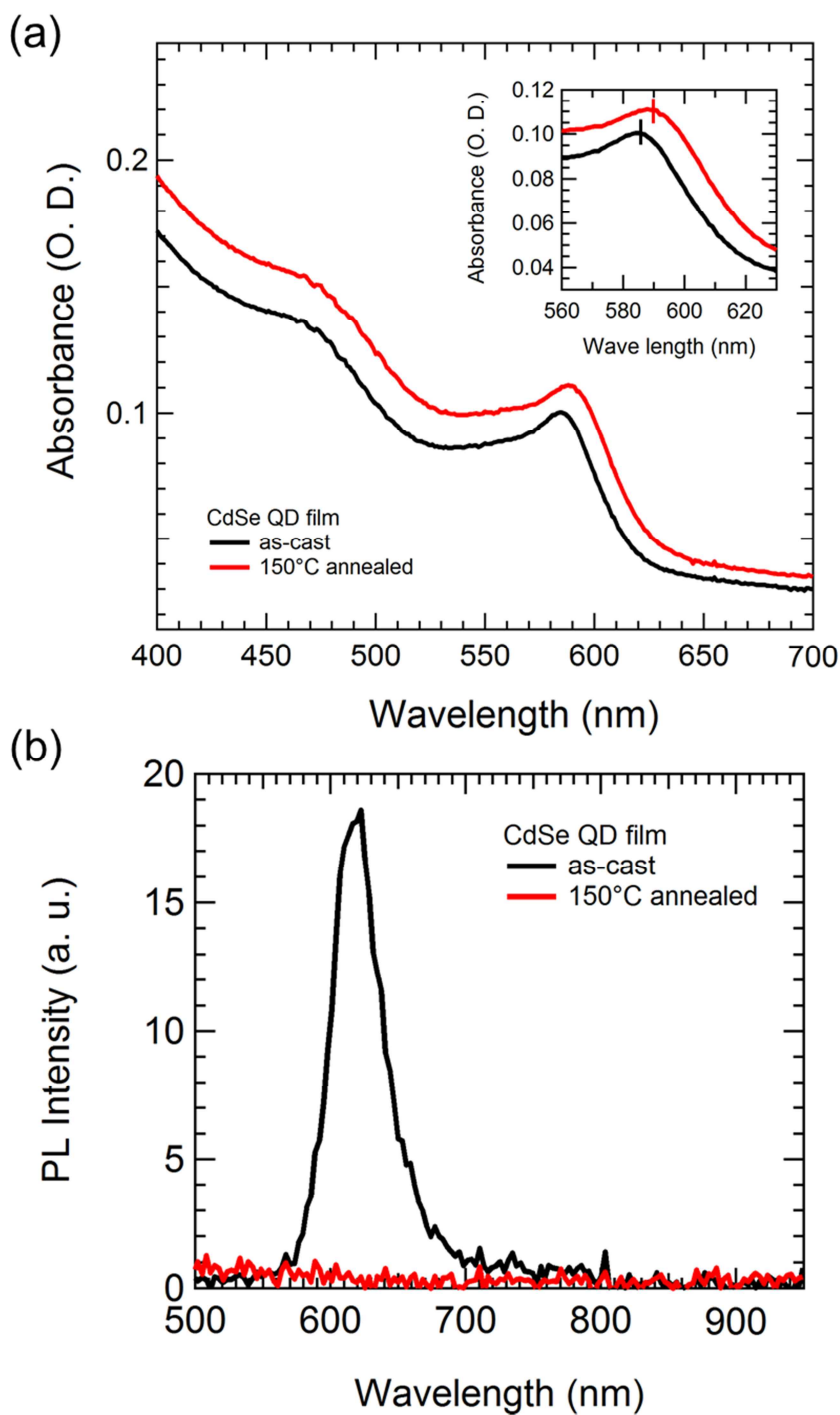
Figure 3.22 (a) Absorption and (b) PL spectra of as-cast and 150°C annealed CdSe QD film.

Absorption and PL spectra of P3HT:QD BHJ film were also investigated with thermal annealing (Figure 3.23). The BHJ films exhibited hardly change in absorption spectra but almost PL of P3HT was quenched after thermal annealing. In the case of polymer materials, vibronic absorption shoulder denotes ordering of conjugated chains. Therefore, no significant change of absorption spectrum denotes that BHJ morphology such as aggregation of QDs or polymer ordering, dosen't change by the thermal annealing. In addition, PL quenching of annealed film denotes exciton generated by P3HT dissociate more efficiently compared to as cast BHJ film since electrical interaction between P3HT and CdSe QDs are enhanced due to the removal of surface ligand.
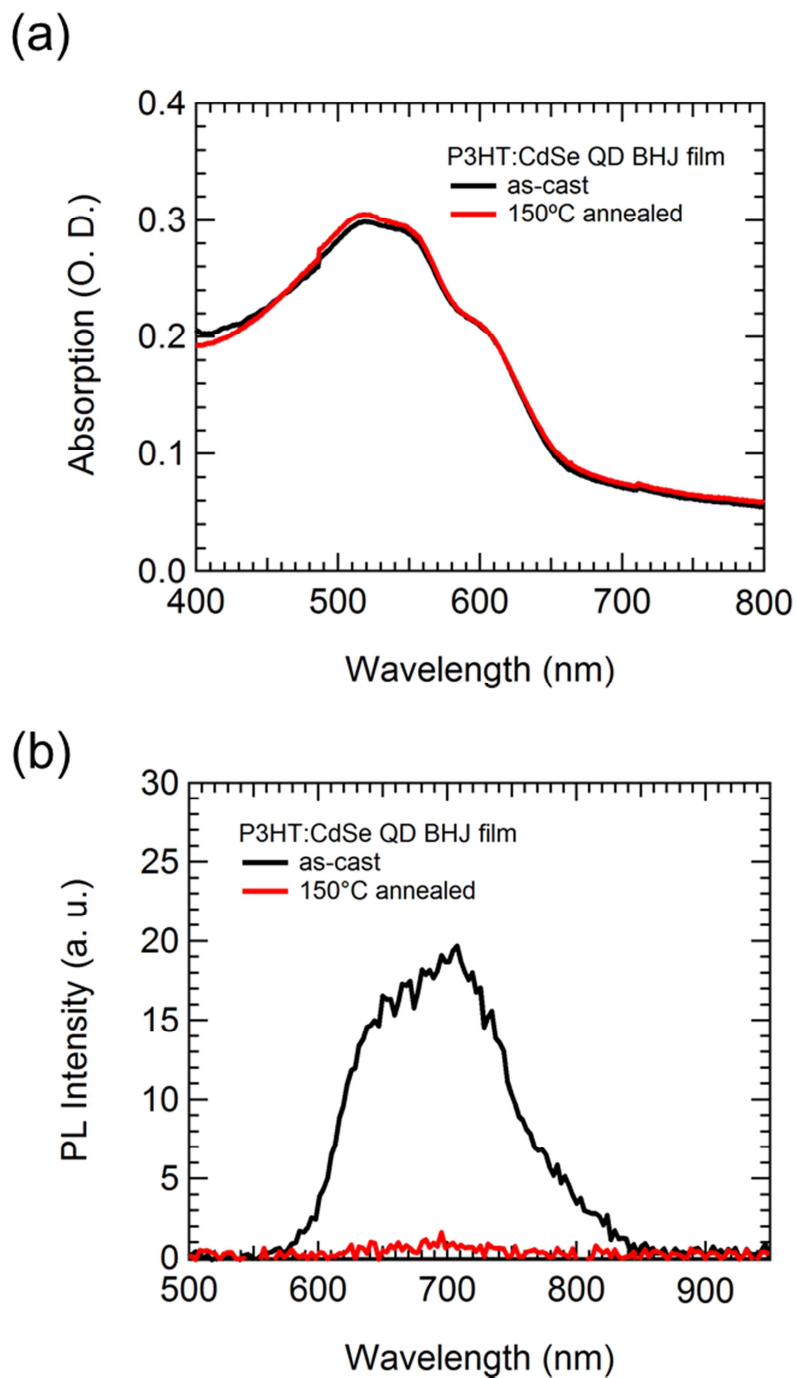
Figure 3.23 (a) Absorption and (b) PL spectra of as-cast and 150°C annealed P3HT:CdSe QD BHJ film.

Any noticeable changes in morphology of the P3HT:CdSe QD BHJ film in accordance with thermal annealing were not observed (Figure 3.24 and Figure 3.25). There was slight increase of root mean square (RMS) roughness from 18.1 to 19.2 nm after thermal annealing but the phase image of as-cast and annealed P3HT:CdSe QD films had similar grain size.
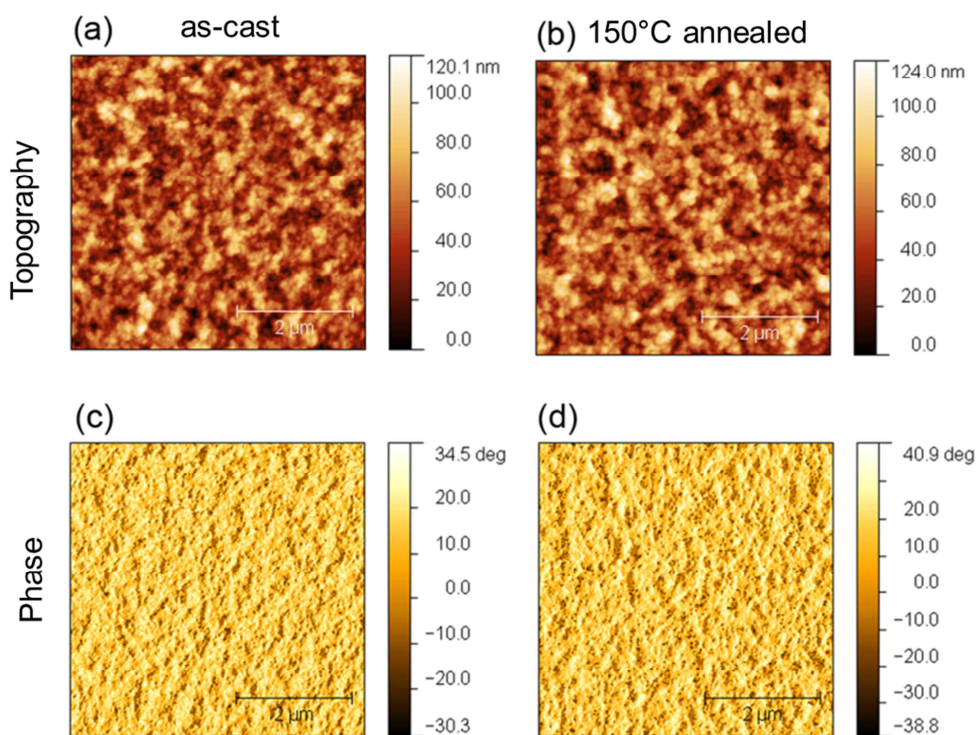
Figure 3.24 (a, b) AFM topography and (c, d) phase image of as-cast and 150°C annealed P3HT:CdSe QD BHJ film.
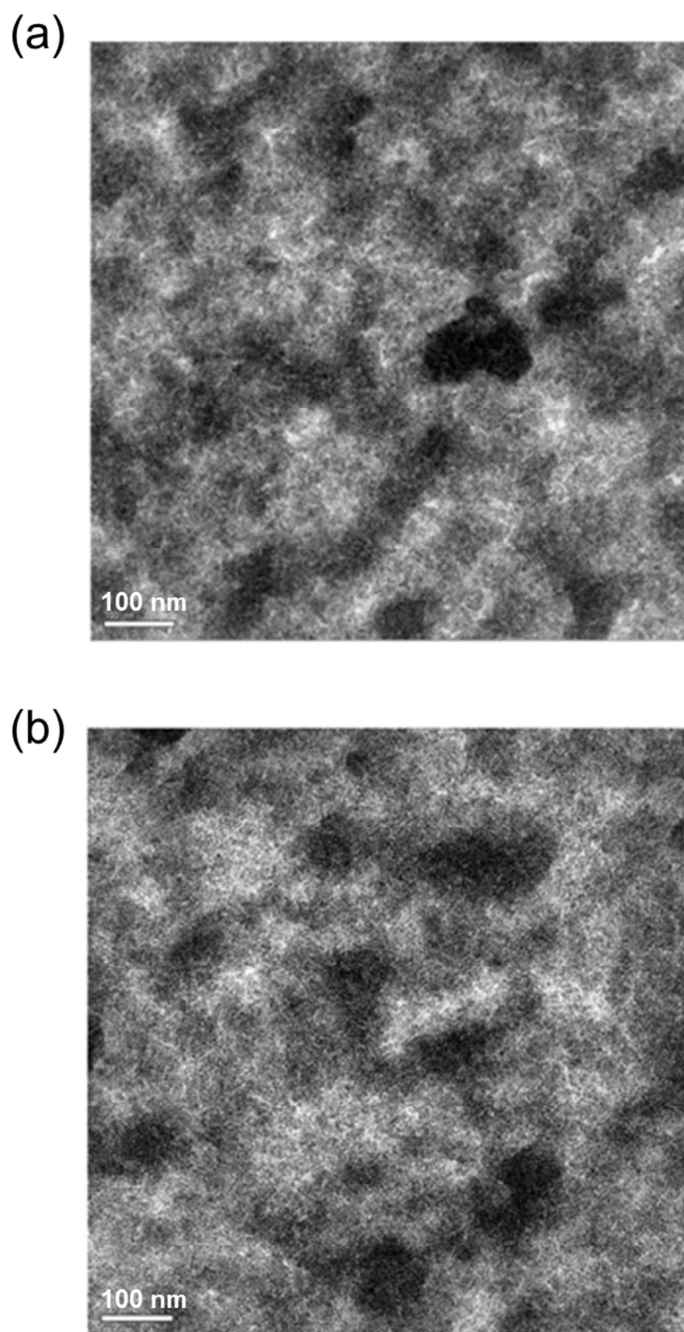
Figure 3.25 TEM images of (a) as-cast and (b) 150°C annealed P3HT:CdSe QD BHJ film.

3.4.2 P3HT:CdSe QD BHJ Solar Cell Performance with Thermal Annealing

The effect of thermal annealing on P3HT:CdSe QD hybrid solar cells were investigated. The red shift of CdSe QD absorption spectra after annealing revels that thermal annealing increase electrical coupling of QDs, and almost perfect quenching of P3HT PL after annealing denotes improved exciton dissociation efficiency. Therefore, annealing of hybrid solar cells could improve J_{SC}.

Using the diode equivalent circuit models, we can extract the diode parameters from the J-V curves (see, Table 3.6). From the equivalent circuit model, n, J_0, R_S are reudced and R_{Sh} is remained unchanged after thermal annealing. Increase in R_S denotes enhanced carrier transport due to the enhanced electronic coupling and unchanged R_{Sh} and reduced J_0 denote that leakage path does not generated since the morphology of P3HT:CdSe QDs BHJ film does not change noticeably.

Decrease in V_{OC} interpreted with the decrease in diode ideality constant (n) after thermal annealing since V_{OC} is proportional to n.

$$V_{OC} \approx \frac{nk_BT}{q}\ln\left(\frac{J_{ph}}{J_0}+1\right) \qquad (3.7)$$

Although V_{OC} decreased after thermal annealing, thanks to the enhanced J_{SC}, PCE is improved after annealing.

The IPCE increased after annealing over all wavelengths. This denotes improved carrier transport by thermal annealing resulted enhanced collection of photo carriers since carrier transport is independent from incident photon wavelength.
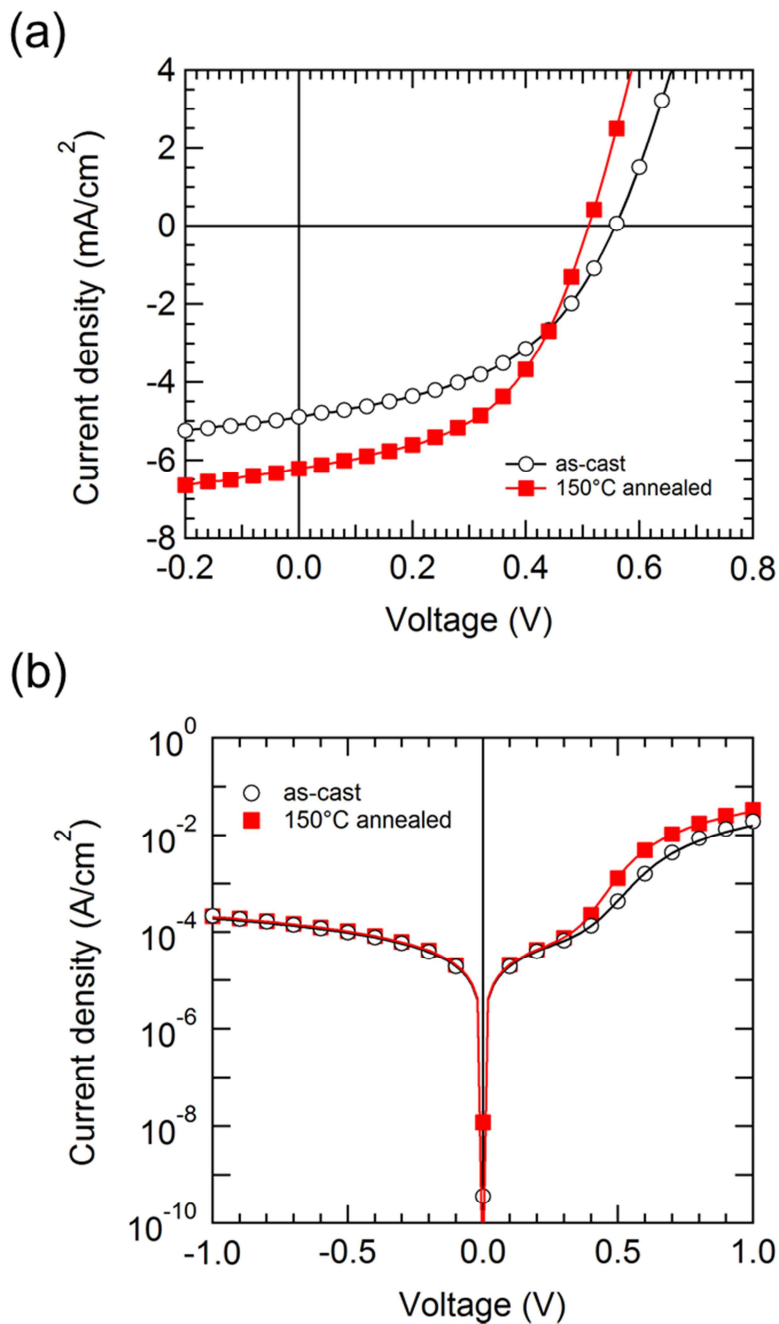
Figure 3.26 Current density-voltage *(J-V)* characteristics of as-cast and 150°C annealed P3HT:CdSe QD BHJ solar cells: (a) under the AM 1.5G 1 sun illumination and (b) dark condition.

Table 3.6 Characteristics of as-cast and 150°C annealed P3HT:CdSe QD BHJ solar cells (The average values of J_{SC}, V_{OC}, FF, PCE are derived from four individual cells on the same substrate. n, J_0, R_S, R_{Sh} are evaluated from J-V curve in **Figure 3.26**(b)).

	as-cast	150°C annealed
J_{SC} (mA/cm^2)	4.58	6.05
V_{OC} (V)	0.56	0.50
FF (%)	46.1	47.9
PCE (%)	1.19	1.46
n	2.03	1.66
J_0 (nA/cm^2)	24.4	13.0
R_S (Ω)	97.6	61.2
R_{Sh} (Ω)	26150	24450
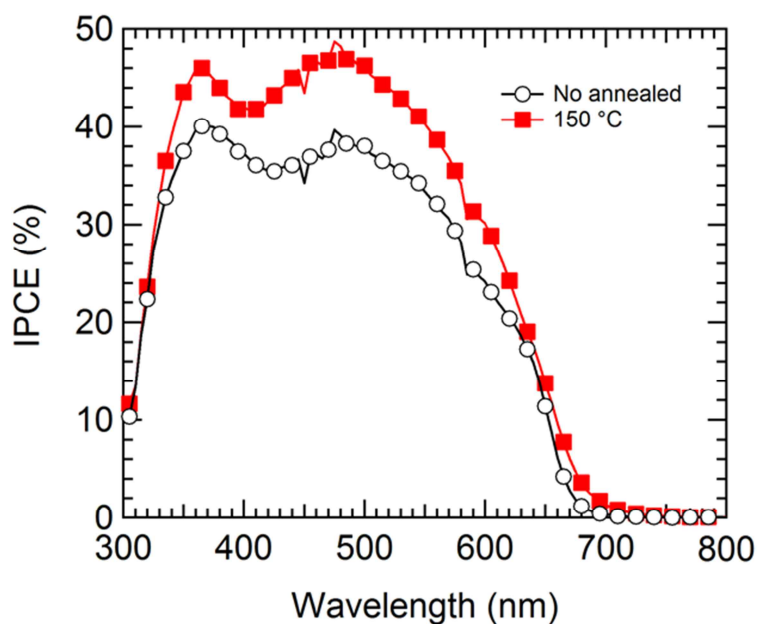
Figure 3.27 IPCE spectra of as-cast and 150°C annealed P3HT:CdSe QD BHJ solar cells

To further investigate recombination and carrier collection properties, we measured *J-V* curves under various illumination light. P3HT:CdSe QD BHJ solar cell before thermal annealing exhibited short collection voltage (V_C) compared to after annealing. . In the case of the solar cell after thermal annealing, linear fits under 10 mW/cm^2 doesn't intersect at a single point because the *J-V* curve is dominated by shunt resistance. The collection efficiency at short circuit condition (η_{C0}), and $\mu\tau_{eff}$ can be evaluated from the V_C with the V_{bi} of 0.7 V. the η_{C0} is slightly improved after thermal annealing from 77 to 79%, and $\mu\tau_{eff}$ enhanced slightly from 2.52 to 2.70 × 10^{-10} cm^2/V.

The light intensity scaling exponent (α) which correlates with a carrier loss mechanism, i.e. $J_{SC} \propto I_{light}^{\alpha}$, exhibited small decrease after thermal annealing. This denote slight arise of bimolecular recombination after annealing due to the increased charge generation.
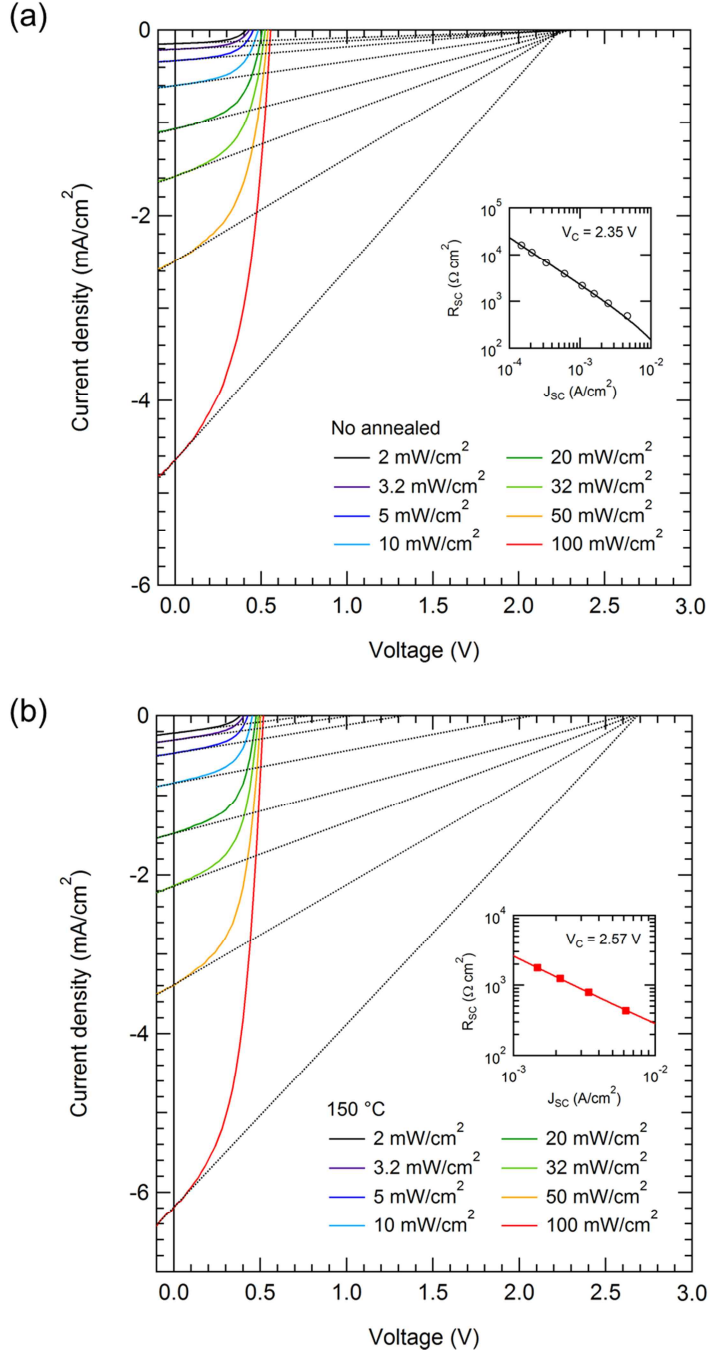
Figure 3.28 Collection voltages (V_C) of (a) as-cast and (b) 150°C annealed P3HT:CdSe QD BHJ solar cells. Inset: extracted R_{SC} at around V = 0 and calculated V_C.
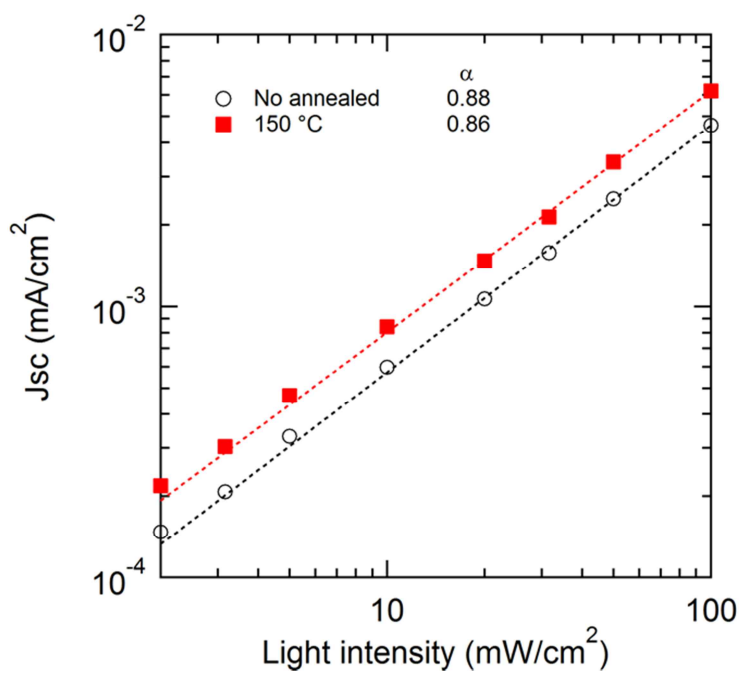
Figure 3.29 Light intensity dependence of short circuit current density (J_{SC}) of as-cast and 150°C annealed P3HT:CdSe QD BHJ solar cells. Dotted lines denote fitted curves using $J_{SC} \propto I_{light}^{\alpha}$.

3.5   Summary

Ligand exchange/elimination procedure of colloidal CdSe QDs for optoelectronic device application were investigated. P3HT:CdSe QDs had optimal device performances at 1:3 wt. ratio and at around 100 nm thickness. Thermal annealing of the hybrid active layer enhanced electron coupling of CdSe QDs and resulted improved J_{SC}. Surface ligands properties on CdSe QDs, such as overall proton ratio and areal ligand density, were quantitatively analyzed through ^{1}H-NMR measurement. Because of the binding mode of oleate ligands on CdSe QDs, proton-donating HA effectively replaced the olate ligands, while HAm eliminated oleate ligands ineffectively. However, in the case of sequential treatment with HA followed by HAm, HAm eliminates hexanoate ligands effectively, which is attributed to reduced steric hindrance of the ligand shells. The decrease in the average ligand shells thickness directly improved the carrier transport properties of P3HT:CdSe QD BHJ solar cells. Large proportion of oleate ligand in the ligand shells ($R_{O/T} > 8$) distinctively hampered the transport of charged carrier between QDs. However, the QDs with the thin ligand shells ($R_{O/T} < 6.5$) showed the considerable improvement in R_S, J_{SC}, and *PCE*. Moreover the presence of remnant 1-hexylamine ligands   enhanced the overall device performance ($J_{SC} = 6.20$ mA/cm^2, $V_{OC} = 0.61$ V, *FF* = 52.2%, *PCE* = 1.98%) and carrier collection efficiency (η_{C0}) higher than 1-hexylamine-free ones. In addition, recombination mechanism is dominated by monomolecular recombination due to enhanced carrier collection length (l_{C0}). These improvements are originated from the passivation effect of primary amines on the surface states of QDs.

Chapter 4

Modular Fabrication of Hybrid Heterojunction Solar Cells Based on CdSe Tetrapod Nanocrystal Network

Since the pioneering work of hybrid solar cell has first been introduced by Alivisatos and coworkers [15], multilateral approaches to improve the solar cell efficiency have been investigated: i) modifying nanocrystal structures (e.g., spherical dots [21, 28, 35, 39, 65], rods [16, 19, 66], tetrapods [18, 36, 67-69], and hyper-branched nanocrystals [32]), ii) proposing new device architectures [70], and iii) developing new nanocrystal surface passivation processes [19, 24, 39]. More recently, employing low bandgap conducting polymers [18, 36, 71] or organic nanowires in the hybrid structure [28] resulted in significant enhancement in *PCE*.

Among various nanocrystals available, tetrapod (TP) semiconductor nanocrystals are a promising structure to improve the performance of hybrid solar cells. This is because the four branches of a tetrapod that are 3-dimensionally extended increase the absorption cross section [72] and also provide conductive pathway to enhance overall charge transport through TP ensembles [31]. Also, by forming hybridized structures with conducting polymers, the increased interfacial area between TPs and conducting polymers is expected to facilitate the exciton dissociation. More importantly, the porous network formed by TPs, which resembles tetrapod-breakwaters, results in an ideal structure to form a bulk heterojunction with the hybridizing organic counterpart.

To fully utilize the benefits offered by the TPs for solar cell applications, the proper elimination of bulky ligands attached to TP surface is essential, which are originally employed to prevent TP aggregation during synthesis, storage, and processing. This is because the bulky and insulating natures of typical surface ligands prevent efficient interfacial contact between TPs and conducting polymers within the hybrid structure. However, the steps for ligand removal or exchange have unfortunately hampered the advances in the TP/polymer hybrid solar cell research. Namely, the poor colloidal stability prevents reliable and reproducible formation of TP/polymer hybrid active layers in terms of nanoscopic morphology, particularly if the ligand removal/exchange processes are inserted prior to forming binary dispersions of the two materials. On the other hand, if the ligand removal/exchange steps are introduced after the formation of TP/conducting polymer hybrid films, independent control on the nanoscopic morphology and the surface chemistry of TPs is not possible, which are the two critical factors determining the final solar cell performance. This is because the TP surface modification in such a manner would inevitably influence the inter-particle distance or spatial distribution of TPs within

the final hybrid structure. Consequently, systematic analysis on TP/polymer hybrid solar cell operations could not be carried out, and thereby rational guidelines for improving the TP/polymer hybrid solar cell performance were not provided.

In this chapter, we propose a so-called modular fabrication to assemble TP nanocrystal/polymer hybrid bulkheterojunction solar cells to prevent morphology change followed by surface ligand modification and resolve reliability problem. Unlike prior approaches based on the binary dispersion of nanocrystals and polymers with pre- or post-chemical treatments of the nanocrystals, our modular fabrication separates the breakwaters-like nanocrystal network formation (step 1), the nanocrystal surface modification via chemical treatments (step 2), and the intrusion of polymers into the nanocrystal network (step 3). Accordingly, CdSe TP/P3HT hybrid bulkheterojuctions could be assembled with their nanoscopic morphology and surface chemistry under control. Consequently, the influence of nanocrystal surface modification on the as-assembled solar cell performance could be systematically examined through temperature-dependent current density (J) vs. voltage (V) measurements at varying light intensities.

4.1 Modular Fabrication of CdSe Tetrapod/P3HT Heterojunction

4.1.1 Preparation of CdSe Tetrapod for Building Block of Network Structured Films

Well-defined CdSe TPs with high morphological uniformity were synthesized following the continuous precursor injection (CPI) method [49]. Careful control on both injection rate of precursors and reaction temperature yielded oleate-capped, lengthy CdSe TPs with excellent shape-selectivity (over 90%). The arm-length of these TPs was ~76 ± 3 nm (see Figure 4.1). Such well-defined CdSe TPs with uniform lengthy arms are particularly beneficial for achieving highly conductive TP networks. Moreover, the resulting breakwaters-like TP networks ensure formation of heterojunction with polymer counterpart exhibiting a significant increase in interfacial contact area with conducting polymers. The arm-diameter of these CdSe TPs was ~8 nm. Such an arm thickness was necessary to improve the mechanical robustness of the network structure and to maximize the light absorption window.

Although stable nanocrystal dispersions, necessary for further solution processing, are achievable with as-synthesized TPs with oleate ligands attached to the nanocrystal surfaces, the original ligands were replaced with oleylamines. Oleylamine ligands, which also yield stable nanocrystal dispersions, have moderate affinity to the surface Cd atoms of CdSe TPs and thereby the removal of oleylamine ligands could be done simply by rinsing the nanocrystals with alcohols later in the fabrication steps [73]. To replace the oleate ligands with oleylamine ligands, a two-

phase ligand exchange method was adopted using tetrafluoroboric acid (HBF_4) (Figure 4.2(a)). Vortexing a mixture of CdSe TPs (in hexane) and HBF_4 (in N,N-dimethylformamide (DMF)/water) resulted in the phase transfer of CdSe TPs from the hexane phase to the mixed DMF/water phase. The phase transfer occurred because the surface Cd sites become positively charged and surrounded by BF_4^- counter ions, as HBF_4 donates protons to the oleate ligands that are detached from the Cd surface as oleic acids [74]. The removal of oleate ligands upon repetitive HBF_4 treatments was confirmed from the disappearance of the vibrational peaks originating from alkylchains (2800–3000 cm^{-1}) in the FT-IR spectra (Figure 4.2(b)). Even if the repulsive interactions among charged TPs may not yield completely stable dispersions of CdSe TPs, the electrostatic repulsion was sufficient enough to prevent irreversible nanocrystal aggregation. The charged CdSe TPs were then quickly collected by centrifugation and re-dispersed in chloroform containing oleylamines. As the oleylamines form coordination bonds with CdSe TP surfaces, TPs could be well dispersed in organic solvents like chloroform. Also, the vibrational peaks due to alkylchains re-appeared in the FT-IR spectra as the evidence of TPs capped with oleylamines. We also note that the optical spectra of CdSe TPs were unchanged upon the ligand exchange from oleates to oleylamines (Figure 4.2(c)).
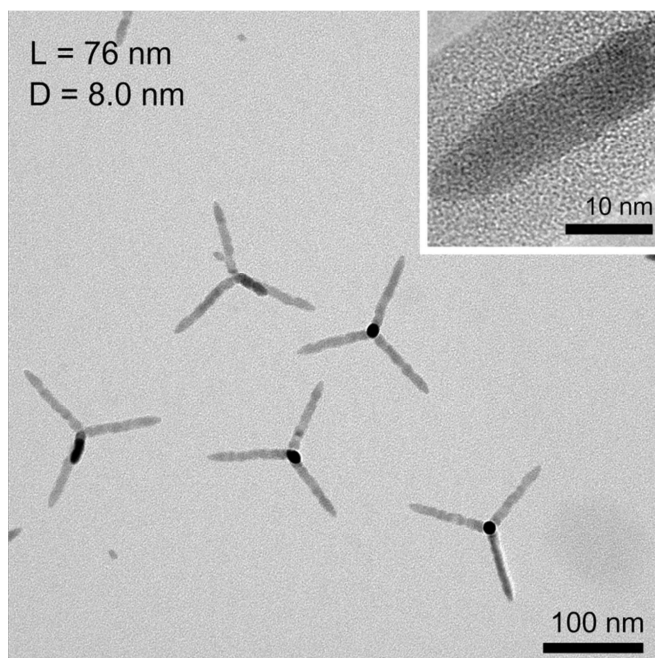
Figure 4.1 TEM images of CdSe tetrapods with 76 nm of arm length. Inset is provided to show arm diameter.
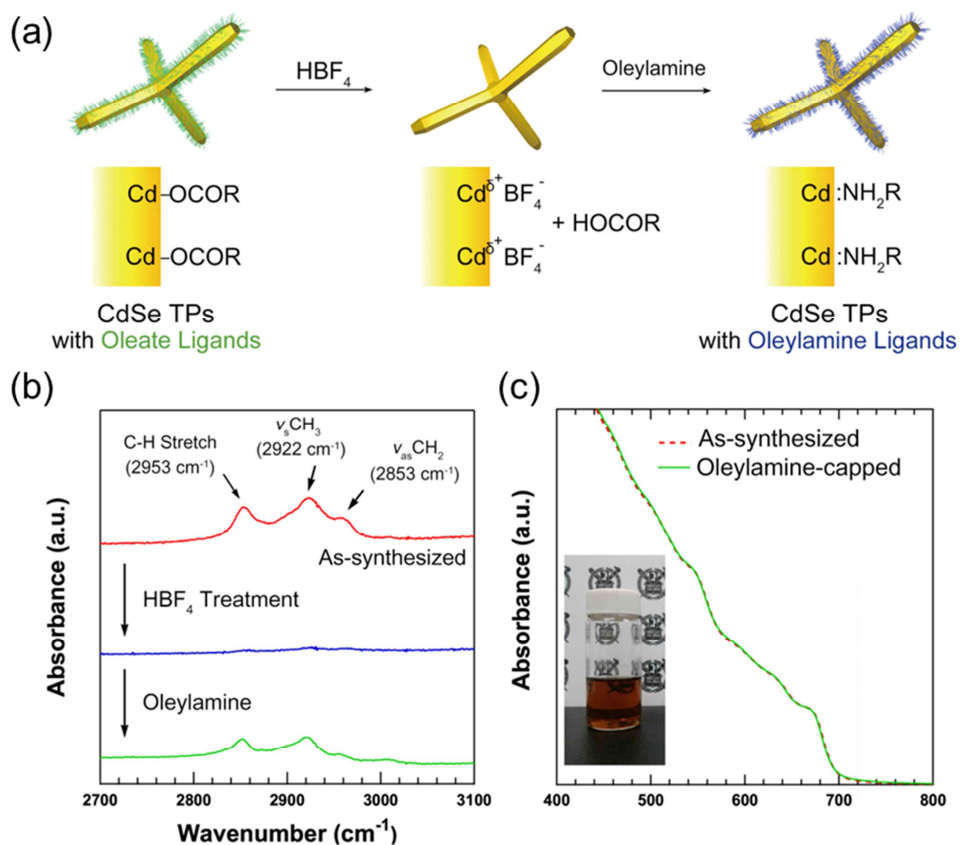
Figure 4.2 (a) A schematic on the ligand exchange procedure of CdSe TPs from oleates to oleylamines. (b) FT-IR spectra of as-synthesized CdSe TPs with oleate ligands (red), TPs after treatment with HBF_4 (blue), and TPs after capping with oleylamine ligands (green). (c) Absorption spectra of as-synthesized CdSe TPs (red dashed line) and oleylamine-capped CdSe TPs (green solid line). The inset is a photograph of oleylamine-capped CdSe TPs dispersed in chloroform.

4.1.2 Modular Fabrication of CdSe TP/P3HT Hetrojunction Solar Cells

The modular fabrication to fabricate CdSe TP/P3HT hybrid solar cells is schematically illustrated in Figure 4.3.

Figure 4.3 Schematic illustration of the modular fabrication for CdSe TP/P3HT heterojunction solar cells.

In Step 1, an interconnected CdSe TP network (~200 nm thick) was first formed by spin-coating a dispersion of oleylamine-capped CdSe TPs in chloroform onto a transparent cathode. The oleylamine ligands were then removed by thermal annealing and repeated ethanol washing. The removal of alkylchains after the repeated ethanol washing for more than 90% was confirmed from FT-IR spectra (Figure 4.5(a)). In addition, the absorption spectra (Figure 4.6(a)) and the highly porous morphology (Figure 4.4(a)) of the CdSe TP network were hardly changed after the ligand removal, confirming the robustness of TP network structure. We also note that the resulting CdSe TP network was devoid of micro cracks, which have often been observed from closely packed nanocrystal films due to large volume contraction during the ligand exchange process [75]. The voids created during the CdSe TP network formation are thought to mitigate the significant volume contraction upon ligand removal.
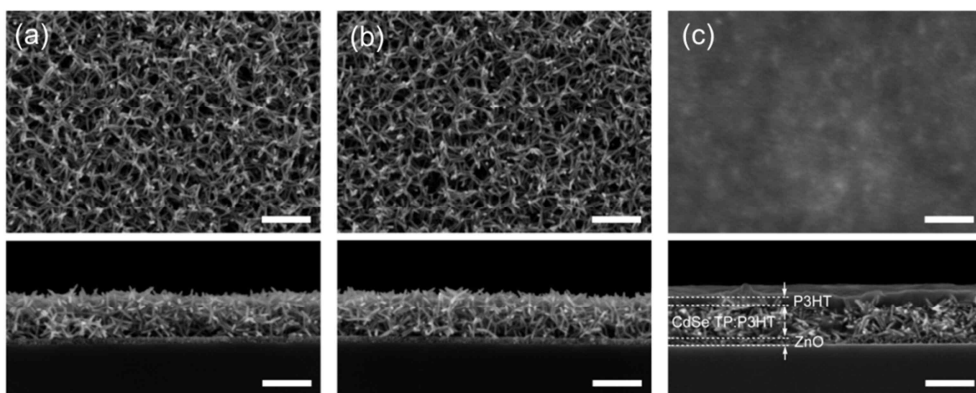
Figure 4.4 Plan- (top) and cross-sectional (bottom) SEM images of (a) a bare CdSe TP network film (Step 1), (b) a CdSe TP network film treated with 1-hexylamine (Step 2), and (c) a CdSe TP/P3HT hybrid film (Step 3). All the scale bars in the SEM images are 200 nm.

In Step 2, the surfaces of bare TPs were further modified by spin coating short ligands such as 1-hexylamine and pyridine directly onto the TP network prepared from Step 1 (Figure 4.5(b)). The choice of 1-hexylamine and pyridine is an interesting set of surface ligands, because these amines are known to cause an opposite effect on the nanocrystal surface state, even if both ligands contain the same nitrogen atoms that interact with nanocrystal surfaces through σ-electron donation. While 1-hexylamine could effectively reduce the surface states [76], pyridine ligands are thought to form traps by delocalizing holes within the aromatic rings [77]. After the TP surface modification, negligible change in the nanoscopic morphology was observed (Figure 4.4(b)). We also note that the surface modification did not cause significant change in the absorption spectra (Figure 4.6).
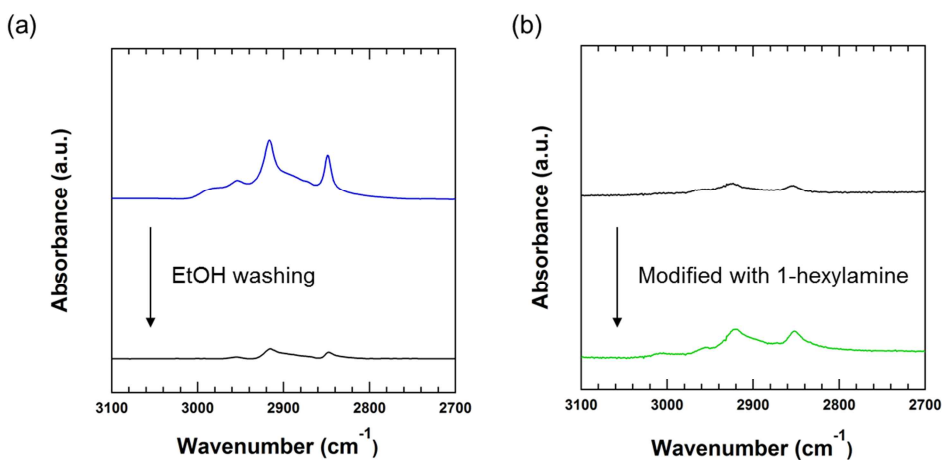
Figure 4.5 Changes in the FT-IR spectra of CdSe TP network films (a) after ethanol washing (Step 1) and (b) after the surface modification with 1-hexylamine (Step 2).
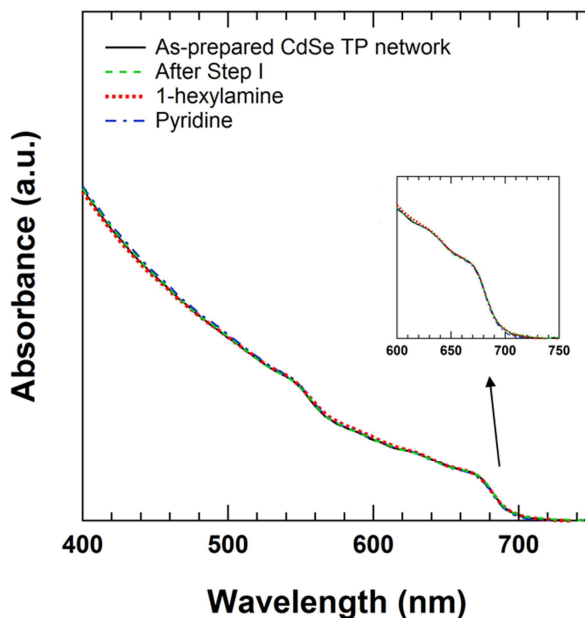
Figure 4.6 Absorption spectra of CdSe TP network film: as-prepared (black solid line), after Step 1 (green dashed line), and after step 2 (red dotted line for 1-hexylamine and blue dash-dot line for pyridine). Inset represents an absorption edge of all CdSe TP network films.

As the final step, voids left within the CdSe TP network were filled with conducting polymers by spin-coating a P3HT solution onto the surface-treated TP network. This final process guaranteed to create the bicontinuous TP/polymer hybrid structure which is critical to serve as a solar cell active layer. The planar and cross-sectional scanning electron microscope (SEM) images shown in Figure 4.4(c) clearly demonstrate that the TP network is fully covered with the conducting polymers. Atomic depth profiles of the TP/P3HT hybrid film obtained from Auger electron spectroscopy, shown in Figure 4.7, also proves the complete infusion of P3HT within the TP network. From the top portion of the hybrid film during the

measurement of Auger electrons, we noted a dominant signal from sulfur over that from cadmium. As the probing position penetrates into the hybrid film yielding intense Cd signal, the signal from sulfur was retained, implying the abundance of P3HT within the CdSe TP network. In addition, the mechanical robustness of the CdSe TP network was again confirmed by removing the P3HT domains from the CdSe TP/P3HT hybrid layer using chloroform: the recovered CdSe TP network showed the absorption spectra and film morphology analogous to the original TP network (Figure 4.8 and Figure 4.9).
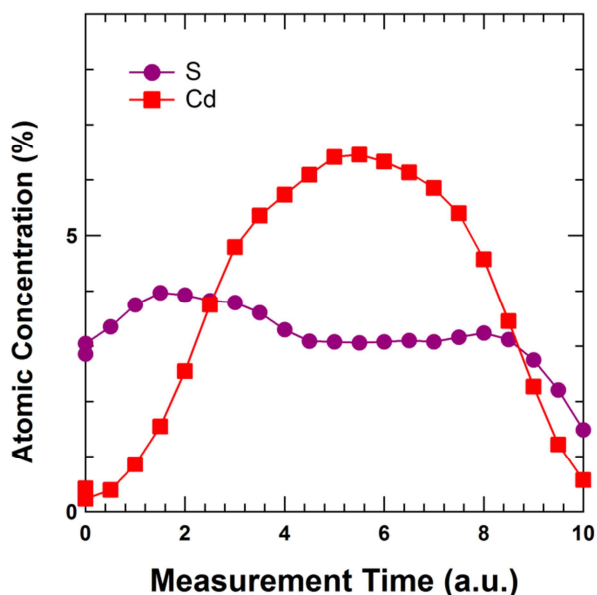
Figure 4.7 Depth profiles of sulfur and cadmium signals in a CdSe TP/P3HT hybrid film (Step 3) taken by Auger electron spectroscopy.
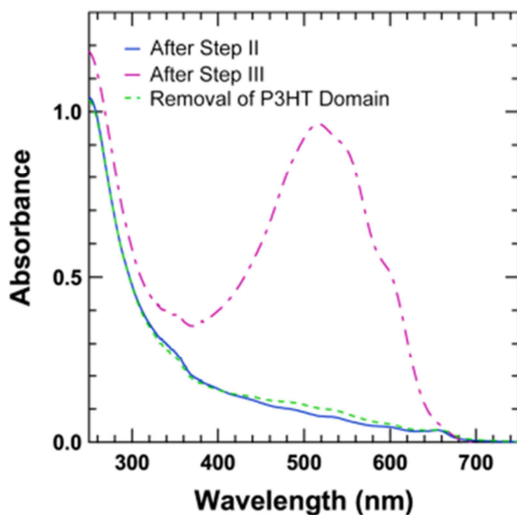
Figure 4.8 Absorption spectra of CdSe TP network film after step 2 (modified with 1-hexylamine), after step 3 (purple dash-dot line), and CdSe TP network film recovered from the prior step by chloroform washing (blue solid line).
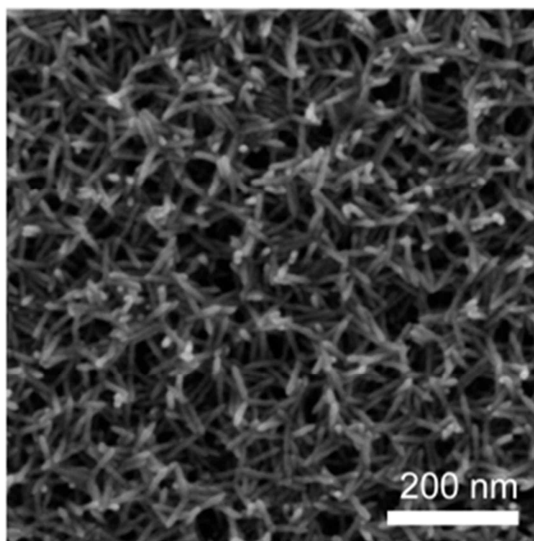
Figure 4.9 A top SEM image of CdSe TP network film yielded from CdSe TP:P3HT hybrid film (Step 3) by chloroform washing.

For the fabrication of actual solar cells, the hybrid TP/P3HT active layers were assembled in the inverted solar cell configuration utilizing indium tin oxide (ITO) substrates as cathodes to extract electrons and Al electrodes to collect holes. The inverted device structure was employed because our modular-approach first requires the formation of a CdSe TP network layer, which is n-type, onto an ITO substrate. Also, for the effective charge collection along with reduced exciton quenching, a hole blocking layer (~20 nm thick ZnO nanoparticle layer) and an electron blocking layer (~10 nm thick MoO_3 layer) were placed between the active layer and two respective electrodes (Figure 4.3). We noticed that the deposition of the ZnO nanoparticle layer facilitated the stable anchoring of the TP network onto the substrate, perhaps due to the enhanced atomic fusion between ZnO nanoparticles and TPs. The entire solar cell fabrication was carried under inert argon atmosphere to prevent undesired oxidation or degradation.

4.2 CdSe TP/P3HT Heterojunction Solar Cell Performance

4.2.1 Performance of Heterojunction Solar Cells with Various Surface Ligand

Figure 4.10 displays the *J-V* characteristics obtained under vacuum for the CdSe TP/P3HT hybrid solar cells that were treated with pyridine and 1-hexylamine. Also, the *J-V* curve of a hybrid solar cell fabricated with a bare TP network is included in the figure as a reference. From the hybrid solar cell device containing TP networks treated with 1-hexylamine, more than 2-fold increase in the short circuit current (J_{SC}) was obtained along with the small reduction in both open circuit voltage (V_{OC}) and fill factor (*FF*), when compared with the reference device. The average solar cell performance is summarized in Table 4.1. The best device, with TP networks treated with 1-hexylamine, yieded the power conversion efficiency (PCE) of 2.24 %, J_{SC} of 7.56 mA cm^{-2}, V_{OC} of 0.63 V and *FF* of 47.1 % that is comparable with the best CdSe NC/P3HT hybrid solar cells treated with short alkylamines reported so far [21, 70]. Meanwhile, the J_{SC} of the solar cells with TP networks treated with pyridine was slightly increased along with the small reductions in both V_{OC} and *FF* when compared with the reference device. The reductions of V_{OC} and *FF* will be discussed in detail later.
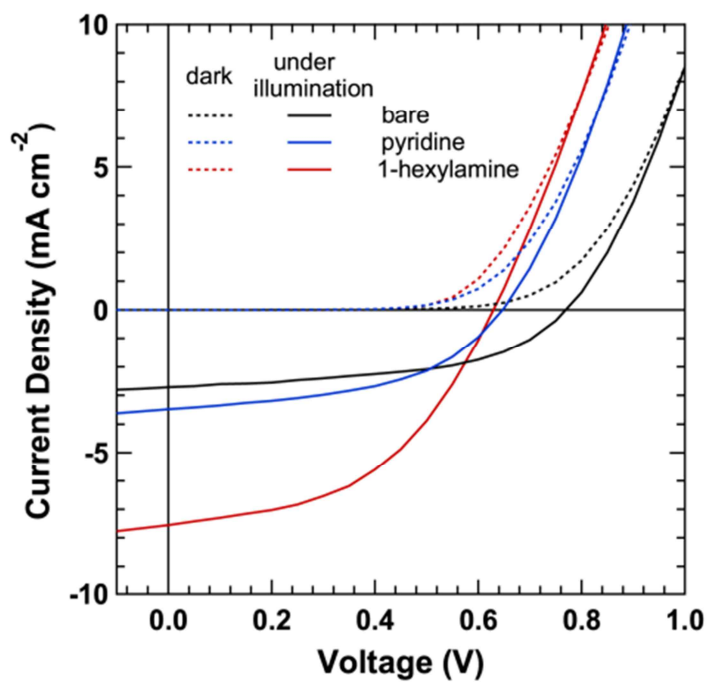
Figure 4.10 *J-V* characteristics of CdSe TP/P3HT hybrid solar cells under AM 1.5G 1sun illumination: TP surface treated with 1-hexylamine (red) and with pyridine (blue) and bare TP surface (black).

Table 4.1 Summary of valence band maximum (VBM), conduction band minimum (CBM), short-circuit current (J_{SC}), open-circuit voltage (V_{OC}), fill-factor (*FF*), and power conversion efficiency (*PCE*) of the hybrid solar cells. Statistics for the solar cell characteristics are based on a total of 12 devices for bare and pyridine and 38 devices for 1-hexylamine.

	Bare	Pyridine	1-hexylamine
VBM (eV)	5.5	5.6	5.7
CBM (eV)	3.7	3.8	3.9
J_{SC} (mA/cm^2)	2.84 ± 0.35	3.51 ± 0.29	6.42 ± 0.68
V_{OC} (V)	0.78 ± 0.04	0.67 ± 0.05	0.62 ± 0.06
FF (%)	49.1 ± 3.1	47.4 ± 2.8	45.4 ± 4.0
PCE (%)	1.09 ± 0.12	1.11 ± 0.13	1.80 ± 0.18
PCE_{best} (%)	1.31	1.39	2.24

The Photoluminescence (PL) decay expriements of P3HT and P3HT/CdSe TP films are related with the exciton dissociation efficiency of P3HT domain, since CdSe TPs has no PL. The PL decay characteristics could be well fitted with single exponential decay function. The solid lines in Figure 4.11 denote fitting lines. In comparison with a neat P3HT film, CdSe TP/P3HT hybrid films showed distinct decrease in PL decay lifetime (from ~930 ps to ~550 ps, probed at 650 nm for PL of P3HT domain). The PL experiments proves that the excitons generated in P3HT domains dissociated by TPs, and the exciton dissociation efficiency is hardly influenced by surface ligands.
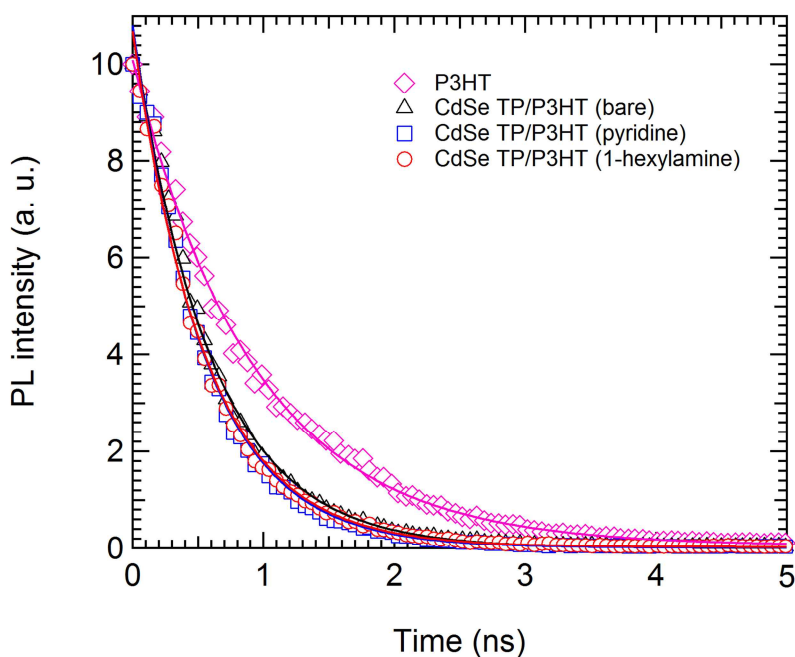
Figure 4.11 PL decay spectra of P3HT and CdSe TP/P3HT films: CdSe TPs without surface modification (black triangle), treated with pyridine (blue square), and treated with 1-hexylamine (red circle)

Figure 4.12(a) displays the incident photon-to-current efficiency (IPCE) of the hybrid solar cells treated differently at varying wavelength. Over the entire wavelength range, the IPCEs were higher for the active layers containing TP networks treated with either 1-hexylamine or pyridine, compared with the IPCE measured with devices containing pristine TP networks. Between these two, the hybrid layers containing TP networks treated with 1-hexylamine ligands exhibit much pronounced enhancement than those treated with pyridine. These results are consistent with the higher J_{SC} values obtained from the devices treated with 1-hexylamine ligands than those with pyridine ligands.

Interestingly, the shape of the IPCE curves exhibited clear discrepancy with the absorption spectra of the active layers, as displayed in Figure 4.12(b). As an IPCE curve reveals the photo-carrier generation efficiency (which is a product of photon absorption efficiency and exciton dissociation efficiency) and the carrier extraction efficiency of solar cells as a function of wavelength, the distinct difference in the shape of the two curves indicates that exciton dissociation and/or carrier extraction limits the performance of CdSe TP/P3HT hybrid solar cells. Since the carrier extraction at the electrodes is independent on the illuminated wavelength, the discrepancy should originate from the ineffective exciton dissociation at the CdSe TP/P3HT interfaces.

The origin of poor exciton dissociation in these hybrid layers can be deduced from the detailed features of the IPCE curves. It is clear that the highest IPCE is achieved at wavelength below 440 nm, which should be mainly attributed to the absorption of CdSe TPs rather than P3HT. Also, small but notable photon-to-current conversion was observed at wavelength above 640 up to 700 nm. This finite current generation should also originate from the absorption of CdSe TPs, as the energy in this wavelength range is smaller than the optical band gap of P3HT. Meanwhile, the

102

IPCE in the range between 440 to 640 nm (wavelengths that are absorbed dominantly by P3HT domains) was not as pronounced as one would expect from the location of the absorbance maximum. Overall, these results imply that excitons generated in the P3HT domains are less efficiently dissociated to free electrons and holes than those populated in the CdSe TP domains.
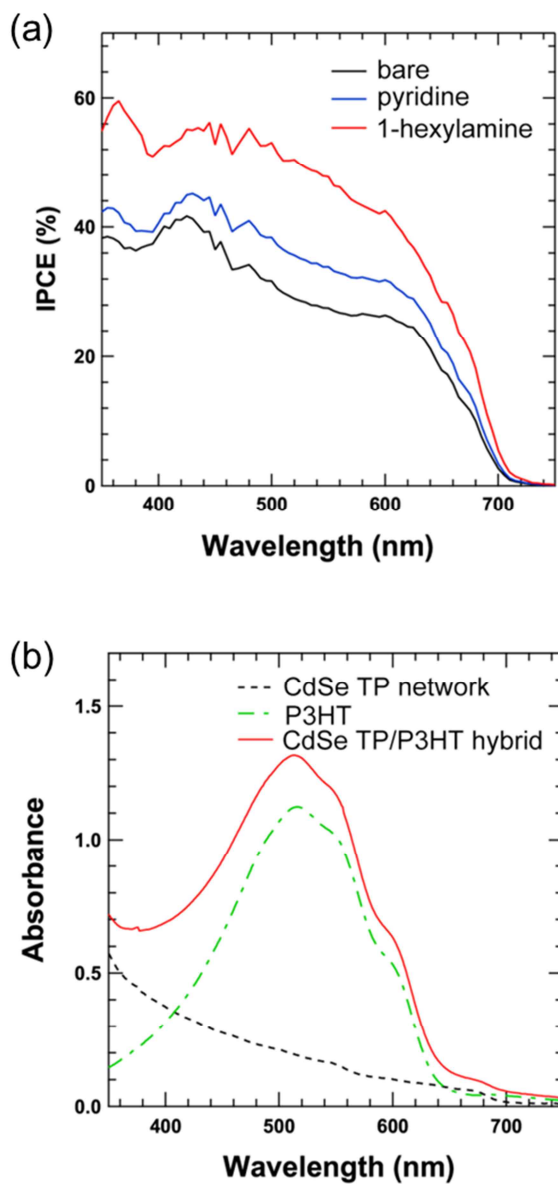
Figure 4.12 (a) Incident photon-to-electron efficiency (IPCE) curves: CdSe TPs without surface modification (black), treated with pyridine (blue), and treated with 1-hexylamine (red). (b) UV-visible absorption spectra of CdSe TP/P3HT active layers treated with 1-hexylamine (solid red), P3HT only (dash-dot green), and CdSe TP network only (dashed black).

4.2.2   UPS Analysis of CdSe TP/P3HT Hybrid Solar Cells

To understand the change in V_{OC} upon surface modifications, UV-photoelectron spectroscopy (UPS) measurements were performed. Figure 4.13 shows the high binding energy cut-off region (Figure 4.13(a)) and the valence band region (Figure 4.13(b)) in the UV-photoelectron spectra for CdSe TP networks treated with two different ligands. A larger shift in the high binding energy cut-off region toward a lower energy value was observed for the CdSe TP network treated with 1-hexylamine compared with the TP network treated with pyridine. Meanwhile, the optical bandgap obtained from absorption measurements remained constant (see the inset of Figure 4.6). Combining these results indicate that the relative positions of the valence band maximum (VBM) and the conduction band minimum (CBM) for the CdSe TP networks are varied upon different chemical treatments. Compared with the bare TP network, the energy levels of TP networks treated with 1-hexylamine and pyridine ligands were lowered by 0.24 and 0.13 eV, respectively (Figure 4.13(c)). Since V_{OC} in heterojunction solar cells is typically determined by the energy difference between the CBM of an acceptor layer and the VBM edge of a donor layer, the results from the UPS measurements could favorably explain the reduced V_{OC} values for solar cell samples treated differently. The shift in the energy levels for the solar cell devices treated differently is attributed to the formation of different interfacial dipoles between the exchanged ligands and nanocrystal surfaces, which either increase or lower the local vacuum level [78].
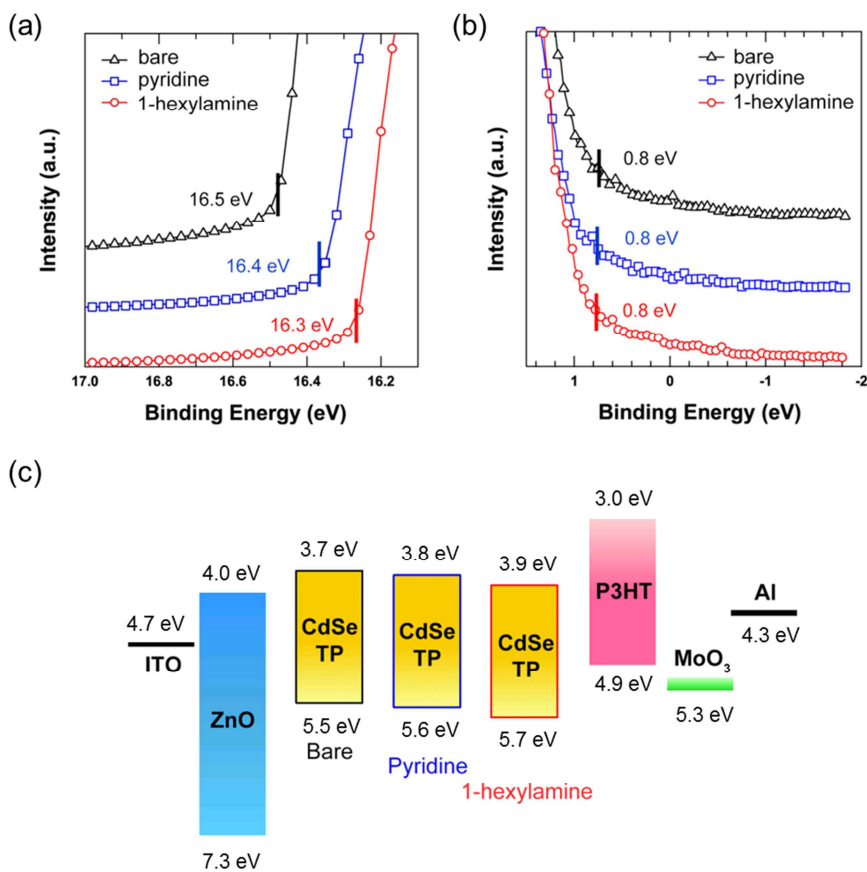
Figure 4.13 (a) High binding energy cut-off region and (b) on-set region in the UPS of CdSe TP network films: bare (black), modified with pyridine (blue), and modified with 1-hexylamine (red). All spectra were referenced with an Au substrate with a work function of 5.1 eV. (c) The energy level diagram of CdSe TP/P3HT hybrid solar cells with different passivation ligands.

4.3 Temperature and Light Intensity Dependence of TP/P3HT Solar Cells

To examine the influence of surface modification of CdSe TPs on hybrid solar cell performance, we carried out temperature (T)-dependent J-V measurements (200~300 K) at different light power (I_{light}, 3~100 mW/cm^2) and analyzed the device characteristics.

4.3.1 Light Intensity Dependence of Solar Cell Performance

Figure 4.12 exhibits incident light intensity (I_{light}) dependence of TP/P3HT hybrid solar cells with different surface ligands. The J_{SC} and V_{OC} exhibit linearly increase with light intensity, but as displayed in Figure 4.14(b), it was found that the FF values of CdSe TP/P3HT hybrid solar cells with increasing I_{light} were differently varied by surface ligands. Overall, 1-hexylamine and pyridine resulted in higher FF values than the one without surface ligands at low I_{light} below ~20 mW/cm^2 but such tendency was reversed at high I_{light} over ~30 mW/cm^2.

FF is closely related to the effectiveness of carrier extraction, achieved by high carrier lifetime and their mobility. Since high carrier density can lower carrier mobility and lifetime by scattering and annihilation of carriers during charge transport and such deteriorating processes bring about reduction in FF. Since the carrier density in the solar cells is proportional to the J_{SC}, the incident light intensity is strongly correlated with the carrier density in active layer. Plotting FF values as a function of J_{SC} displayed more clear dependence of FF on carrier density. In Figure 4.15, the solar cells with 1-hexylamine always showed higher FF values than other solar cells when they have similar J_{SC} but larger J_{SC} caused further decrease in FF.

Summing up, large charge carrier density lowered *FF* even if the trap states were passivated by surface ligands.
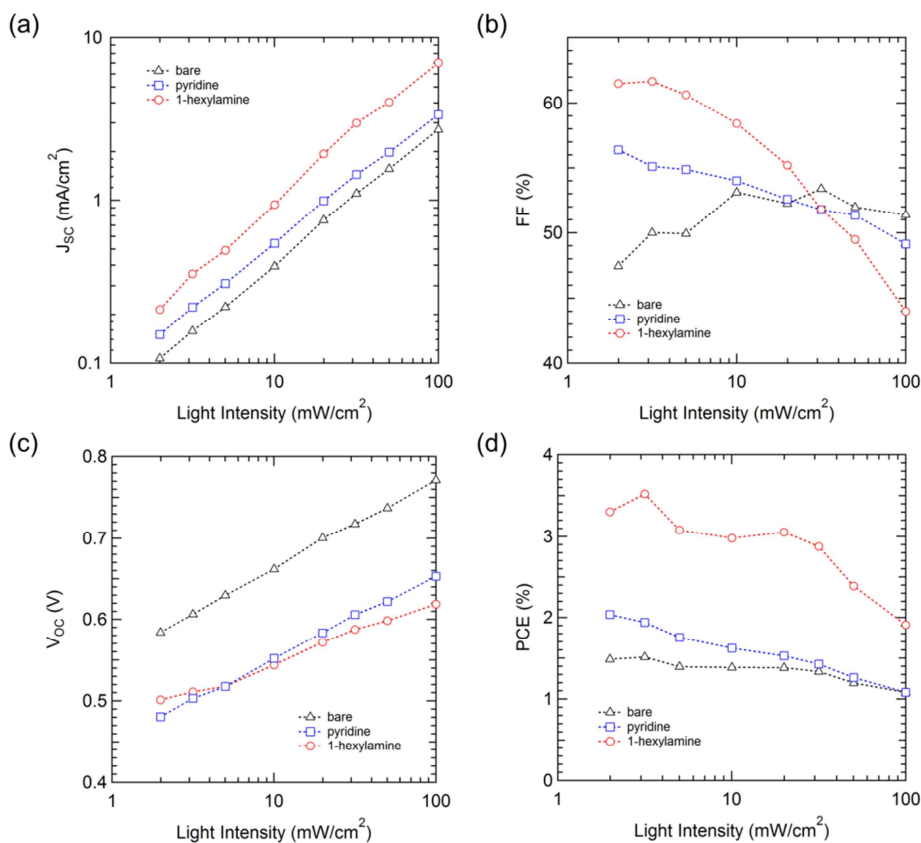
Figure 4.14 Incident light intensity dependence of (a) J_{SC}, (b) *FF*, (c) V_{OC}, and (d) *PCE* of CdSe TP/P3HT hybrid solar cells at room temperature: bare CdSe TP network (black triangle), modified with pyridine (blue square), and 1-hexylamine (red circle).
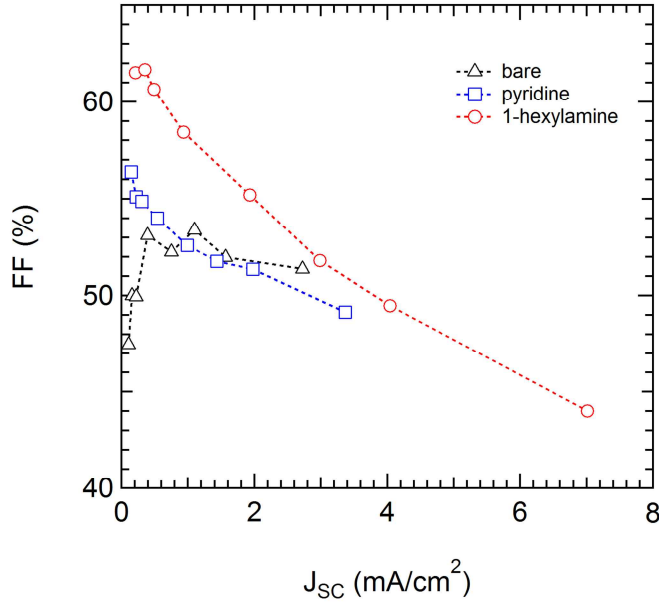
Figure 4.15 Short circuit current density (J_{SC}) dependence of fill factors (*FF*) for CdSe TP/P3HT hybrid solar cells: without surface modification (black triangle), modified with pyridine (blue square), and 1-hexylamine (red circles).

The light power-dependent J_{SC} reveals the nature of recombination process within solar cells ($J_{SC} \sim I_{light}^{\alpha}$, where α is a scaling exponent). The value of unity indicates that the carrier recombination is determined by a monomolecular process, while the α value of 0.5 is associated with a bimolecular process [45, 46]. Deviation in the scaling exponent α from unity toward a smaller value, therefore, implies the presence of energetic traps that capture carriers, serving as recombination centers.

At room temperature, we found that the scaling exponent α was ~ 0.9 for the solar cell containing a TP network treated with 1-hexylamine and ~ 0.8 for the rest of device samples tested (**Error! Reference source not found.**(d)). The variance in

α for the devices with different surface ligands implies that trap states are altered by binding moieties in the surface ligands. As temperature is lowered, the α values are decreased monotonically, while the α value for TP devices containing with 1-hexylamine ligands remain higher than others at given temperatures. These results imply that more frequent carrier trapping takes place at reduced temperatures but the trapping from 1-hexylamine treated TP surface is less frequent than other devices at given temperatures. As the active layer of the CdSe TP/P3HT hybrid solar cells is a disordered system, in which the charge transport should be thermally assisted, more trapping and thereby more recombination of charge carriers are likely to occur at low temperatures. Overall, the enhanced J_{SC} for the hybrid solar cells modified with 1-hexylamine compared to that of the other devices can then be attributed to the reduced bimolecular recombination due to efficient passivation of trap states in TP network by 1-hexylamine ligands.
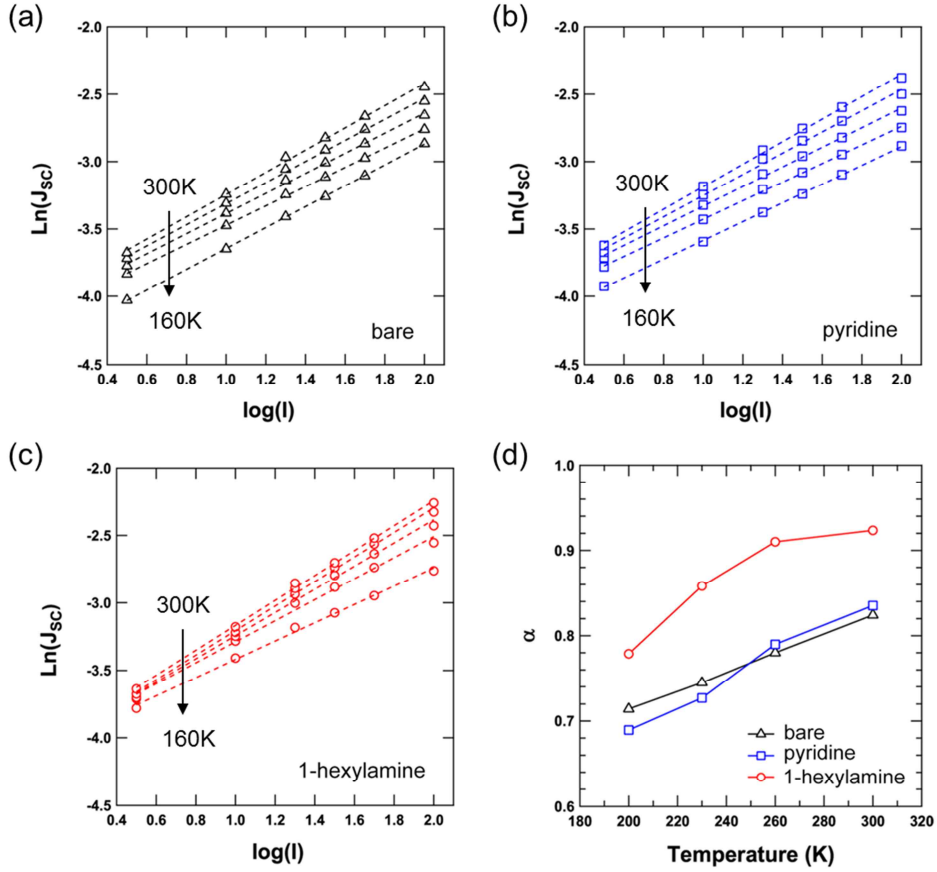
Figure 4.16 Light intensity dependence of short circuit current density (J_{SC}) of CdSe TP/P3HT hybrid solar cells with various temperature: (a) bare CdSe TP networks, TP networks modified with (b) pyridine and (c) 1-hexylamine Dashed lines represent the fitting lines with $J_{SC} \sim I_{light}^{\alpha}$. (d) Temperature dependence of the scaling exponents (α).

4.3.2 Temperature Dependence of Solar Cell Performance

Overall, the hybrid solar cells follow the temperature-dependent behavior similar to typical polymer/fullerene solar cells (Figure 4.17); J_{SC} and *FF* show positive temperature coefficients while V_{OC} displays a negative temperature coefficient [46, 79]. We think that thermally-assisted hopping conduction [80] in organic domains governs the overall photocurrent of present hybrid solar cells. At the same time, the increase in V_{OC} is in good agreement with the analytical equation for V_{OC} based on the Shockley diode equation. Intercepts of the linear extrapolations of V_{OC} values (*T* → 0 K) are very close to E_{CT}/q (E_{CT} is the energy of interfacial charge transfer state and *q* is the elementary charge) [81-83], estimated from the UPS measurements. The V_{OC} at 0 K (1.17, 1.14 and 1.08 V for solar cell with bare TP, pyridine and 1-hexylamine treated TP) denotes that V_{OC} is strongly correlated with the energy level difference of HOMO level of P3HT and conduction band of CdSe TP (1.3, 1.2 and 1.1 eV for bare TP, pyridine and 1-hexylamine treated TP).
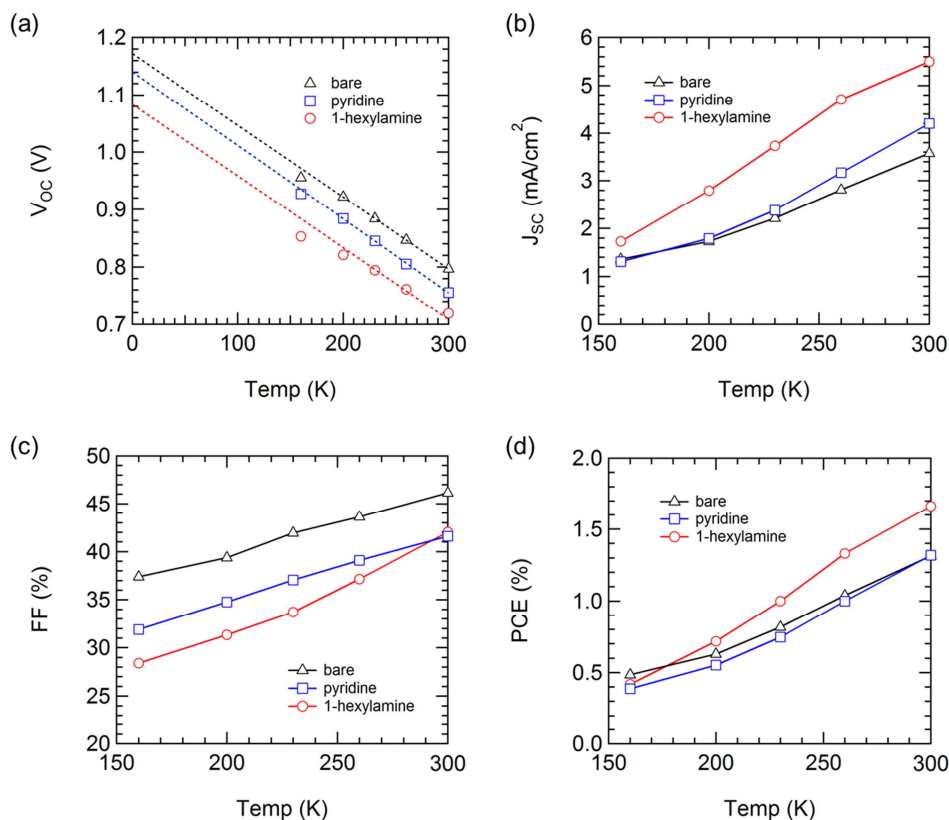
Figure 4.17 Temperature dependence of (a) V_{OC}, (b) J_{SC}, (c) FF, and (d) PCE of CdSe TP/P3HT hybrid solar cells: bare CdSe TP network (black triangle), modified with pyridine (blue square), and 1-hexylamine (red circle).

To analyze the trapping nature of carriers and their influence on J_{SC}, we employed the Arrhenius relation between J_{SC} and T with different I_{light}, $J_{SC}(T, I_{light}) = J_0(I_{light}) \exp(-E_A/k_B T)$, as shown in Figure 4.18. Here, J_0 is a pre-exponential factor determined by photogeneration, recombination, and transport of carriers, E_A is the activation energy, and k_B is the Boltzmann constant [46]. According to the theories typically applied to organic solar cells, E_A is associated with the depth of trap states relative to the transport levels of charge carriers. As summarized in Figure 4.18(d),

we found that the solar cells passivated with 1-hexylamine exhibit lower E_A values compared with other devices. Meanwhile the solar cells treated with pyridine showed similar (at low light intensities) or higher (at high light intensities) E_A values compared with the reference devices.

The lowered E_A and the reduced depth of trap states are perhaps due to the altered energy levels of surface Cd atoms in the presence of 1-hexylamine. Namely, the strong σ-electron donation of 1-hexylamine modulates the non-bonding orbitals of surface Cd atoms that are located near the CBM of CdSe nanocrystals and reduce the depth of trap states [76]. Whereas, the relatively weak σ-electron donation of pyridine (supported by its lower basicity ($pK_b \sim 8.7$) compared with that of primary amines ($pK_b \sim 3.3$)) does not contribute to reducing the trap depth substantially. Instead, pyridine is thought to delocalize holes within the aromatic ring to generate hole traps [77, 84], and increases E_A.

Interestingly, E_A values increase consistently with increased light intensity for all the solar cell devices tested in the present study. If we assume that E_A is solely determined by the depth of trap states, E_A is expected to be independent on I_{light} [46, 85], as often observed in organic or quantum dot photovoltaic research. However, our results do not follow such behaviors. Therefore, an alternative explanation is necessary to describe the TP/polymer hybrid solar cell operation. The origin of the such an intriguing observation is not clear yet. However, unusual light intensity-dependent E_A for our hybrid solar cells may arise from the physical nature of TP nanocrystals with long arms. In other words, the exciton dissociation in our solar cells containing tetrapod arms longer than its Bohr radius would be different from that in typical so-called excitonic solar cells including organic and quantum dot solar cells. Unlike the Frenkel-type excitons in typical excitonic solar cells, which are dissociated only at the interfaces, the excitons in our system would more resemble

the Wannier-type excitons. Further detailed investigation is necessary to clarify the photophysical processes in the hybrid systems involving TPs with various arm dimensions (i.e., length and diameter).
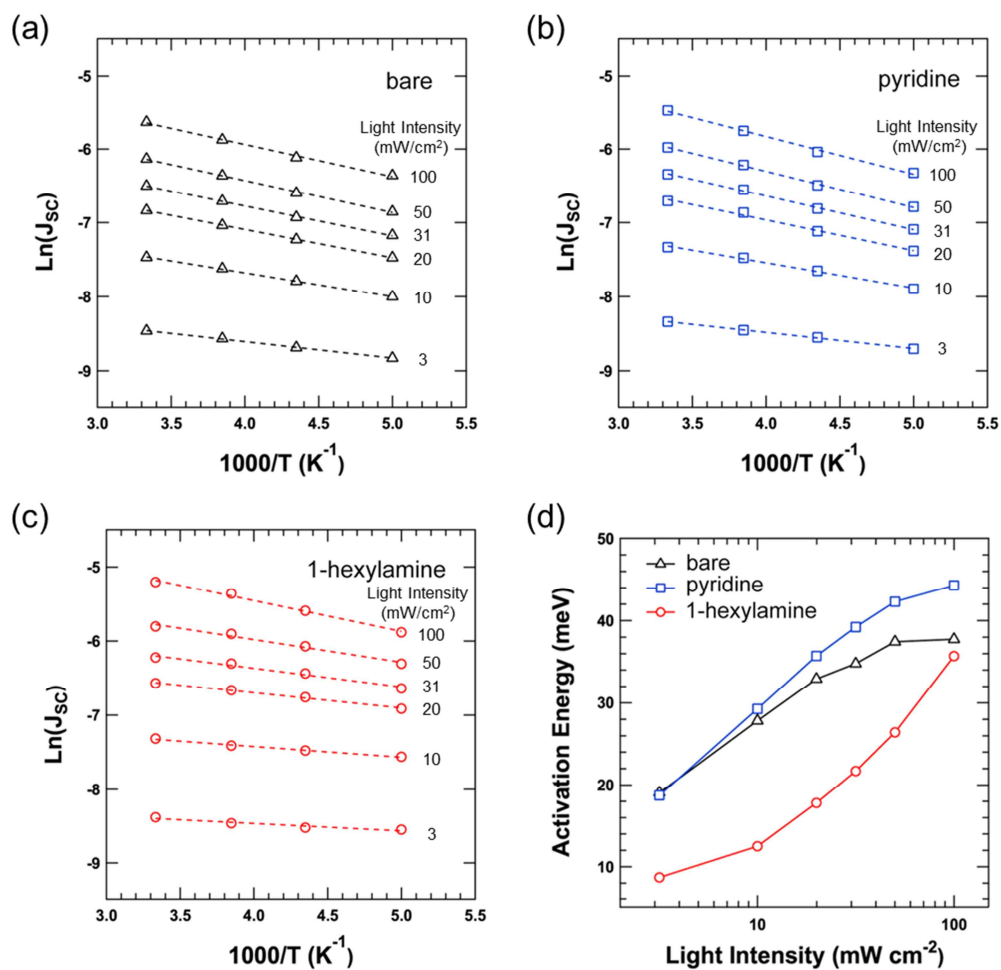
Figure 4.18 Temperature dependence of short circuit current density (J_{SC}) of CdSe TP/P3HT hybrid solar cells under various light intensity: (a) bare CdSe TP networks, (b) TP networks modified with pyridine and (c) 1-hexylamine. Dashed lines represent the fitting lines with Arrhenius relation. (d) Light intensity dependence of activation energy.

4.3.3　Temperature Dependence of Carrier Collection Characteristics

Photogenerated charge carrier collection characteristics could be evaluated from the *J-V* curves under various incident light intensity. Figure 4.19 display the *J-V* curves of the P3HT/CdSe TP solar cells under various incident light and temperature. All linear fit of *J-V* curves of various incident light intensity at short circuit conditions (*V=0*), intersect the x-axis at a single point of voltage, *Vc*. We can evaluate collection length (l_{C0}) and efficiency at short circuit condition (η_{C0}) as well as $\mu\tau_{eff}$ from the V_C (see, Figure 4.20).
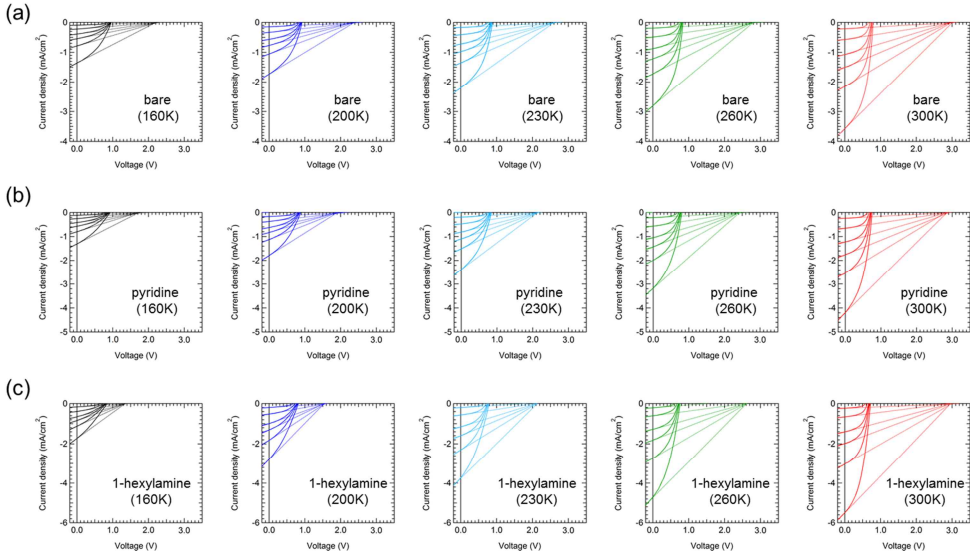
Figure 4.19 *J-V* curves of the P3HT/CdSe TP solar cells with various surface modified CdSe TPs under the various incident light intensity to evaluate collection voltages (V_C): (a) bare, (b) pyridine, and (c) 1-hexylamine.

Collection voltages of P3HT/CdSe TP solar cells with 1-hexylamine surface treated TP exhibits the highest temperature dependence compared with bare, and pyridine treated TPs. This tendency of collection characteristics such as V_C, l_{C0}, η_{C0} and $\mu\tau_{eff}$, have similar tendency of J_{SC} and FF depending on the temperatures. This can be interpreted as the solar cells with 1-hexylamine treated TPs need thermal energy to overcome energy barriers which might be caused by insulting alkyl chains of 1-hexylamine. As a result V_C and J_{SC} exhibits stiff decreasing tendency as the temperature decreased.
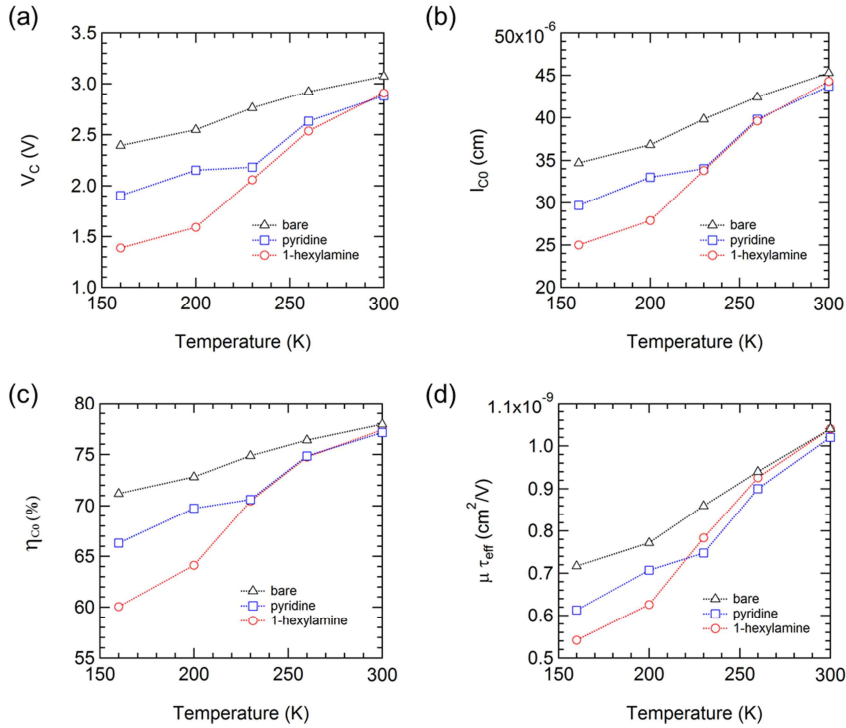
Figure 4.20 (a) Collection voltages (V_C), (b) collection length at short circuit condition, (c) collection efficiency at short circuit condition, and (d) effective $\mu\tau$ product of the P3HT/CdSe TP solar cells with various surface modified CdSe TPs: bare CdSe TP network (black triangle), modified with pyridine (blue square), and 1-hexylamine (red circle).

4.4   Summary

Modular fabrication for CdSe TP/P3HT heterojunction solar cells was demonstrated and the influences of surface passivation of CdSe TPs on solar cell performance were investigated. The modular fabrication enabled us to independently realize inorganic CdSe TP networks devoid of insulating ligands, further modification of nanocrystal surfaces, and finally the filling of semiconducting polymers into the TP networks in a sequential manner. As a result, the modular approach allowed us to establish a reliable and controllable framework to clarify the relationship between surface chemistry of nanocrystals and device characteristics. We confirmed that the passivation of CdSe TPs with 1-hexylamine ligands showed the best short circuit current and power conversion efficiency. The improvements in device characteristics associated with the hybrid solar cell containing TPs treated with 1-hexylamine ligands, when compared with the treatment with pyridine ligands, are attributed to the suppressed bimolecular recombination process within the active layer due to the reduced depth of trap states. We believe that the modular fabrication presented herein is one of versatile platforms to fabricate solution-processible nanocrystal/conducting polymer hybrid solar cells easily applicable to different semiconductor nanocrystals and other novel conducting polymers.

Chapter 5

Conclusion

In this thesis, influence of surface ligand of CdSe QDs and CdSe TP on solar cell performances have been systematically studied. The solar cells were constructed with P3HT as electron donor and CdSe nanocrystals as electron acceptor. Efficiency enhancement could be achieved by the surface modification of NCs, novel device fabrication process and structures.

At first, ligand exchange/elimination procedure based on P3HT:CdSe QDs BHJ solar cell application were investigated. Surface ligands properties on CdSe QDs, such as overall proton ratio and areal ligand density, were quantitatively analyzed through ^{1}H-NMR measurement. Because of the binding mode of oleate ligands on CdSe QDs, proton-donating HA effectively replaced the olate ligands, while HAm eliminated oleate ligands ineffectively. However, in the case of sequential treatment with HA followed by HAm, HAm eliminates hexanoate ligands effectively, which is

attributed to reduced steric hindrance of the ligand shells. The decrease in the average ligand shells thickness directly improved the carrier transport properties of P3HT:CdSe QD BHJ solar cells. Large proportion of oleate ligand in the ligand shells ($R_{O/T} > 8$) distinctively hampered the transport of charged carrier between QDs. However, the QDs with the thin ligand shells ($R_{O/T} < 6.5$) showed the considerable improvement in R_S, J_{SC}, and PCE. Moreover the presence of remnant 1-hexylamine ligands enhanced the overall device performance ($J_{SC} = 6.20$ mA/cm^2, $V_{OC} = 0.61$ V, $FF = 52.2\%$, $PCE = 1.98\%$) and carrier collection efficiency (η_{C0}) higher than 1-hexylamine-free ones. In addition, recombination mechanism is dominated by monomolecular recombination due to enhanced carrier collection length (l_{C0}). These improvements are originated from the passivation effect of primary amines on the surface states of QDs.

We also developed modular fabrication for CdSe TP/P3HT heterojunction solar cells. The modular fabrication method provide robust and simple surface exchange process without morphology change, and therefore, the influences of surface passivation of CdSe TPs (with pyridine and 1-hexylamine) on solar cell performance could be investigated. We confirmed that the passivation of CdSe TPs with 1-hexylamine ligands showed the best short circuit current and power conversion efficiency. The improvements in device characteristics associated with the hybrid solar cell containing TPs treated with 1-hexylamine ligands, when compared with the treatment with pyridine ligands, are attributed to the suppressed bimolecular recombination process within the active layer due to the reduced depth of trap states. We believe that the modular fabrication presented herein is one of versatile platforms to fabricate solution-processible nanocrystal/conducting polymer hybrid

solar cells easily applicable to different semiconductor nanocrystals and other novel conducting polymers.

These approaches to enhance efficiency of polymer-NC hybrid solar cells, including the surface modification of NCs, suitable device structure, and novel processing method, could be expanded to other kinds of optoelectronic devices.

Bibilography

[1]   N. S. Lewis, "Toward Cost-Effective Solar Energy Use," *Science,* vol. 315, no. 5813, pp.798-801, 2007.

[2]   W. Shockley and H. J. Queisser, "Detailed Balance Limit of Efficiency of p-n Junction Solar Cells," *Journal of Applied Physics,* vol. 32, no. 3, pp.510-519, 1961.

[3]   K. W. J. Barnham and G. Duggan, "A new approach to high-efficiency multi-band-gap solar cells," *Journal of Applied Physics,* vol. 67, no. 7, pp.3490-3493, 1990.

[4]   R. P. Raffaelle, S. L. Castro, A. F. Hepp*, et al.*, "Quantum dot solar cells," *Progress in Photovoltaics: Research and Applications,* vol. 10, no. 6, pp.433-439, 2002.

[5]   Z. Liu, Y. Sun, J. Yuan*, et al.*, "High-Efficiency Hybrid Solar Cells Based on Polymer/PbSxSe1-x Nanocrystals Benefiting from Vertical Phase Segregation," *Advanced Materials,* vol. 25, no. 40, pp.5772–5778, 2013.

[6]   R. Vogel, K. Pohl and H. Weller, "Sensitization of highly porous, polycrystalline TiO2 electrodes by quantum sized CdS," *Chemical Physics Letters,* vol. 174, no. 3–4, pp.241-246, 1990.

[7]   J. W. Lee, D. Y. Son, T. K. Ahn*, et al.*, "Quantum-dot-sensitized solar cell with unprecedentedly high photocurrent," *Scientific reports,* vol. 3, no. pp.1050, 2013.

[8]   P. K. Santra and P. V. Kamat, "Mn-Doped Quantum Dot Sensitized Solar Cells: A Strategy to Boost Efficiency over 5%," *Journal of the American Chemical Society,* vol. 134, no. 5, pp.2508-2511, 2012.

[9]   Q. Zhang, X. Guo, X. Huang*, et al.*, "Highly efficient CdS/CdSe-sensitized solar cells controlled by the structural properties of compact porous TiO2 photoelectrodes," *Physical Chemistry Chemical Physics,* vol. 13, no. 10, pp.4659-4667, 2011.

[10]   H. Zhang, K. Cheng, Y. M. Hou*, et al.*, "Efficient CdSe quantum dot-sensitized solar cells prepared by a postsynthesis assembly approach," *Chemical Communications,* vol. 48, no. 91, pp.11235-11237, 2012.

[11]   E. J. D. Klem, D. D. MacNeil, P. W. Cyr*, et al.*, "Efficient solution-processed infrared photovoltaic cells: Planarized all-inorganic bulk heterojunction devices via inter-quantum-dot bridging during growth from solution," *Applied Physics Letters,* vol. 90, no. 18, pp.183113, 2007.

[12]   W. Ma, S. L. Swisher, T. Ewers*, et al.*, "Photovoltaic Performance of Ultrasmall PbSe Quantum Dots," *ACS Nano,* vol. 5, no. 10, pp.8140-8147, 2011.

[13]   P. Maraghechi, A. J. Labelle, A. R. Kirmani*, et al.*, "The Donor–Supply Electrode Enhances Performance in Colloidal Quantum Dot Solar Cells," *ACS Nano,* vol. 7, no. 7, pp.6111-6116, 2013.

[14]   O. E. Semonin, J. M. Luther, S. Choi*, et al.*, "Peak External Photocurrent Quantum Efficiency Exceeding 100% via MEG in a Quantum Dot Solar Cell," *Science,* vol. 334, no. 6062, pp.1530-1533, 2011.

[15]   W. U. Huynh, J. J. Dittmer and A. P. Alivisatos, "Hybrid Nanorod-Polymer Solar Cells," *Science,* vol. 295, no. 5564, pp.2425-2427, 2002.

[16]   B. Sun and N. C. Greenham, "Improved efficiency of photovoltaics based on CdSe nanorods and poly(3-hexylthiophene) nanofibers," *Physical Chemistry Chemical Physics,* vol. 8, no. 30, pp.3557-3560, 2006.

[17]   M. D. Heinemann, K. von Maydell, F. Zutz*, et al.*, "Photo-induced Charge Transfer and Relaxation of Persistent Charge Carriers in Polymer/Nanocrystal Composites for Applications in Hybrid Solar Cells," *Advanced Functional Materials,* vol. 19, no. 23, pp.3788-3795, 2009.

[18]   S. Dayal, N. Kopidakis, D. C. Olson*, et al.*, "Photovoltaic Devices with a Low Band Gap Polymer and CdSe Nanostructures Exceeding 3% Efficiency," *Nano Letters,* vol. 10, no. 1, pp.239-242, 2010.

[19]   Y. Wu and G. Zhang, "Performance Enhancement of Hybrid Solar Cells Through Chemical Vapor Annealing," *Nano Letters,* vol. 10, no. 5, pp.1628-1631, 2010.

[20]   Y. Zhou, F. S. Riehle, Y. Yuan*, et al.*, "Improved efficiency of hybrid solar cells based on non-ligand-exchanged CdSe quantum dots and poly(3-hexylthiophene)," *Applied Physics Letters,* vol. 96, no. 1, pp.013304, 2010.

[21]   N. Radychev, I. Lokteva, F. Witt*, et al.*, "Physical Origin of the Impact of Different Nanocrystal Surface Modifications on the Performance of CdSe/P3HT Hybrid Solar Cells," *The Journal of Physical Chemistry C,* vol. 115, no. 29, pp.14111-14122, 2011.

[22]   Y. Zhou, M. Eck, C. Men*, et al.*, "Efficient polymer nanocrystal hybrid solar cells by improved nanocrystal composition," *Solar Energy Materials and Solar Cells,* vol. 95, no. 12, pp.3227-3232, 2011.

[23]   D. Celik, M. Krueger, C. Veit, *et al.*, "Performance enhancement of CdSe nanorod-polymer based hybrid solar cells utilizing a novel combination of post-synthetic nanoparticle surface treatments," *Solar Energy Materials and Solar Cells,* vol. 98, no. 0, pp.433-440, 2012.

[24]   M. J. Greaney, S. Das, D. H. Webber, *et al.*, "Improving Open Circuit Potential in Hybrid P3HT:CdSe Bulk Heterojunction Solar Cells via Colloidal tert-Butylthiol Ligand Exchange," *ACS Nano,* vol. 6, no. 5, pp.4222-4230, 2012.

[25]   K. F. Jeltsch, M. Schädel, J.-B. Bonekamp, *et al.*, "Efficiency Enhanced Hybrid Solar Cells Using a Blend of Quantum Dots and Nanorods," *Advanced Functional Materials,* vol. 22, no. 2, pp.397-404, 2012.

[26]   R. Zhou, Y. Zheng, L. Qian, *et al.*, "Solution-processed, nanostructured hybrid solar cells with broad spectral sensitivity and stability," *Nanoscale,* vol. 4, no. 11, pp.3507-3514, 2012.

[27]   H.-C. Liao, S.-Y. Chen and D.-M. Liu, "In-Situ Growing CdS Single-Crystal Nanorods via P3HT Polymer as a Soft Template for Enhancing Photovoltaic Performance," *Macromolecules,* vol. 42, no. 17, pp.6558-6563, 2009.

[28]   S. Ren, L.-Y. Chang, S.-K. Lim, *et al.*, "Inorganic–Organic Hybrid Solar Cell: Bridging Quantum Dots to Conjugated Polymer Nanowires," *Nano Letters,* vol. 11, no. 9, pp.3998-4002, 2011.

[29]   S. D. Oosterhout, M. M. Wienk, S. S. van Bavel, *et al.*, "The effect of three-dimensional morphology on the efficiency of hybrid polymer solar cells," *Nat Mater,* vol. 8, no. 10, pp.818-824, 2009.

[30]   M.-C. Wu, C.-H. Chang, H.-H. Lo, *et al.*, "Nanoscale morphology and performance of molecular-weight-dependent poly(3-hexylthiophene)/TiO2 nanorod hybrid solar cells," *Journal of Materials Chemistry,* vol. 18, no. 34, pp.4097-4102, 2008.

[31]   S. Dayal, M. O. Reese, A. J. Ferguson, *et al.*, "The Effect of Nanoparticle Shape on the Photocarrier Dynamics and Photovoltaic Device Performance of Poly(3-hexylthiophene):CdSe Nanoparticle Bulk Heterojunction Solar Cells," *Advanced Functional Materials,* vol. 20, no. 16, pp.2629-2635, 2010.

[32]   I. Gur, N. A. Fromer, C.-P. Chen, *et al.*, "Hybrid Solar Cells with Prescribed Nanoscale Morphologies Based on Hyperbranched Semiconductor Nanocrystals," *Nano Letters,* vol. 7, no. 2, pp.409-414, 2007.

[33]   N. C. Greenham, X. Peng and A. P. Alivisatos, "Charge separation and transport in conjugated-polymer/semiconductor-nanocrystal composites studied by photoluminescence quenching and photoconductivity," *Physical Review B,* vol. 54, no. 24, pp.17628-17637, 1996.

[34]   S. Zhang, P. W. Cyr, S. A. McDonald, *et al.*, "Enhanced infrared photovoltaic efficiency in PbS nanocrystal/semiconducting polymer composites: 600-fold increase in maximum power output via control of the ligand barrier," *Applied Physics Letters,* vol. 87, no. 23, pp.-, 2005.

[35]   J. D. Olson, G. P. Gray and S. A. Carter, "Optimizing hybrid photovoltaics through annealing and ligand choice," *Solar Energy Materials and Solar Cells,* vol. 93, no. 4, pp.519-523, 2009.

[36]   H.-C. Chen, C.-W. Lai, I. C. Wu, *et al.*, "Enhanced Performance and Air Stability of 3.2% Hybrid Solar Cells: How the Functional Polymer and CdTe Nanostructure Boost the Solar Cell Efficiency," *Advanced Materials,* vol. 23, no. 45, pp.5451-5455, 2011.

[37]   J. Seo, M. J. Cho, D. Lee, *et al.*, "Efficient Heterojunction Photovoltaic Cell Utilizing Nanocomposites of Lead Sulfide Nanocrystals and a Low-Bandgap Polymer," *Advanced Materials,* vol. 23, no. 34, pp.3984-3988, 2011.

[38]   Y. Zhou, F. S. Riehle, Y. Yuan*, et al.*, "Improved efficiency of hybrid solar cells based on non-ligand-exchanged CdSe quantum dots and poly(3-hexylthiophene)," *Applied Physics Letters,* vol. 96, no. 1, pp.013304, 2010.

[39]   Y. Zhou, M. Eck, C. Veit*, et al.*, "Efficiency enhancement for bulk-heterojunction hybrid solar cells based on acid treated CdSe quantum dots and low bandgap polymer PCPDTBT," *Solar Energy Materials and Solar Cells,* vol. 95, no. 4, pp.1232-1237, 2011.

[40]   A. Gadisa, M. Svensson, M. R. Andersson*, et al.*, "Correlation between oxidation potential and open-circuit voltage of composite solar cells based on blends of polythiophenes/ fullerene derivative," *Applied Physics Letters,* vol. 84, no. 9, pp.1609-1611, 2004.

[41]   M. C. Scharber, D. Mühlbacher, M. Koppe*, et al.*, "Design Rules for Donors in Bulk-Heterojunction Solar Cells—Towards 10 % Energy-Conversion Efficiency," *Advanced Materials,* vol. 18, no. 6, pp.789-794, 2006.

[42]   J. Hubin, A. V. Shah and E. Sauvain, "Effects of dangling bonds on the recombination function in amorphous semiconductors," *Philosophical Magazine Letters,* vol. 66, no. 3, pp.115-125, 1992.

[43]   J. Merten, J. M. Asensi, C. Voz*, et al.*, "Improved equivalent circuit and analytical model for amorphous silicon solar cells and modules," *Electron Devices, IEEE Transactions on,* vol. 45, no. 2, pp.423-429, 1998.

[44]   C. Voz, J. Puigdollers, J. M. Asensi*, et al.*, "Analysis of the dynamic short-circuit resistance in organic bulk-heterojunction solar cells: relation to the charge carrier collection efficiency," *Organic Electronics,* vol. 14, no. 6, pp.1643-1648, 2013.

[45]   P. Schilinsky, C. Waldauf and C. J. Brabec, "Recombination and loss analysis in polythiophene based bulk heterojunction photodetectors," *Applied Physics Letters,* vol. 81, no. 20, pp.3885-3887, 2002.

[46]   I. Riedel, J. Parisi, V. Dyakonov*, et al.*, "Effect of Temperature and Illumination on the Electrical Characteristics of Polymer–Fullerene Bulk-Heterojunction Solar Cells," *Advanced Functional Materials,* vol. 14, no. 1, pp.38-44, 2004.

[47]   C. Hof, N. Wyrsch and A. Shah, "Influence of Electrical Field Distortion and i-layer Quality on the Collection Function of Drift-driven a-Si:H Solar Cells," *J. Non-Crystalline Solids,* vol. 266-269, no. pp.1114-1118, 2000.

[48]   X. Zhong, Y. Feng and Y. Zhang, "Facile and Reproducible Synthesis of Red-Emitting CdSe Nanocrystals in Amine with Long-Term Fixation of Particle Size and Size Distribution," *The Journal of Physical Chemistry C,* vol. 111, no. 2, pp.526-531, 2006.

[49]   J. Lim, W. K. Bae, K. U. Park*, et al.*, "Controlled Synthesis of CdSe Tetrapods with High Morphological Uniformity by the Persistent Kinetic Growth and the Halide-Mediated Phase Transformation," *Chemistry of Materials,* vol. 25, no. 8, pp.1443-1449, 2012.

[50]   I. Lokteva, N. Radychev, F. Witt*, et al.*, "Surface Treatment of CdSe Nanoparticles for Application in Hybrid Solar Cells: The Effect of Multiple Ligand Exchange with Pyridine," *The Journal of Physical Chemistry C,* vol. 114, no. 29, pp.12784-12791, 2010.

[51]   J. Jasieniak, M. Califano and S. E. Watkins, "Size-Dependent Valence and Conduction Band-Edge Energies of Semiconductor Nanocrystals," *ACS Nano,* vol. 5, no. 7, pp.5888-5902, 2011.

[52]   W. W. Yu, L. Qu, W. Guo*, et al.*, "Experimental Determination of the Extinction Coefficient of CdTe, CdSe, and CdS Nanocrystals," *Chemistry of Materials,* vol. 15, no. 14, pp.2854-2860, 2003.

[53]   W. Kim, S. J. Lim, S. Jung*, et al.*, "Binary Amine−Phosphine Passivation of Surface Traps on CdSe Nanocrystals," *The Journal of Physical Chemistry C,* vol. 114, no. 3, pp.1539-1546, 2010.

[54]   D. Yu, C. Wang and P. Guyot-Sionnest, "n-Type Conducting CdSe Nanocrystal Solids," *Science,* vol. 300, no. 5623, pp.1277-1280, 2003.

[55]   D. Yu, B. L. Wehrenberg, P. Jha*, et al.*, "Electronic transport of *n*-type CdSe quantum dot films: Effect of film treatment," *Journal of Applied Physics,* vol. 99, no. 10, pp.104315-104315-104317, 2006.

[56]   M. V. Kovalenko, M. Scheele and D. V. Talapin, "Colloidal Nanocrystals with Molecular Metal Chalcogenide Surface Ligands," *Science,* vol. 324, no. 5933, pp.1417-1420, 2009.

[57]   E. Talgorn, E. Moysidou, R. D. Abellon*, et al.*, "Highly Photoconductive CdSe Quantum-Dot Films: Influence of Capping Molecules and Film Preparation Procedure," *The Journal of Physical Chemistry C,* vol. 114, no. 8, pp.3441-3447, 2010.

[58]   H. Yang, T. J. Shin, L. Yang*, et al.*, "Effect of Mesoscale Crystalline Structure on the Field-Effect Mobility of Regioregular Poly(3-hexyl thiophene) in Thin-Film Transistors," *Advanced Functional Materials,* vol. 15, no. 4, pp.671-676, 2005.

[59]   T. Leijtens, J. Lim, J. Teuscher*, et al.*, "Charge Density Dependent Mobility of Organic Hole-Transporters and Mesoporous TiO2 Determined by Transient Mobility Spectroscopy: Implications to Dye-Sensitized and Organic Solar Cells," *Advanced Materials,* vol. 25, no. 23, pp.3227-3233, 2013.

[60]   J. H. Lee, S. Cho, A. Roy, *et al.*, "Enhanced diode characteristics of organic solar cells using titanium suboxide electron transport layer," *Applied Physics Letters,* vol. 96, no. 16, pp.163303, 2010.

[61]   P. K. Watkins, A. B. Walker and G. L. B. Verschoor, "Dynamical Monte Carlo Modelling of Organic Solar Cells: The Dependence of Internal Quantum Efficiency on Morphology," *Nano Letters,* vol. 5, no. 9, pp.1814-1818, 2005.

[62]   O. Voznyy, "Mobile Surface Traps in CdSe Nanocrystals with Carboxylic Acid Ligands," *The Journal of Physical Chemistry C,* vol. 115, no. 32, pp.15927-15932, 2011.

[63]   D. Chirvase, Z. Chiguvare, M. Knipper, *et al.*, "Electrical and optical design and characterisation of regioregular poly(3-hexylthiophene-2,5diyl)/fullerene-based heterojunction polymer solar cells," *Synthetic Metals,* vol. 138, no. 1–2, pp.299-304, 2003.

[64]   S. Yoo, B. Domercq and B. Kippelen, "Intensity-dependent equivalent circuit parameters of organic solar cells based on pentacene and C[sub 60]," *Journal of Applied Physics,* vol. 97, no. 10, pp.103706, 2005.

[65]   H. Lili, Q. Donghuan, J. Xi, *et al.*, "Synthesis of high quality zinc-blende CdSe nanocrystals and their application in hybrid solar cells," *Nanotechnology,* vol. 17, no. 18, pp.4736, 2006.

[66]   J. Liu, T. Tanaka, K. Sivula, *et al.*, "Employing End-Functional Polythiophene To Control the Morphology of Nanocrystal−Polymer Composites in Hybrid Solar Cells," *Journal of the American Chemical Society,* vol. 126, no. 21, pp.6550-6551, 2004.

[67]   B. Sun, E. Marx and N. C. Greenham, "Photovoltaic Devices Using Blends of Branched CdSe Nanoparticles and Conjugated Polymers," *Nano Letters,* vol. 3, no. 7, pp.961-963, 2003.

[68]   B. Sun, H. J. Snaith, A. S. Dhoot*, et al.*, "Vertically segregated hybrid blends for photovoltaic devices with improved efficiency," *Journal of Applied Physics,* vol. 97, no. 1, pp.014914, 2005.

[69]   P. Wang, A. Abrusci, H. M. P. Wong*, et al.*, "Photoinduced Charge Transfer and Efficient Solar Energy Conversion in a Blend of a Red Polyfluorene Copolymer with CdSe Nanoparticles," *Nano Letters,* vol. 6, no. 8, pp.1789-1793, 2006.

[70]   L. Qian, J. Yang, R. Zhou*, et al.*, "Hybrid polymer-CdSe solar cells with a ZnO nanoparticle buffer layer for improved efficiency and lifetime," *Journal of Materials Chemistry,* vol. 21, no. 11, pp.3814-3817, 2011.

[71]   R. Zhou, R. Stalder, D. Xie*, et al.*, "Enhancing the Efficiency of Solution-Processed Polymer:Colloidal Nanocrystal Hybrid Photovoltaic Cells Using Ethanedithiol Treatment," *ACS Nano,* vol. 7, no. 6, pp.4846-4854, 2013.

[72]   D. V. Talapin, J. H. Nelson, E. V. Shevchenko*, et al.*, "Seeded Growth of Highly Luminescent CdSe/CdS Nanoheterostructures with Rod and Tetrapod Morphologies," *Nano Letters,* vol. 7, no. 10, pp.2951-2959, 2007.

[73]   J. K. Cooper, A. M. Franco, S. Gul*, et al.*, "Characterization of Primary Amine Capped CdSe, ZnSe, and ZnS Quantum Dots by FT-IR: Determination of Surface Bonding Interaction and Identification of Selective Desorption," *Langmuir,* vol. 27, no. 13, pp.8486-8493, 2011.

[74]   A. Nag, M. V. Kovalenko, J.-S. Lee*, et al.*, "Metal-free Inorganic Ligands for Colloidal Nanocrystals: S^{2-}, HS^{-}, Se^{2-}, HSe^{-}, Te^{2-}, HTe^{-}, TeS_3^{2-}, OH^{-}, and NH_2^{-} as Surface Ligands," *Journal of the American Chemical Society,* vol. 133, no. 27, pp.10612-10620, 2011.

[75]   J. M. Luther, M. Law, Q. Song*, et al.*, "Structural, Optical, and Electrical Properties of Self-Assembled Films of PbSe Nanocrystals Treated with 1,2-Ethanedithiol," *ACS Nano,* vol. 2, no. 2, pp.271-280, 2008.

[76]   K. E. Knowles, D. B. Tice, E. A. McArthur*, et al.*, "Chemical Control of the Photoluminescence of CdSe Quantum Dot−Organic Complexes with a Series of Para-Substituted Aniline Ligands," *Journal of the American Chemical Society,* vol. 132, no. 3, pp.1041-1050, 2009.

[77]   V. I. Klimov, "Optical Nonlinearities and Ultrafast Carrier Dynamics in Semiconductor Nanocrystals," *The Journal of Physical Chemistry B,* vol. 104, no. 26, pp.6112-6123, 2000.

[78]   M. Soreni-Harari, N. Yaacobi-Gross, D. Steiner*, et al.*, "Tuning Energetic Levels in Nanocrystal Quantum Dots through Surface Manipulations," *Nano Letters,* vol. 8, no. 2, pp.678-684, 2008.

[79]   S. N. Yongju Park, Donggu Lee, Jun Young Kim and Changhee Lee, "Temperature and Light Intensity Dependence of Polymer Solar Cells with MoO3 and PEDOT:PSS as a Buffer Layer," *Journal of the Korean Physical Society,* vol. 59, no. pp.362~366, 2011.

[80]   H. Bässler, "Charge Transport in Disordered Organic Photoconductors a Monte Carlo Simulation Study," *physica status solidi (b),* vol. 175, no. 1, pp.15-56, 1993.

[81]   K. Vandewal, A. Gadisa, W. D. Oosterbaan*, et al.*, "The Relation Between Open-Circuit Voltage and the Onset of Photocurrent Generation by Charge-Transfer Absorption in Polymer：Fullerene Bulk Heterojunction Solar Cells," *Advanced Functional Materials,* vol. 18, no. 14, pp.2064-2070, 2008.

[82]   K. Vandewal, K. Tvingstedt, A. Gadisa, *et al.*, "On the origin of the open-circuit voltage of polymer-fullerene solar cells," *Nature Materials,* vol. 8, no. 11, pp.904-909, 2009.

[83]   K. Vandewal, K. Tvingstedt, A. Gadisa, *et al.*, "Relating the open-circuit voltage to interface molecular properties of donor:acceptor bulk heterojunction solar cells," *Physical Review B,* vol. 81, no. 12, pp.125204, 2010.

[84]   P. Guyot-Sionnest, M. Shim, C. Matranga, *et al.*, "Intraband relaxation in CdSe quantum dots," *Physical Review B,* vol. 60, no. 4, pp.R2181-R2184, 1999.

[85]   J. Y. Kim, H. Lee, J. Park, *et al.*, "Effect of Sol-Gel-Derived ZnO Interfacial Layer on the Photovoltaic Properties of Polymer Solar Cells," *Japanese Journal of Applied Physics,* vol. 51, no. 10, pp.10NE29, 2012.

Publication

[1] International Journals

1. C. K. Suman, S. Noh, S. Kim, S.-D. Lee, C. Lee, <u>D. Lee</u> and J. Park, "Electrical impedence studies of the effect of a buffer layer on organic bulk hetrojunction solar cells," *Journal of the Korean Physical Society* , vol. 53, no. 6, pp. 3278–3282, 2008.

2. W. K. Bae, J. Kwak, J. Lim, <u>D. Lee</u>, M. K. Nam, K. Char, C. Lee and S. Lee, "Deep blue light-emitting diodes based on Cd1−xZnxS@ZnS quantum dots," *Nanotechnology,* vol. 20, no. 7, p. 075202, 2009.

3. <u>D. Lee</u>, J. Park, S. Noh, J. Kim, S. Lee and C. Lee, "Effect of Solution Processed Salt Layers on the Device Performances of Polymer Solar Cells," *Thin Solid films*. vol. 518, no. 2, pp. 541–544 (2009)

4. S. Noh, C. K. Suman, <u>D. Lee</u>; S. Kim and C. Lee, *"*Study of buffer layer thickness on bulk heterojunction solar cell," *Journal of Nanoscience and Nanotechnology,* vol. 10, no. 10, pp. 6815–6818, 2009.

5. W. K. Bae, J. Kwak, J. Lim, <u>D. Lee</u>, M. K. Nam, K. Char, C. Lee and S. Lee,

"Multicolored Light-Emitting Diodes Based on All-Quantum Dot Multilayer Films Using Layer-by-Layer Assembly Method," *Nano Letters,* vol. 10, no. 7, pp. 2368–2373, 2010.

6. J. Y. Kim, S. Noh, <u>D. Lee</u> and C Lee, "Organic Tandem Solar Cell Using a Semi-transparent Top Electrode for Both-side Light Absorption," *Journal of the Korean Physical Society,* vol. 57, no. 6, pp. 18521855, 2010.

7. <u>D. Lee</u>, W. K. Bae, I. Park, D. Y. Yoon, S. Lee and C. Lee, "Transparent Electrode with ZnO Nanoparticles in Tandem Organic Solar Cells," *Solar Energy Materials and Solar Cells,* vol. 95, no. 1, pp. 365368, 2011.

8. I. Park, Y. Lim, S. Noh, <u>D. Lee</u>, M. Meister, J. J. Amsden, F. Laquai, C. Lee and D. Y. Yoon, "Enhanced photovoltaic performance of ZnO nanoparticle/poly(phenylene vinylene) hybrid photovoltaic cells by semiconducting surfactant," *Organic Electronics,* vol. 12, no. 3, pp. 424–428, 2011.

9. J. Y. Kim, S. Noh, <u>D. Lee</u>, P. K. Nayak, Y. Hong and C. Lee, "Solution-Processable Zinc Oxide for the Polymer Solar Cell Based on P3HT:PCBM," *Journal of Nanoscience and Nanotechnology,* vol. 11, no. 7, pp. 59956000, 2011.

10. Y. Park, S. Noh, <u>D. Lee</u>, J. Kim and C. Lee, "Study of the Cesium Carbonate (Cs_2CO_3) Inter Layer Fabricated by Solution Process on P3HT:PCBM Solar Cells," *Molecular Crystals and Liquid Crystals*, vol. 538, no. 1, pp. 20-27, 2011.

11. S. Noh, <u>D. Lee</u>, J. Y. Kim, Y. Park, C. Lee and J. J. Amsden, "Area and Light Intensity Dependence of Buffer Layers on P3HT:PCBM Solar Cells," *Journal*

of the Korean Physical Society, vol. 59, no.2, pp. L207L210, 2011.

12. Y. Park, S. Noh, <u>D. Lee</u>, J. Y. Kim and C. Lee, "Temperature and Light Intensity Dependence of Polymer Solar Cells with MoO_3 and PEDOT:PSS as a Buffer Layer," *Journal of the Korean Physical Society,* vol. 59, no.2, pp. 362-366, 2011.

13. J. Lim, W. K. Bae, <u>D. Lee</u>, M. K. Nam, J. Jung, C. Lee, K. Char and S. Lee, "InP@ZnSeS, Core@Composition Gradient Shell Quantum Dots with Enhanced Stability," *Chemistry of Materials*, vol. 23, no. 20, pp. 44594463, 2011.

14. J. Kwak, W. K. Bae, <u>D. Lee</u>, I. Park, J. Lim, M. Park, H. Cho, H. Woo, D. Y. Yoon, K. Char, S. Lee and C. Lee, "Bright and efficient full-color colloidal quantum dot light-emitting diodes using an inverted device structure," *Nano Letters,* vol. 12, no. 5, pp. 23622366, 2012.

15. J. Y. Kim, H. Lee, J. Park, <u>D. Lee</u>, H.-J. Song, J. Kwak and C. Lee, "Effect of Sol-Gel-Derived ZnO Interfacial Layer on the Photovoltaic Properties of Polymer Solar Cells," *Japanese Journal of Applied Physics,* vol. 51, no. 10, p. 10NE29, 2012.

16. L. zur Borg, <u>D. Lee</u>, J. Lim, W. K. Bae, M. Park, S. Lee, C. Lee, K. Char and R. Zentel, "The effect of band gap alignment on the hole transport from semiconducting block copolymers to quantum dots," *Journal of Materials Chemistry C*, vol. 1, no. 9, pp. 1722-1726, 2013.

17. J.-W. Mun, I. Cho, <u>D. Lee</u>, W. S. Yoon, O. K. Kwon, C. Lee and S. Y. Park, "Acetylene-bridged D-A-D type small molecule comprising pyrene and

diketopyrrolopyrrole for high efficiency organic solar cells," *Organic Electronics*, vol. 14, no. 9, pp. 23412347, 2013.

18. H.-J. Song, J. Y. Kim, <u>D. Lee</u>, J. Song, Y. Ko, J. Kwak and C. Lee, "Origin of the Mixing Ratio Dependence of Power Conversion Efficiency in Bulk Heterojunction Organic Solar Cells with Low Donor Concentration," *Journal of Nanoscience and Nanotechnology,* vol. 13, no. 12, pp. 79827987, 2013.

19. J. Lim, M. Park, W. K. Bae, <u>D. Lee</u>, S. Lee, C. Lee and K. Char, "Highly Efficient Cadmium-Free Quantum Dot Light-Emitting Diodes Enabled by the Direct Formation of Excitons within InP@ZnSeS Quantum Dots," *ACS Nano,* vol. 7, no. 10, pp. 90199026, 2013.

20. W. K. Bae, Y.-S. Park, J. Lim, <u>D. Lee</u>, L. A. Padilha, H. McDaniel, I. Robel, C. Lee, J. M. Pietryga and V. I. Klimov, "Controlling the influence of Auger recombination on the performance of quantum-dot light-emitting diodes," *Nature Communications,* vol. 4, p. 2661, 2013.

[2] International Conferences

1. <u>D. Lee</u>**,** S. Noh, C. K. Suman, S. Lee and C. Lee, "Investigation of active layer thickness dependence of polymer solar cells   based on poly(3-hexylthiophene) by impedance spectroscopy," *International Conference on Advanced Functional Polymers and Self-Organized Materials (ICPSM)*, Poster, 2008.

2. <u>D. Lee</u>, J. Park, S. Noh, J. Kim, S. Lee and C. Lee, "Effect of Solution Processed Salt Layers on the Device Performances of Polymer Solar Cells," *The 8th International Conference on Nano-Molecular Electronics (ICNME*

2008), PI-51, 2008.

3. <u>D. Lee</u>, W. K. Bae, I. Park, D. Y. Yoonc, S. Lee, and C. Lee, "Transparent electrode with ZnO nanoparticles in tandem organic solar cells", *19th International Photovoltaic Science and Engineering Conference and Exhibition*, OSC-P2-42, 2009.

4. <u>D. Lee</u>, S. Noh, C. K. Suman, J. Kim, S. Lee and C. Lee, "Characteristics of Polymer Solar Cells Depending on the Thickness of Active Layer", *9th international Meeting on Information Display (iMiD 2009),* IMID 2009 Digest pp. 12041207, 2009.

5. <u>D. Lee</u>, J. Kim, S. Noh and C. Lee, "The Thickness of Active Layer Dependence of Polymer Solar Cells," *IEEE NANO 2010*, ICP-TS13-014, 2010.

6. <u>D. Lee</u>, J. Lim, J. Y. Kim, M. Park, Y. Ko, K. Char, S. Lee, C. Lee and J. Kwak, "Thermal Annealing Effect on P3HT:CdSe Nanoparticle Bulkheterojunction Solar Cells," *2011 MRS Fall Meeting & Exhibit*, H3.67, 2011.

7. <u>D. Lee</u>, J. Lim, J. Y. Kim, H.-J. Song, M. Park, J. Song, H. J. Syn, Y. Ko, K. Char, S. Lee and C. Lee, "Study on Surfactants of CdSe Quantum Dots for Solar Cell Application," *Global Photovoltaic Conference 2012 (GPVC 2012) & Korea-EU International Symposium on Photovoltaics*, OSC-P-24, 2012.

8. <u>D. Lee</u>, J. Lim, J. Y. Kim, H. Song, H. Syn, J. Song, Y. Ko, K. Char, S. Lee and C. Lee, "Polymer-Nanocrystal Hybrid Solar Cells Using CdSe Tetrapod Network Structure," *2013 MRS Spring Meeting & Exhibit*, B11.93, 2013.

[3] Domestic Conferences

1. <u>D. Lee</u>, S. Noh, J. Y. Kim, H. Lee, J. Kwak and C. Lee, "Temperature Dependence of Current-Voltage Characteristics of Polymer Solar Cells with MoO_3 and PEDOT:PSS as Hole Injection Layer," Nano Korea 2011, P1108-089, 2011.

2. <u>D. Lee</u>, J. Lim, K. Char, S. Lee and C. Lee, "Polymer-Nanoparticle Bulk-hetrojunction Solar Cells with Various Surface Modification," 한국유기태양전지학회 2012 하계심포지엄, Poster, 2012.

3. <u>D. Lee</u>, J. Lim, L. zur Borg, M. Park, H. Lee, S. Lee, K. Char, R. Zentel, and C. Lee, "Investigation of Hole Injection Barrier of Quantum Dot-Conducting Polymer Hybrids LEDs," The 20th Korean Conference on Semiconductors, TP2-9, 2013.

한글 초록

콜로이드 반도체 나노결정은 크기 및 형태를 조절함에 따라 광학적 특징 및 전기적 특성을 조절할 수 있고, multiple exciton generation 현상을 통한 효율적인 광에너지 활용이 가능하기 때문에 최근 이를 이용한 차세대 고효율 태양전지가 주목받고 있다. 또한 잉크젯 프린팅, 스핀 코팅과 같은 용액공정을 기반으로 태양전지를 제작 가능하기 때문에 공정단가를 낮출 수 있는 장점이 있다. 하지만, 나노결정의 표면에 위치한 비결합성 분자 오비탈에 의해 발생하는 표면 에너지 준위는 나노결정의 전기적 및 광학적 특성을 저해하기 때문에, 나노결정의 표면 에너지 준위를 패시베이션하기 위한 연구가 필요하다.

나노결정의 표면 에너지 준위를 억제하며, 전기적 특성을 저해하지 않도록 다양한 접근법이 연구되어 왔지만, 나노결정의 표면 개질은 다양한 반응조건(온도, 계면활성제의 농도, 반응 시간, 계면활성제의 길이 및 반응도)에 따라 민감하게 변화하기 때문에 대부분의 연구는 나노결정의 표면 개질 전·후에 따른 태양전지 특성 변화만을 보고하였다.

따라서 본 논문에서는 나노결정의 표면 개질 조건에 따른 나노결정의 표면 리간드를 정량적으로 분석하고, 리간드의 평균적인 길이 및 밀도에 따른 고분자-나노결정 하이브리드 태양전지의

특성과의 상관관계를 분석하였다. 1H-NMR 을 통해 계면 활성제의 작용기의 종류(카르복실 산, 아민 계열)및 치환 순서에 따른 표면 개질 정도를 정량화 하였고, 이를 Poly(3-hexylthiophene) P3HT:CdSe QD 벌크 이종접합 태양전지특성에 미치는 영향을 분석하였다. 태양전지의 전류-전압 곡선, 외부양자효율 측정 및 입사광 세기에 따른 전류-전압 곡선의 변화를 통해 광전자의 수집 및 결합특성을 분석하였다. 이를 기반으로 P3HT:CdSe QD BHJ 태양전지의 혼합비율 및 두께, 열처리에 따른 특성변화 또한 연구하였다. 계면활성제의 평균 길이를 줄이고, 1-hexylamine 리간드를 통해 표면을 안정화 함으로서, 72%의 광전하 수집 효율을 보였고, 2% 전력변환효율을 얻을 수 있었다.

하지만 위와 같은 용액상에서의 나노결정을 치환하는 공정은 나노결정의 콜로이드 분산성을 변화시키기 때문에 고분자-나노결정 광흡수층의 나노 모폴로지의 변화가 불가피하다. 이러한 나노 모폴로지 또한 나노결정의 표면 리간드과 더불어 태양전지의 소자 특성에 영향을 미치기 때문에, 표면 리간드에 의한 태양전지의 특성 변화를 연구하기 위해서는 나노모폴로지가 고정된 상태에서 이루어 져야한다. 따라서 표면 개질에 의한 모폴로지의 변화를 막고 신뢰성 문제를 해결하기 위해, 본 논문에서는 모듈식 공정을 이용한 이종접합 형성 방법을 제안하였다. 이러한 모듈식 공정은 테트라포드 나노결정을 형성하는 단계, 형성된 테트라포드의 표면을 개질하는 단계, 고분자를 스며들게 하여 이종접합을 형성하는 단계로 구성된다. 이와 같은 공정법은 기존의 용액상에서 혼합하여 이종접합을 형성하는 방법에 비해 신뢰도가 우수하며, 나노결정의 표면 개질이

나노 모폴로지가 고정된 상태에서 용이하게 이루어지는 장점을 가진다. 모듈식 공정을 적용해 제작된 태양전지를 기반으로 다양한 계면활성제에 의한 태양전지 특성변화를 연구하였다. 1-hexylamine 을 적용할 경우 pyridine 에 비해 2 배 이상의 단락 전류를 향상 시킬 수 있었는데, 이는 1-hexylamine 이 표면 트랩 에너지 준위를 낮추고, 표면 에너지 준위를 패시베이션하여 전자와 정공의 재결합을 억제하기 때문이다.

본 논문을 통한 고분자-나노결정 하이브리드 태양전지의 나노결정의 표면 개질방법, 소자의 구조 및 새로운 공정 방법은 태양전지에 한정되지 않고, 나노결정을 이용한 다양한 광전자 소자에도 적용될 수 있을 것으로 생각된다.